Geophysical and Geological Exploration Applied to Sb Mineralizations

Ana Maria Carvalho

Master in Geology

Departamento de Geociências, Ambiente e Ordenamento do Território da Faculdade de Ciências da Universidade do Porto

2020

Advisor

Rui Miguel Marques Moura, Professor Auxiliar, Faculdade de Ciências da Universidade do Porto

Co-Advisor

Alexandre Martins Campos de Lima, Professor Associado, Faculdade de Ciências da Universidade do Porto

Todas as correções determinadas

pelo júri, e só essas, foram efetuadas.

O Presidente do Júri,

Porto, _____/_____/_____

Acknowledgements

First, I would like to thank my advisor, Professor Doctor Rui Moura, and my co-advisor, Professor Doctor Alexandre Lima, for entrusting me with this project, where I could learn so much, and where I could grow personally and professionally.

I want to thank everyone involved in the AUREOLE project, for the help you have provided with all the bibliographic research as well as mineralogical data. A special thanks to Aurélie Peyrefitte, with whom I have worked more closely, for your availability to help me with everything related to the gravimetric survey, and to Rui Frutuoso, for the help with all the field work and for all your knowledge of the area's geology.

I would like to thank the National Laboratory of Energy and Geology (LNEG) for providing several reports done by associations and companies about the mineralizations in my study area.

A big thank you to Ricardo Ribeiro, Doctorate student at FCUP, for all your invaluable help with every single geophysical method, both in the field, the processing, and the interpretations of the data. I could not have done this without your help.

I want to thank all my friends, Ana Carolina, Catarina Ferraz, Inês Fonseca, Joana Basto and Paula Amorim for this journey that we've had together, where we've supported each other in every way possible.

A special thanks to Vítor Martins and Mariana Costa. You are the best friends anyone could ever ask for. I could not have done this without you. Your support is what kept me going in the hardest times. Thank you for all the laughs and for all the serious moments. I hope there will be many more to come.

I want to thank all my family, especially my cousin Diogo, who has been my companion throughout this entire journey, and who listened and understood all my happy and all my not so happy moments.

I want to thank my boyfriend Rúben, for always supporting me, for always thinking I could do it and never letting me give up. Hope I made you as proud of me, as I am proud of you.

Last, but certainly not least, I want to thank my parents and my brothers. You have made me who I am today. Thank you for pushing me every step of the way and for never giving up on me, no matter how difficult it was. So, from the bottom of my heart, thank you.

Abstract

This thesis is included in the AUREOLE project that intends to improve the knowledge about antimony (Sb) mining exploration, as well as evaluate the potential environmental risk associated with it. Antimony is considered by the European Commission to be a critical raw material, which is why it is important to know more about this element's mineralizations.

The main objective of this work is to add to that knowledge by understanding which are some of the better methods to localize Sb mineralizations along with its associated lithologies and structures.

To do this, one spatial analysis method and four geophysical methods (gravity, electromagnetic, magnetic, and radiometric) were used. Learning how these methods respond to the mineralizations and their surroundings will allow us to know which are most adequate to locate them.

The spatial analysis method consists in the creation of drainage basins from stream sediment data. This data includes geochemical values of several elements in ppb. The drainage basins show the location of higher concentrations of these elements. At Alto do Sobrido some of the higher values of antimony, gold and arsenic can be found. Ribeiro da Serra has the higher values of several elements, such as antimony, gold, arsenic, silver and lead. Terramonte, as expected, holds the highest values of lead, zinc and silver. The higher values of tungsten and tin are in Alvarenga and Covas do Rio, which are locations closest to granitic sources.

From the gravity survey it was possible to add more data to the hypothesis that the gold-antimony mineralizations could be associated with non-outcropping granitic intrusions. A 2D model was proposed be both modelling and inversion to show that the presence of this granite could indeed fit the response of the negative anomalies found in the residual anomaly.

The electromagnetic method is useful in locating areas of lower resistivity, which could occur due to fractures or structures, such as the Douro sheer zone that marks the contact between the CXG and the Carboniferous, due to more weathered areas, or due to mineralizations and their respective alteration products such as was observed in some outcrops of the Alto do Sobrido veins.

With the magnetic method it is possible to contribute towards the location of areas with the prevalence of lithologies and minerals with higher magnetic susceptibilities, which in

this case corresponds to the Alto do Sobrido mineralized vein paragenesis, as well as the location of faults or fractures associated with the Dúrico-Beirã Shear Zone.

The radiometric method allowed a distinction between some lithologies in the area such as the Lower Ordovician quartzites, by showing areas of lower concentration values of K, U and total concentration, while also showing a distinction between the lithologies and facies variations of the CXG and the lithologies from the Medium Ordovician to the Carboniferous.

All the methods provided some insight in relation to the Sb-Au mineralizations, either by locating a confirmed source or by finding structures or lithologies associated with them.

Keywords

Gravity, Magnetic, Radiometric, Electromagnetic, Stream Sediments.

Table of Contents

List of Figures

List of Tables

Abbreviations

1VD – First Vertical Derivative

BA – Bouguer Anomaly

BC – Bouguer Correction

BRGM – Bureau de Recherches Géologiques et Minières

CBD – Consórcio do Baixo Douro

CIZ – Central Iberian Zone

CRM – Critical Raw Material

CXG – Schist-Greywacke Complex

DA – Departamento de Avaliação

DBSZ – Dúrico-Beirã Shear Zone

DEM – Digital Elevation Model

EM – Electromagnetic

EOL-RIR – End-of-life recycling input rate

FA – Flow Accumulation

FAA – Free-air Anomaly

FAC – Free-air Correction

FD – Flow Direction Raster

IGM – Geological and Mining Institute

IGRF – International Geomagnetic Reference Field

ISTO - Institut des Sciences de la Terre d'Orléans

SFM – Serviço de Fomento Mineiro

TC – Terrain Correction

VLF – Very Low Frequency

1. Introduction

1.1 Introduction

The present work constitutes the master's thesis, entitled "Geophysical and Geological Exploration Applied to Sb Mineralizations", for the completion of a Master's degree in Geology at the Faculty of Science of the University of Porto.

This thesis is included in the AUREOLE project which integrates the partnership between the Bureau de Recherches Géologiques et Minières (BRGM) (coordinator), the Institut des Sciences de la Terre d'Orléans (ISTO), the University of Castilla-La Mancha, the Faculty of Science of the University of Porto and the Antea Group.

The AUREOLE project (website https://aureole.brgm.fr/) intends to improve the efficiency of mining exploration of antimony (Sb) and tungsten (W), as well as evaluate the potential environmental risk associated with the exploitation of these elements on a large scale.

The study area approached in this work is the Dúrico-Beirão Gold-Antimony Mining District. There is a lot of knowledge about this area which allows the trial use of several different methods and ensures a better interpretation of those methods as well as their relation and how they respond to Sb mineralizations and to the structures and lithologies associated with them.

1.2 Objectives

The main objective of this thesis is to understand how different geophysical methods respond to the antimony mineralization paragenesis, as well as how these methods respond to the structures and lithologies to which the mineralizations are associated. In order to better localize the Sb occurrences within the Dúrico-Beirão Gold-Antimony Mining District, stream sediment chemical data is used with a new approach to the spatial analysis of this data.

As mentioned before, this work is done on an area where the geology is well known, which allows for a better interpretation of the results of the geophysical methods.

The geophysical methods used in this work are gravity, magnetic, electromagnetic (VLF), and gamma-ray spectrometry (radiometry). With the results that are obtained some 2D processing will be done in order to create maps or sections with the different anomalies. With this it is possible to understand the connections and associations that might exist between the occurrences and the structures and lithologies present.

Once it is clearer how these methods respond to the mineralizations and the different lithologies it will be easier to assess on how to understand them and use them on new areas with similar geographical, geomorphological and geological context.

1.3 Thesis Structure

This thesis is structured in different chapters:

- Chapter 1 – defines the purpose and study area of the thesis along with its objectives.
- Chapter 2 – describes the study area with its geographic, geomorphological, hydrological, geotectonic and geological settings.
- Chapter 3 – this chapter consists of a description of the chemical element Sb, the mineralizations in which it occurs, and the occurrences of these mineralizations on the area of study, the Dúrico-Beirão Mining District.
- Chapters 4, 5, 6, 7, 8 – these chapters contain the methods, results and discussions of the Spatial Analysis of Geochemical Data, the Gravity Survey, the Electromagnetic Survey (VLF), the Magnetic Survey and the Radiometric Survey, respectively.
- Chapter 9 – in this chapter there is a comparison between the two methods that were done on a larger scale, gravity and radiometry, and between the two methods that were done on a smaller scale, magnetic and electromagnetic (VLF).
- Chapter 10 – here can be found the conclusions of this work, along with some comments on the same.

2. Area of Study

2.1 Geographic, Geomorphological and Hydrological Setting

As was stated previously, the study area corresponds to the Dúrico-Beirã Region, also called the Dúrico-Beirão Gold-Antimony Mining District. This region is located in northwest Portugal, within the districts of Braga, Porto, Aveiro and Viseu and it corresponds to a zone with NW-SE direction, approximately 90 Km of extension and a width that goes from 7 to 23 km (Figure 1 in orange). It includes several municipalities, such as Barcelos, Póvoa de Varzim, Vila do Conde, Trofa, Santo Tirso, Valongo, Paredes, Gondomar, Penafiel, Castelo de Paiva, Arouca, São Pedro do Sul and Castro Daire.

For the geophysical methods, the study area is restricted to the Ribeiro da Serra – Alto do Sobrido sector in Gondomar (Figure 1 in pink), where the mines of Alto do Sobrido, Ribeiro da Serra and Tapada are located. The coordinates of this area's vertices can be found on Table 1.

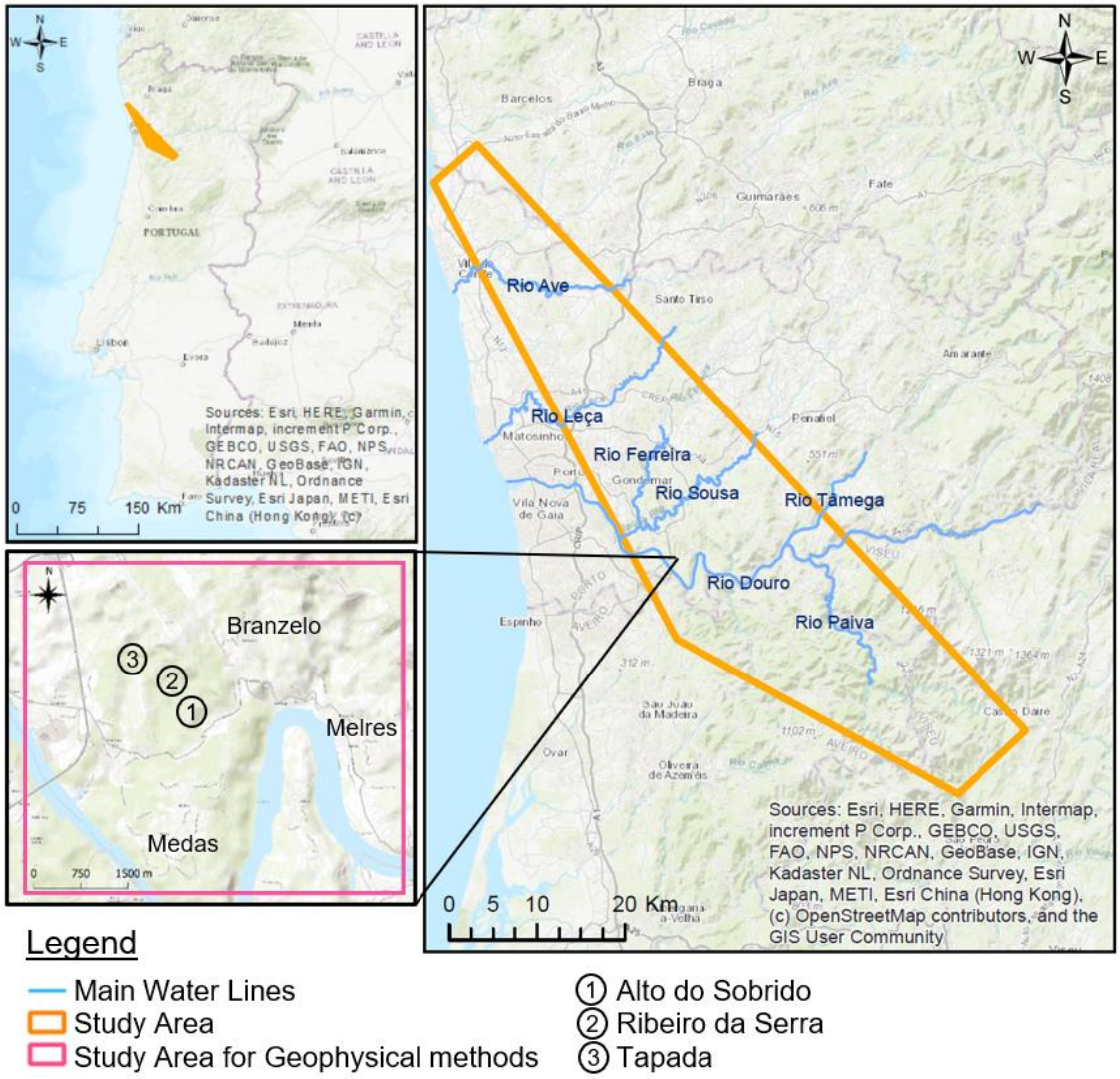

Figure 1 – Study areas' locations and main rivers (images obtained through ArcGIS and QGIS software).

Table 1 – Coordinates of the geophysics study area's vertices (Coordinate System: ETRS89 Portugal TM06, EPSG:3763).

M	P
-21703,02	153077,79
-21718,09	158393,10
-27742,43	153087,31
-27758,68	158376,44

The geomorphology of the area is defined mainly by residual elevations that consist in the quartzite ridges of the Ordovician and granitic intrusions that stand out over the metasedimentary rocks. Some of the most important elevations are ridges, such as the Serras of Santa Justa, Pias, Castiçal, Facho, Santo Antoninho, Rates, Flores, S. Domingos, Santa Iria, Banjas, Boneca (Medeiros, 1964; Medeiros *et al*., 1980).

As is shown in Figure 1 the main rivers in the study area are Douro, Leça, Ave, Paiva, Tâmega, Sousa and Ferreira. Along with the main rivers come their affluents, which are countless. The Douro river has a very narrow and deep valley, whereas the Leça river has a very sinuous valley (Teixeira & Medeiros, 1965; Costa & Teixeira, 1957; Medeiros *et al*., 1980).

The Geological Maps of Portugal (scale 1:50.000) that make up the study area are the sheets 9-A Póvoa de Varzim, 9-C Porto, 9-D Penafiel, 13-A Espinho, 13-B Castelo de Paiva, 13-D Oliveira de Azeméis, 14-A Lamego and 14-C Castro Daire from the Portuguese Geological Services. On Figure 2 can be observed an extract of sheet 13-B Castelo de Paiva, where the study area for the geophysical methods is located.

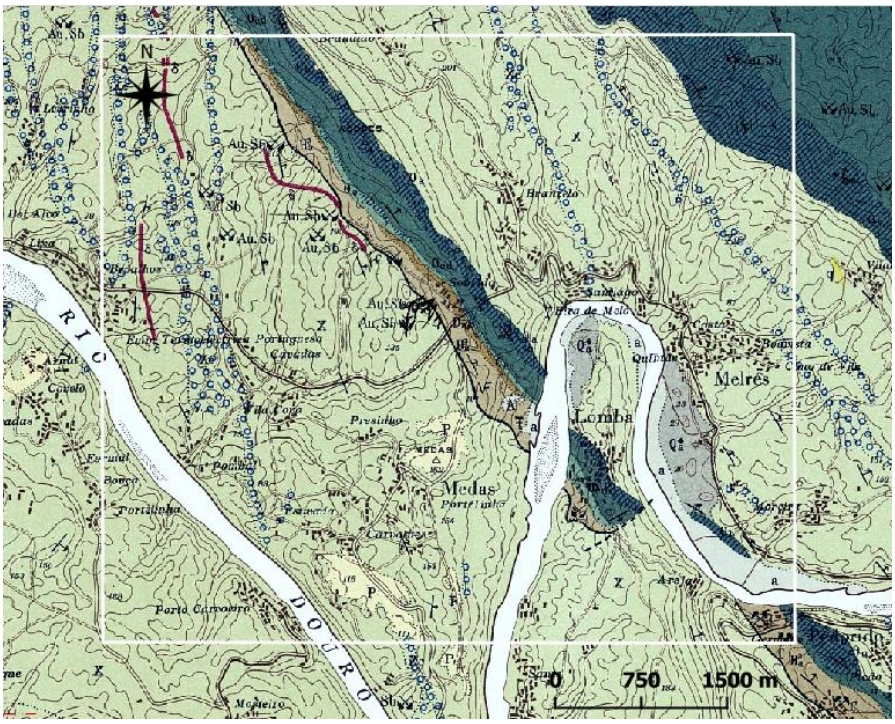

Figure 2 - Extract of the Geological Map of Portugal, sheet 13-B Castelo de Paiva (1:50.000), with the study area for the geophysical methods in white.

2.2 Geotectonic and Geological Setting

The Iberian Peninsula can be divided into 5 zones according to their tectonostratigraphic characteristics (Figure 3): Cantabrian Zone, West Asturian-Leonese Zone, Central Iberian Zone, Ossa Morena Zone and South Portuguese Zone (Julivert *et al*., 1974). The Dúrico-Beirã Region (study area) is located within the Central Iberian Zone (CIZ).

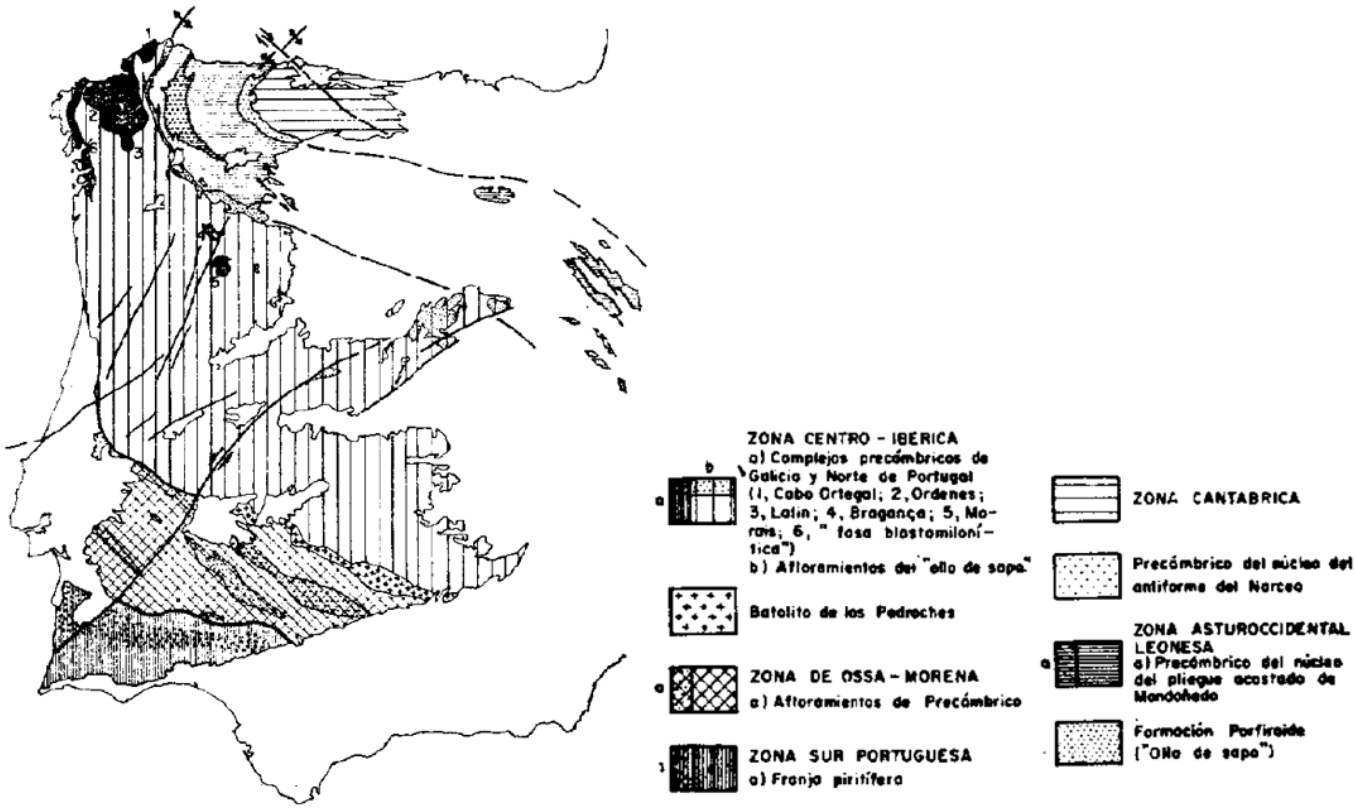

Figure 3 - Tectonostratigraphic zones of the Iberian Peninsula (Source: Julivert et al., 1974).

The main structures within the area of study are the Valongo Anticline and the Dúrico-Beirã Shear Zone that were formed during the Hercynian Orogeny. This orogeny can be described by three phases of deformation, known as D_1, D_2 and D_3. According to Ribeiro & Pereira (1992):

- The first deformation phase (D_1) originated a tectonic flake where the dip of structures changes from subvertical in the centre of the flake to progressively less tilted on the edges.
- The second phase of deformation (D_2) consists in a shear deformation caused by the obduction of oceanic crust, making it so that D_2 can only be observed near the carried rocks.
- Between D_2 and D_3 there is an extensional period where the ascension of the granitoids begins, but these will only have a maximum development during and after the third phase.

- The third phase (D_3) occurred due to the action of conjugated shear zones.

According to Medeiros (1964 *in* Couto, 1993) there was a phase of the Hercynian orogeny, in the end of the Carboniferous or the beginning of the Permian, to which are related the mineralized veins of Sb-Au and W.

The Valongo Anticline is a structure formed during the first deformation phase (D_1) of the Hercynian Orogeny (Figure 4) (Ribeiro *et al*., 1987 *in* Couto, 1993). It consists in an asymmetrical anticline, oriented NW-SE. Its axis dips between 5º to 15º NW and its axial plane dips 60º to the NE (Couto, 1993).

The Anticline has a normal and an inverse limb. The normal limb is located to the east, dips 35º NE, and it goes from Valongo to Castelo de Paiva, for approximately 20 Km until it is cut by Hercynian granites. The inverse limb, located to the west, is subvertical and has an extension of around 50 Km, from Valongo to Castro Daire (Couto, 1993; Couto *et al*., 1997).

The veins are mainly found in the limbs of the Valongo Anticline, where they fill fractures transversal to the main structure. The mineralization is, in general, quite irregular, but in some cases can be found as masses of stibnite (e.g. Montalto mine). The gangue is normally composed of quartz, with carbonates occurring occasionally. Sb-Au exploitations are mostly found in the inverse limb (Couto, 1993).

In the Valongo Anticline have been deposited marine facies from the Precambrian and/or Cambrian up to the Devonian. To the west of the Anticline is located the Dúrico-Beirã Shear Zone (DBSZ) where the Carboniferous continental facies deposited (Couto, 2013).

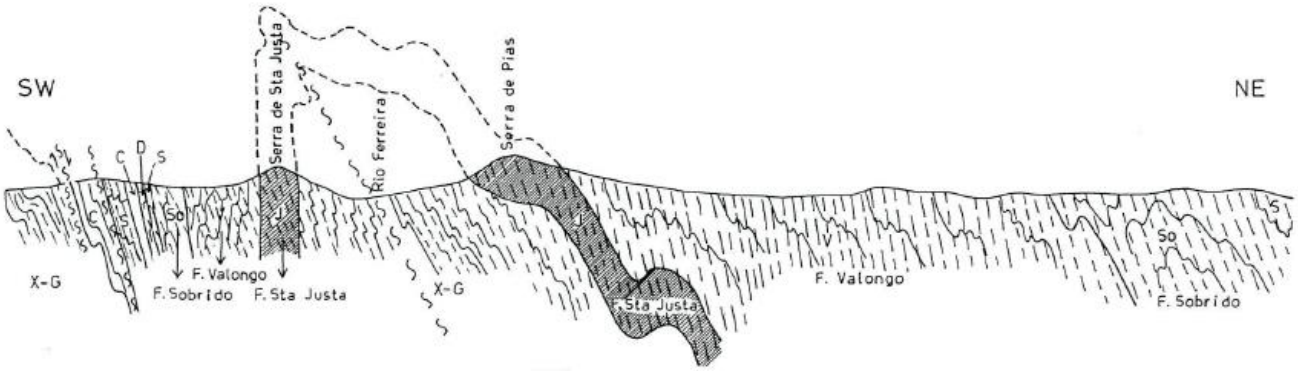

Figure 4 – Regional Geological Profile of the Valongo Anticline: C – Carboniferous, D – Devonian, S – Silurian, So – Sobrido Formation (Ordovician), V – Valongo Formation (Ordovician), J – Santa Justa Formation (Ordovician), X-G – Precambrian and/or Cambrian. (adapted by Couto, 1993).

2.2.1 Precambrian and/or Cambrian (?)

The rocks of Precambrian and/or Cambrian age correspond to the Schist-Greywacke Complex (CXG). The CXG can also be referred to as Dúrico-Beirão Super Group, which separates the Douro Group, to the north, from the Beiras Group to the South (Sousa & Sequeira, 1989; Medina, 1996).

Rocks from the CXG can be found in the Valongo Anticline, in its core, in the Terramonte Unit, and to the SW, in the Montalto and Alto do Sobrido Units (Costa, 1950; Teixeira, 1955; Couto, 1993). Within the CXG occur diabase sills, normally interstratified, whose age is yet to be determined (Couto, 1993).

The **Terramonte Unit** is formed by sediments of turbiditic origin (type “flysch”) and is divided in two lithologic associations. In the first one occurs carbonous dark schists alternating with sandstone to the top. The transition from the first to the second lithologic associations is gradual. The second association is a greenish formation, where epiclastic levels have been observed. Various sedimentary structures can be found in these rocks (Couto, 1993).

In the **Montalto Unit** were described three lithologic associations. The inferior association corresponds to greyish to violaceous schists, fine greywacke and acid volcanic rocks. The intermediate association consists in greyish beige schists alternating with sandstones, and the superior association consists in polygenetic conglomerates with mainly quartz elements, along with pelitic and arenitic levels (Couto, 1993).

The **Alto do Sobrido Unit** is correlated with the intermediate association of the Montalto Unit, and consists in schists alternating with sandstones (Couto, 1993).

2.2.2 Ordovician

Between the Ordovician and the CXG transpires an angular discordance, that was caused by the Sarda phase associated to the opening of the Rheic Ocean (Couto, 1993).

There are three formations that belong to the Ordovician: Santa Justa Formation, Valongo Formation and Sobrido Formation.

The **Sana Justa Formation** (Lower Ordovician) has in its base an irregular conglomerate, with variable granulometry and its elements are mainly quartz. Following these, are quartzites, so called Armorican Quartzites. In these it is possible to find ichnofossils, such as *Cruzianas* and *Skolithos*, as well as sedimentary structures that are characteristic of a coastal marine deposition environment, such as slumps and ripple marks. The quartzites mark the top of the ridges. At the top of this formation can be

observed arenitic levels alternating with pelitic levels, where have also been found volcano-sedimentary levels defined for the first time in the Dúrico-Beirã region by Couto (1993) (in Moreira, 2001).

The Santa Justa Formation passes gradually to the **Valongo Formation** (Middle Ordovician) which has around 300 m of thickness and begins with pinkish siltstones that change to a greyish colour as the sequence continues. Above these can be observed grey schists which contain a very rich fossiliferous content (e.g. trilobites, graptolites, mollusc, brachiopods and echinoderms (Couto *et al*., 1997)), and at the top of the formation can, usually, be found siliceous nodules (Couto, 1993; Couto *et al*, 2013).

The **Sobrido Formation** sits atop the Valongo Formation through a paraconformity. At the lower member of the Sobrido Formation can be observed massive, lenticular and immature whiteish grey quartzites intercalated with thinly bedded grey siltstones and mudstones (Couto, 2013; Couto *et al*., 2013). The transition from the lower member to the upper is gradual for the periclinal zone and eastern limb of the Valongo Anticline. On the western limb there is a mudstone overlaying an eroded lower member. The upper member is formed by diamictites that contain clasts (dropstones), which are locally intercalated with quartzites, conglomerates and slates. These diamictites are very heterogenous and can vary from massive to laminated, clast-rich to clast-poor, and from an argillaceous to arenaceous matrix. Their colour can also vary from grey to reddish or black (Couto *et al*., 2013).

2.2.3 Silurian

The transition from the upper member of the Sobrido Formation to the Silurian is quite variable. In some places the upper member is in erosive contact with black quartzites of the Silurian, but the transition is more commonly observed as a contact between the upper member and light grey quartzites or dark grey slates (Couto *et al.*, 2013).

According to Oliveira et al. (1992 *in* Couto, 1993) the Silurian in the Valongo Anticline is essentially composed by carbonous schists and lyddites, from the **Carbonous Schists Formation**, interbedded with quartzites (Bougado Quartzites).

Couto (1993) described the Silurian in the Dúrico-Beirã region as dark grey schists, followed by light grey to violaceous schists and grey schists.

The **Sobrado Formation** is formed by two members: a greenish grey lower member composed by slates alternating with greywackes, and an upper member composed by grey to black slates intercalated with light siltstones. This formation has been attributed to both the top of the Silurian and the base of the Devonian (Couto *et al*., 1997).

2.2.4 Devonian

The transition from the Silurian to the Devonian is gradual. The rocks of this age consist in arenitic to pelitic formations and are the last marine sediments deposited in this region (Medeiros *et al.*, 1980; Couto, 1993).

In the normal limb of the Valongo Anticline is described the **Telheiras Formation**, which consists in a lower member of quartzites interbedded with schists and dark sandstones, along with an upper member composed of purplish schists (Costa & Teixeira, 1957; Couto *et al*., 1997).

In the contact with the Carboniferous, the Devonian is represented by dark greenish grey schists interbedded with fine sandstone that passes to quartzites (Medeiros et al., 1980). This is correlated with the Sobrado Formation (Couto, 1993).

2.2.5 Carboniferous

The Carboniferous in the Dúrico-Beirã region occurs in continental basins along the western limb of the Valongo Anticline. These basins have a high tectonic control, and the deposition of sediments is mainly sin-tectonic. The sedimentary sequence can be grouped in 4 tectono-sedimentary units that are duplicated (Couto, 1993; Jesus, 2003).

In the base of the Carboniferous is a breccia, that isn't always present, interbedded with clay flows (Jesus, 1986 *in* Couto, 1993). Following these are fossiliferous schists, siltstones, and sandstones. Across this sequence can be found intercalations of conglomerates and coal (Couto, 1993).

3. Antimony

3.1 The Chemical Element

Antimony is a metallic element with the chemical symbol Sb, whose atomic number is 51, and is silvery-white, lustrous, very brittle and semiconducting. It has a density of 6,688 g/cm^3, its melting point is at 630.5 ºC and it has an average hardness (3.0 on the Mohs scale). Other physical properties of this metal can be found on Table 2 (Grund *et al.*, 2006; European Commission, 2014).

Table 2 – Physical properties of Antimony (Source: Grund et al., 2006).

Density	solid at 20 ºC	6.688 g/cm^3
	liquid at 630.5 ºC	6.55 g/cm^3
Melting point		630.5 ºC
Heat of fusion		10.49 kJ/mol
Boiling point at 101.3 kPa		1325 ºC
Modulus of elasticity		566 N/mm^2
Electrical resistivity at 0 ºC		30.0x10^{-6} Ω.cm
Thermal conductivity	at 0 ºC	18.51 W.m^{-1}.K^{-1}
	at 100 ºC	16.58 W.m^{-1}.K^{-1}

Antimony is considered a critical raw material (CRM) by the European Commission, according to the most recent list of CRMs provided in 2017. The EU has, currently, no primary extraction of antimony ores or concentrates, so its import reliance rate is 100%. The main producers of antimony in the world are China and Vietnam, with an average production of 87% and 11%, respectively (European Commission, 2017).

Antimony is one of the few CRMs that have a higher end-of-life recycling input rate (EOL-RIR), which measures the ratio between recycling and demand. The EOL-RIR for antimony is 28%, and this is possible due to one of the main uses of Sb being in batteries, which are well collected at their end-of-life, because of the waste legislation (Blengini *et al.*, 2017).

Even though the EU does not have any current mining of Sb, it does have some of the processing stages of the material (Figure 5). Belgium, Germany, France, Greece, Italy, UK, Netherlands, Romania and Slovakia are some of the important producers of antimony metal and antimony oxide (European Commission, 2014).

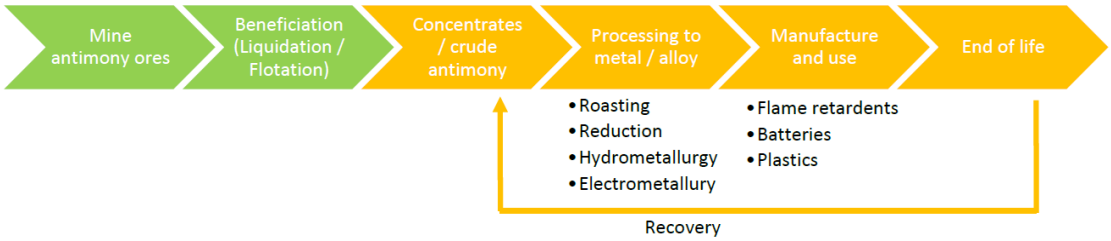

Figure 5 – Processing stages of antimony. In orange are the stages that take place in the EU. (Source: European Commission, 2014)

In Table 3 can be seen the production of several countries in the years 2017 and 2018, as well as their reserves. China is the country with the highest reserves, followed by Russia and Bolivia.

Table 3 – World antimony mine production and reserves. All values are in tons. (Source: Klochko, 2019).

	Mine Production		
	2017	**2018**	**Reserves**
United States	0	0	60.000
Australia	3.120	3.100	140.000
Bolivia	2.700	2.700	310.000
Burma	1.000	1.000	NA
China	98.000	100.000	480.000
Guatemala	25	25	NA
Iran	300	300	NA
Kazakhstan	700	700	NA
Laos	340	300	NA
Mexico	243	240	18.000
Pakistan	60	60	NA
Russia	14.400	14.000	350.000
Tajikistan	14.000	14.000	50.000
Turkey	2.000	2.000	100.000
Vietnam	380	300	NA
World total (rounded)	137.000	140.000	1.500.000

Antimony is mainly used as a trioxide in the chemical and plastic industries for flame-retardant compounds, but it is also used in alloys along with lead to increase its durability. These alloys are then used in batteries, low friction metals and cable sheathing. Antimony can also be used in paints, glass, and ceramics.

3.2 The Mineralizations

The average content of antimony on the Earth's crust is 0,2 to 0,5 ppm. Even though Sb occurs in more than 100 mineral species, the main antimony ore mineral is stibnite, a sulphide with the chemical formula Sb_2S_3. Stibnite occurs as black acicular crystals and contains around 71,7% of Sb (Llewellyn, 1992; Grund *et al*., 2006). Although stibnite is the main ore mineral of antimony, there are other important mineral species, such as, tetrahedrite ($Cu_6(Cu_4X_2)Sb_4S_{13}$), berthierite ($FeSb_2S_4$), stibiconite ($H_2Osb_2O_5$) and famatinite (Cu_3SbS_4).

Most of the antimony occurrences of the Iberian Peninsula are in the Central Iberian Zone (CIZ). In Portugal there are several antimony occurrences described, some in Trás-os-Montes (around Vimioso, Macedo de Cavaleiros, Mogadouro and Mirandela), others in the Alto Douro area (in Vila Nova de Foz Côa), in the Baixo Douro area (also known as the Dúrico-Beirã Region) and in Castelo Branco. The mineralizations occur essentially

in veins in formations of the Silurian (in Trás-os-Montes) and in the Schist-Greywacke Complex (in the Alto Douro area). In the Baixo Douro area the mineralizations occur in various lithologies, so there is not a single lithological control (Gumiel, 1983).

According to Gumiel (1983) in a regional scale, a spatial relation can be made between the antimony mineralizations and (1) the Palaeozoic anticline-syncline structures and (2) the post-orogenic granites that intruded the Palaeozoic and Pre-Ordovician formations at NE. At a grand scale it can also be found a spatial correlation between the mineralizations and dikes of basic rocks.

There are several different classifications of the antimony deposits, some of which are described in the following paragraphs.

According to morphology, Gumiel & Arribas (1987) differentiated 3 types of antimony deposits. The first is *vein-type deposits* that consist essentially of “crosscutting vein systems of small extents” with lenticular shapes and pinching and swelling structures associated. These veins are often found in Precambrian rocks, even though there’s no lithological control of the veins. The second type is *strata-bound deposits*. This type of deposit occurs in calcareous or sandy shales, in addition to a few siliceous layers. These deposits can be associated to intraformational breccias and seem to be controlled lithostratigraphically and structurally. The final type is *antimony deposits in volcanic dikes*. These are associated with post-orogenic volcanism where the mineralization occurs in both the host-rocks and the dikes.

According to this it can be assumed that the origin of antimony deposits can be explained by direct or indirect magmatic processes, but there are also some deposits that are strata-bound, where antimony is restricted to certain beds of host rocks and that appear to be syngenetic (Gumiel & Arribas, 1987). In Figure 6 can be seen all the deposits studied by Gumiel & Arribas (1987) according to the type of deposits and to its host rocks.

Gumiel & Arribas (1987) also divided antimony deposits in 8 different types, this time according to the mineral associations, based on the ones found in the Iberian Peninsula:

1. Quartz-stibnite: this is the most common association where the veins are mostly quartz and stibnite, but sometimes can be found arsenopyrite and iron sulphides, although scarcely. In this type of deposits galena is always absent and berthierite can occur included in stibnite. This being the most common paragenesis it can be found in numerous deposits, some examples are the Pinheirinhos and Corgo, in Oporto, Portugal and Pandeiro, in Ordenes, Spain.

2. Quartz-stibnite-gold: in these quartz veins the mineral assemblage is stibnite, arsenopyrite, pyrite and native gold. Gold can be associated to quartz, pyrite or arsenopyrite. The veins usually have pinching and swelling structures, and stibnite occurs in irregular pockets. In Portugal these types of deposits are often found in the pre-Ordovician Schist-Greywacke Complex. One example of this type of deposits is Alto do Sobrido, in Oporto.
3. Carbonate-quartz-stibnite-sphalerite-gold: these deposits are characterized by the early deposition of pyrite, arsenopyrite and accessory gold included in stibnite. There are other minerals that also appear included in stibnite, such as chalcopyrite, sphalerite and tetrahedrite. The last mineral in the deposition sequence is stibnite with inclusions of berthierite, and this is the main mineral of this paragenesis. The gangue is composed essentially of quartz and calcite. One example of this type of mineralization associations is the Ribeiro da Igreja mine, in Oporto.
4. Carbonate-quartz-stibnite-galena-silver: there is only one deposit with this type of association, which is the Diógenes mine, in Ciudad Real, Spain. Its deposition sequence starts with the formation of pyrite, ullmannite and chalcopyrite. After this, there is an enrichment in Pb and Pb-Sb, primarily with the deposition of galena and afterward with the formation of iron sulfoantimonides. Lastly, it occurs the deposition of Sb-Ag sulfosalts, filling the spaces available. In this case the gangue is mainly composed by carbonates, with quartz being rare.
5. Quartz-stibnite-sphalerite: this association consist essentially of sphalerite, which forms first, and stibnite with inclusions of berthierite. Associated with these are also pyrite and chalcopyrite. The gangue in this type of deposits is essentially made of quartz and, scarcely, carbonates. One example of this type of deposit is the Nazarena mine, in Ciudade Real, Spain.
6. Quartz-stibnite-scheelite: this paragenesis was firstly described in the San Antonio ore deposit, in Extremadura, Spain, and it corresponds to a strata-bound mineralization where the main ore minerals are stibnite, scheelite, berthierite and pyrite. Associated with these there are some secondary minerals, such as stibiconite, cervantite and goethite. The gangue, although very scarce, consists solely of quartz and calcite.
7. Quartz-stibnite-mercury: this type of association has only been described in the Cantabrian Zone, in the sheared limestones of the Carboniferous from Mieres, Riaño, Pola and Somiedo, in Spain. Its paragenesis includes realgar, orpiment, pyrite, cinnabar, stibnite and minor arsenopyrite. In the gangue can be found quartz, carbonates and fluorite.

8. Quartz-stibnite-copper: this paragenesis is characteristic of the southern part of the Hercynian belt (South Portuguese zone) and consists in arsenopyrite, chalcopyrite and famatinite, which always form before stibnite. The main mineral in this association is stibnite, but it can easily be replaced by antimony oxides. There can be found remains of berthierite in stibnite. Some examples of this type of association are the Accesos mine, in Cordoba, Spain, the Sierra Morena 2ª, also in Cordoba, and the Nerón mine, in Huelva, Spain.

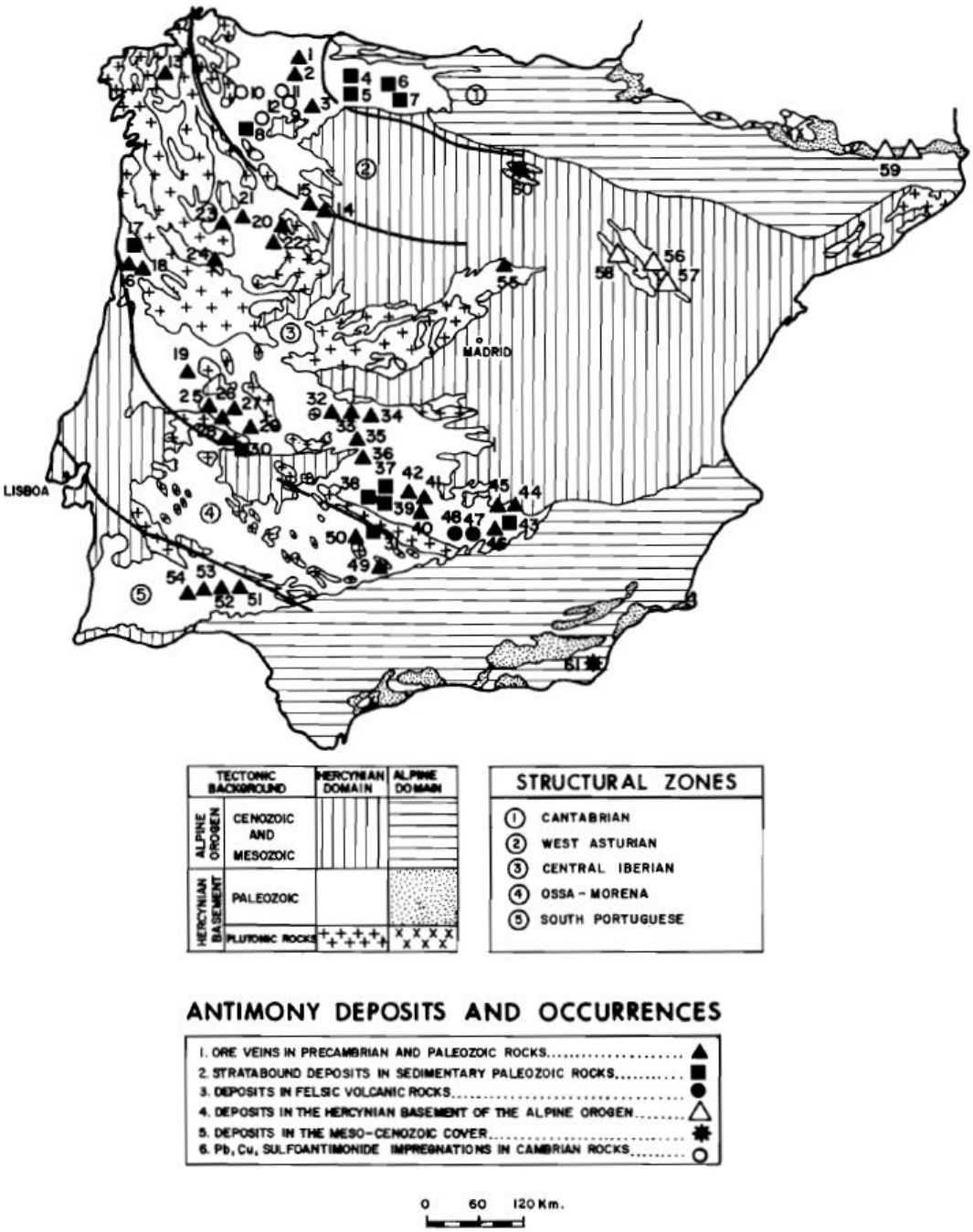

Figure 6 – Location of antimony deposits and occurrences in the Iberian Peninsula according to their types and host rocks (Source: Gumiel & Arribas, 1987).

Couto (1993) separated 4 types of deposits according to the distinct paragenetic associations found in the Dúrico-Beirã Region:

1. Sb-Au
2. Au-As
3. Pb-Zn(-Ag)
4. Sn-W

Within the different associations Couto *et al*. (1990) described up to 5 stages of evolution of the mineralization according to the fracturing episodes.

- Stage 1: Iron-Arsenic
- Stage 2: Zinc
- Stage 3: Lead-Antimony
- Stage 4: Antimony
- Stage 5: Remobilization

Every occurrence has its own paragenetic evolution, which may or may not include all these stages.

The Sb-Au and Au-As paragenesis result from the same metallogeny process but differ in the paragenetic stages, with the Au-As association having a bigger development in the Fe-As stage and the Sb-Au association developing the Sb stage more. The Sn-W associations occur close to the outcropping granites. The Pb-Zn(-Ag) associations occur due to an over-imposition of Pb-Zn fluids on the pre-existing Sb-Au mineralizations (Couto, 1993).

According to Couto (1995) the paragenetic evolution that resulted in these associations occurred in two different processes: one Hercynian, dominated by either the Sb-Au or the Au-As associations; the second Post-Hercynian, tied to the opening of the Atlantic, where the formation of the Pb-Zn(-Ag) associations occur, due to the remobilization of Sb by the Pb-Zn fluids.

According to Couto et al. (2007) there is an indirect genetic relationship between the Sb-Au mineralizations and hidden granites, due to: (1) the presence of minor Sn and W minerals in the Iron-Arsenic stage in some Sb-Au deposits (Ribeiro da Igreja, Vale do Inferno, Montalto, Pinheirinhos, Tapada) that suggests a connection concerning the Sb-Au and the Sn-W mineralizations; (2) the occurrence of veins of acid igneous granitoid rocks in Ribeiro da Serra, whose emplacement is prior to the mineralizations and latter to the major folding phases suggests the existence of an acidic magmatic activity immediately preceding the metallogenic event; (3) apatite occurs commonly in Tapada

mine (in quartz veins) and in Ribeiro da Igreja mine (in quartz stockwork). These apatites were compared to the ones found in the granitic intrusions close to the Dúrico-Beirão District, through cathodoluminescence studies. This showed that the apatites from the granites and the Tapada mine were very different, and the ones in Ribeiro da Serra showed properties intermediate to the other two. It was clear that there was an attenuation of the magmatic origin of the apatites.

Llewellyn (1992) and Grund *et al*. (2006) make a different division on the types of Sb deposits. They describe two types of Sb deposits: simple and complex. Both types are formed due to hydrothermal fluids of low temperature, at shallow depths. Usually, Sb mineralization is found in veins, but it can also occur as irregular masses (Llewellyn, 1992; Grund *et al*., 2006; Moura & Velho, 2012).

The simple antimony deposits are composed essentially of stibnite, or, rarely, native antimony, in a siliceous gangue. These usually contain pyrite and, in some areas, small amounts of other metal sulphides (typically silver and mercury sulphides) and very small amounts of gold. These types of deposits are found in the most productive antimony districts, such as the ones in Bolivia, China, Mexico and the Republic of South Africa, and each of them doesn't contain more than several thousand tons of ore (Llewellyn, 1992; Grund *et al*., 2006).

The complex antimony deposits can have two different compositions: the first one consists of stibnite associated with pyrite, arsenopyrite, cinnabar or scheelite; the second one consists of antimony sulfosalts with differing amounts of copper, lead and silver, in addition to common sulphides of these metals and zinc. These types of deposits are normally mined primarily for gold, lead, silver, tungsten or zinc, with antimony being mined as a by-product (Llewellyn, 1992; Grund *et al*., 2006).

Neiva *et al.* (2008) also described a classification according to the abundances of the main ore minerals which was based on the previous works and publications of Portugal Ferreira *et al*., 1971; Santarém Andrade & Portugal Ferreira, 1976; Couto *et al*., 1990; Noronha *et al*., 1998. This classification was created for the existing assemblages in northern Portugal and they are:

1. Quartz + stibnite for Sb-quartz veins
2. Quartz + pyrite + galena + berthierite for Pb-Sb-quartz veins
3. For the Sb-Au-quartz veins there are three different assemblages:
    a. Quartz + sphalerite + stibnite
    b. Quartz + pyrite + berthierite + stibnite
    c. Quartz + arsenopyrite + pyrite + stibnite

3.3 The Occurrences

As it was mentioned previously, most of the antimony mineralizations of the Iberian Peninsula are located within the CIZ. Some of those are in the Dúrico-Beirã Region, around the Valongo Anticline.

The mining of the mineralizations in the Dúrico-Beirã Region started in the Roman Era, when the romans were attracted to the gold existing in this area. When it comes to antimony the first deposits were found in 1807 (Vale das Achas e Ribeiro da Igreja), and its mining only started in 1858 (Gumiel, 1983; Couto, 1993).

In 1880 the mines of Tapada and Ribeiro da Igreja started exploiting, along with the Montalto mine in 1881. This last mine was one of the most productive in the region. The mining of antimony deposits reached its peak between 1870 and 1890, and it was concentrated in a band of about 5 Km from Covelo to Alto do Sobrido. In the beginning of the 20th century the antimony production practically stopped, with only a few mines being able to produce up to 1971. In 1990 the Banjas and Moirama mines reopened (Gumiel, 1983; Couto, 1993).

Couto (1993) divided the Dúrico-Beirã Region in 5 sectors according to the mineralogic variety and to the paragenetic associations:

1. Ribeiro da Igreja – Vale do Inferno Sector (Sb-Au)
2. Montalto Sector (Sb-Au)
3. Alto do Sobrido – Ribeiro da Serra Sector (Sb-Au)
4. Banjas Sector (Au-As)
5. Terramonte Sector (Pb-Zn-Ag)

Within these sectors there are several mines that can be observed in Figure 7. There are also some of the mines that are not included in any of the sectors. In this chapter will only be described the first three sectors, along with three antimony mines that are not included in any of the five sectors.

According to Couto (1993) there were considered 4 groups of strikes and dips for mineralized structures in the Dúrico-Beirã Region: (1) Strike: ENE-WSW; Dip: S, E, SE; (2) Strike: E-W; Dip: NE; (3) Strike: N-S; Dip: E; (4) Strike: NNW-SSE.

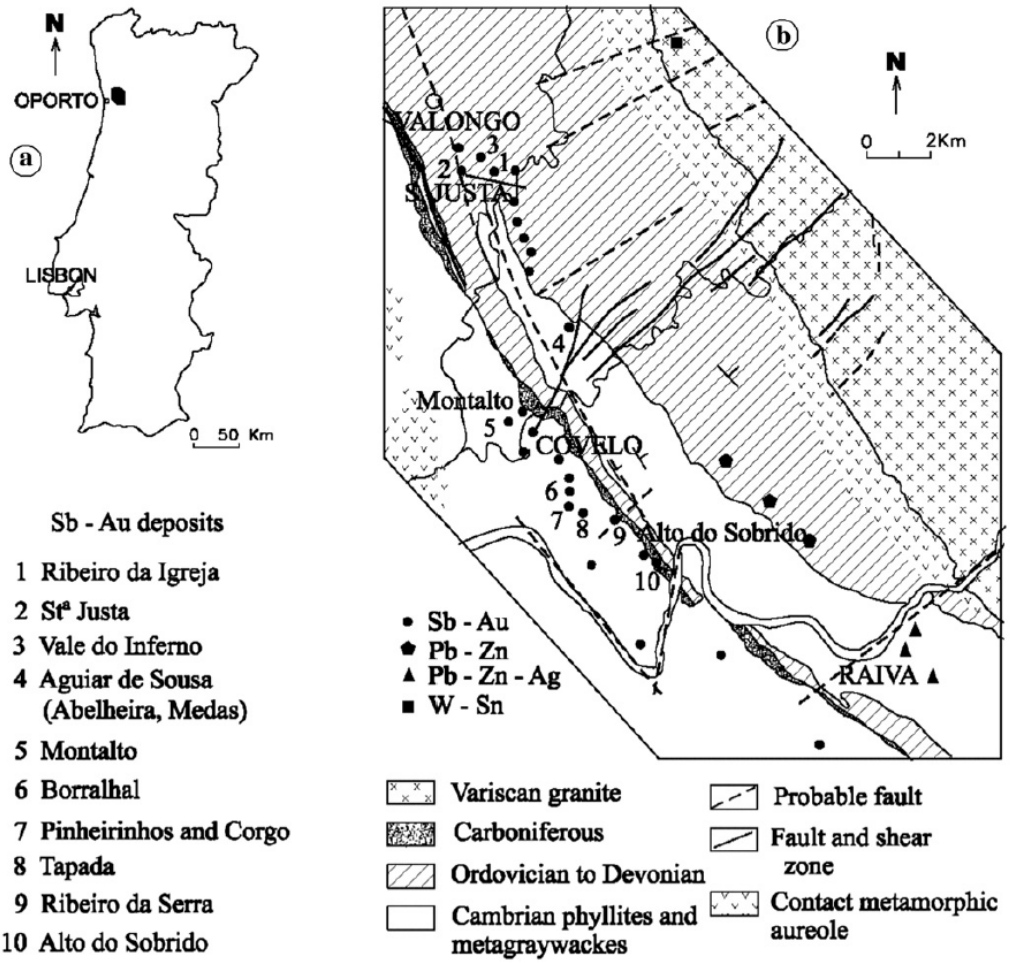

Figure 7 – (a) location of the Dúrico-Beirã Region in the map of Portugal; (b) Locations of the different antimony deposits within the Dúrico-Beirã Region and their type. (Source: adapted from Couto et al. 1990 in Neiva et al. 2008).

The **Ribeiro da Igreja-Vale do Inferno Sector (Sb-Au)** contains the Ribeiro da Igreja, the Vale das Achas and the Vale do Inferno mines. There are currently no traces of the Vale das Achas mine due to the urbanization of the area. This sector is located in the eastern flank of the Valongo Anticline.

The mineralized structures of the mines in this sector occur within the alternations of the Santa Justa Formation (Lower Ordovician), although they also appear in the schists and siltstones of the Valongo Formation (Medium Ordovician). These host rocks correspond to alternating sandstones, quartzites, siltstones and schists, with a very disturbed sedimentary deposition and some volcano-sedimentary levels (Gumiel, 1983; Couto, 1993). The mineralization occurs with three preferable strikes, from the most dominant to the least: NE-SW; E-W; N-S (Couto, 1993).

In the Ribeiro da Igreja mine occur all the five stages of the paragenetic evolution (Figure 8) described by Couto *et al*. (1990). In the Vale do Inferno case, the paragenetic evolution only has 3 stages, the Iron-Arsenic stage, the Antimony stage, and the Remobilization stage (Couto, 1993).

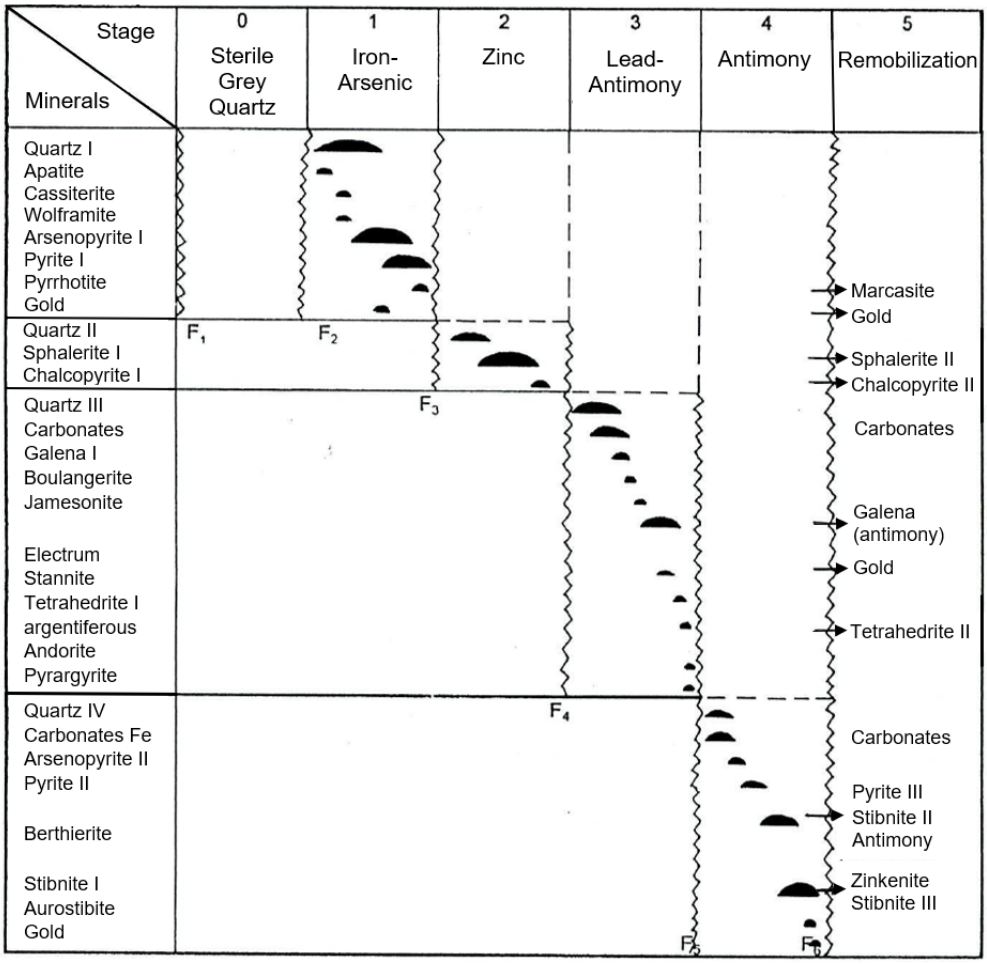

Figure 8 – Paragenetic evolution of the mineralizations from Ribeiro da Igreja (translated from Couto et al., 1990).

In Ribeiro da Igreja and Vale do Inferno mines, tungsten mineralizations were found as wolframite automorphic crystals in quartz (Couto et el. 1990) and as wolframite surrounded by stibnite (Neiva, 1944 *in* Couto, 1993), respectively.

According to Couto (1993) the mineralizations of this sector appear to have both lithological and structural control. The mineralization occurs essentially within the Lower Ordovician Formations and seems to be associated to dark layers with organic matter and sulphides. The veins are installed in shearing fractures.

The second sector is the **Montalto Sector (Sb-Au)** which includes the Montalto mine, one of the most important due to size and content in antimony and gold (Carvalho, 1964 *in* Couto, 1993). This sector is located in the inverse flank of the Valongo Anticline.

The veins found in the galleries of the Montalto mine occur with a strike of NNW-SSE and the host rocks for these veins are the conglomerates of the top lithologic association of the Montalto Unit (Precambrian and/or Cambrian(?)), with intercalations of pelitic levels. There was also a vein found within Carboniferous Formations striking E-W (Couto, 1993).

The mineralization that occurs in the Montalto mine is structurally controlled by an important shear zone, called Douro Shear Zone, and its paragenetic evolution contains four stages (Figure 9): (1) Iron-Arsenic; (2) Zinc; (3) Antimony; (4) Remobilization.

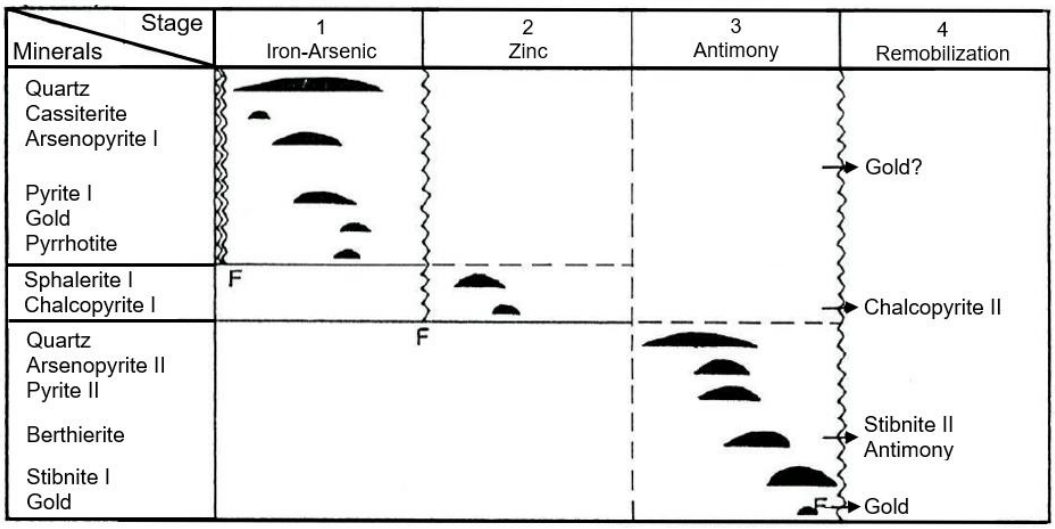

Figure 9 – Paragenetic evolution of the mineralizations from Montalto mine (translated from Couto, 1993).

The last sector that will be described in this chapter is the **Alto do Sobrido – Ribeiro da Serra Sector (Sb-Au)** which is located in the western flank of the Valongo Anticline. In this sector can be found the Alto do Sobrido and the Ribeiro da Serra mines.

The Alto do Sobrido mineralizations occur near the contact between the Precambrian and/or Cambrian(?) and the Carboniferous. The host rocks consist in schists alternating with quartzites of the Precambrian and/or Cambrian(?) (Alto do Sobrido Unit), as well as in the breccia of the base of the Carboniferous up to the sandstone that corresponds to mud seeps described by Jesus (1986) (*in* Couto, 1993). The mineralized veins strike mainly towards €NE-(W)SW, although there's a stockwork that strikes NNW-SSE (Couto, 1993).

According to Couto (1993) the paragenetic evolution in Alto do Sobrido is composed by five stages (Figure 10). The Iron-Arsenic stage appears to be less important than the one observed in the occurrences of the eastern flank. There is no Zinc stage in this deposit, and the Lead-Antimony stage is represented by Jamesonite which is scarce. The Antimony stage is divided in two different stages due to a clear fracturing episode present between the deposition of berthierite and the deposition of stibnite.

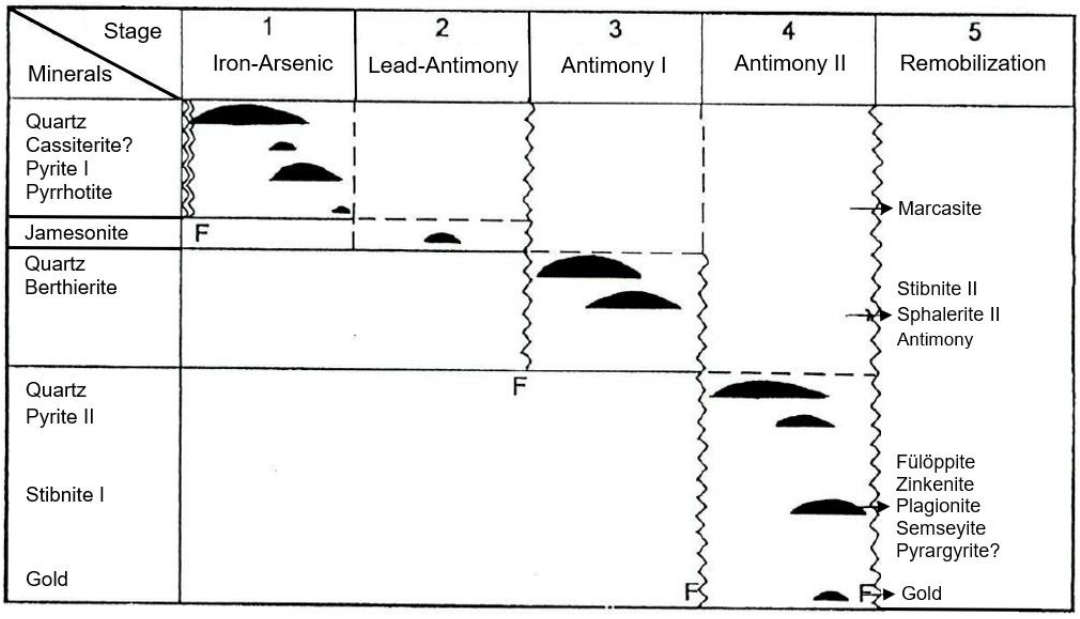

Figure 10 – Paragenetic evolution of the Alto do Sobrido mine (translated from Couto, 1993).

The Ribeiro da Serra mine includes the concessions of Ribeiro da Serra and Fontinha. In this deposit the mineralization occurs within Precambrian and/or Cambrian(?) Formations, but unlike Alto do Sobrido, it isn't near the contact with the Carboniferous. The mineralized veins consist in a breccia formed by elements from the host rocks (schist and quartzite) with lenticular white quartz fillings. Their strike varies from N-S to E-W (Couto, 1993).

According to Gumiel (1983) the mineralizations from Ribeiro da Serra and Fontinha are an extension of the veins from Alto do Sobrido.

The paragenetic evolution of Ribeiro da Serra consists of three stages (Figure 11): iron-arsenic, antimony and remobilization. Contrary to what happens in Alto do Sobrido, here there is no evidence of a fracturing episode between the deposition of berthierite and stibnite.

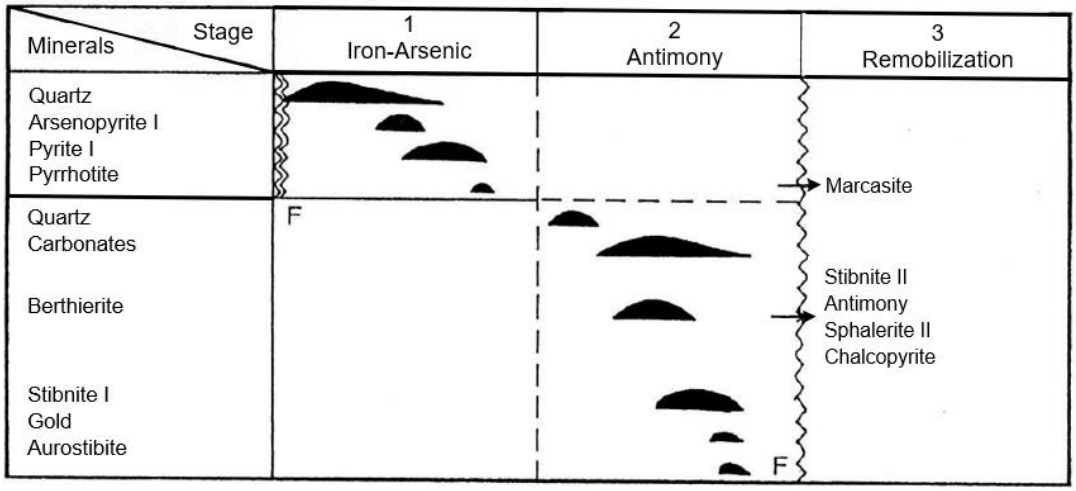

Figure 11 – Paragenetic evolution of the Ribeiro da Serra mine (translated from Couto, 1993).

The variation on the strikes found in the Alto do Sobrido-Ribeiro da Serra Sector is due to a structural control of the mineralization. In the Remobilization stage of this sector (specially in Alto do Sobrido) the presence of sulfosalts such as Plagionite and Zinkenite indicate a substitution of the Sb and Fe for the Pb-Zn-Ag in which the fluids are rich (Couto, 1993). This remobilization reaction between the fluids and the mineralization has been demonstrated in antimony occurrences in Hercynian areas in France (Möelo et al., 1978 *in* Couto, 1993) and in the Marrocos Central Hercynian Massif (Kosakevich & Möelo, 1982 *in* Couto, 1993).

Next will be described the three mines that do not belong in any of the sectors: the Tapada mine, and the Pinheirinhos and Corgo mines. All these mines belong to the Sb-Au type.

In the Tapada deposit the veins occur within pelitic rocks alternating with sandstones of Precambrian and/or Cambrian(?) ages. Near these can be found diabase dikes that can reach 20 meters of thickness (Couto, 1993).

The paragenetic evolution of this mine has 3 stages (Figure 12) with the antimony stage being the dominant one. In this deposit, carbonates are more abundant then in the neighbour mines of Ribeiro da Serra and Alto do Sobrido (Couto, 1993).

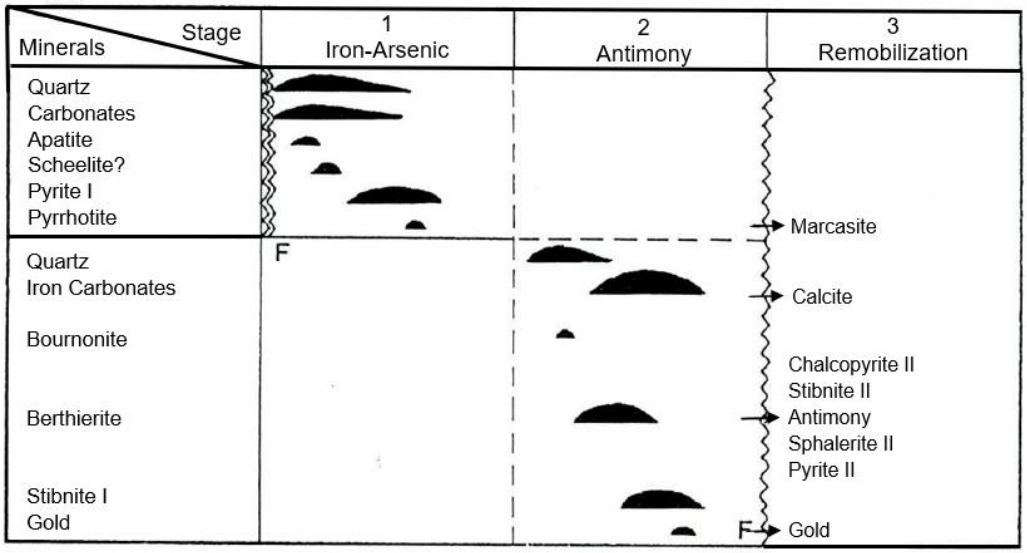

Figure 12 – Paragenetic evolution of the Tapada mine (translated from Couto, 1993).

In the Pinheirinhos and Corgo mines the mineralizations are observed in Precambrian and/or Cambrian conglomerates that can be correlated with the top association of the Montalto Unit.

According to Couto (1993) the paragenetic evolution of the Pinheirinhos deposit has 5 stages (Figure 13), with two of them being interrogated. This is because galena and sphalerite have never been found in this mine's paragenesis before.

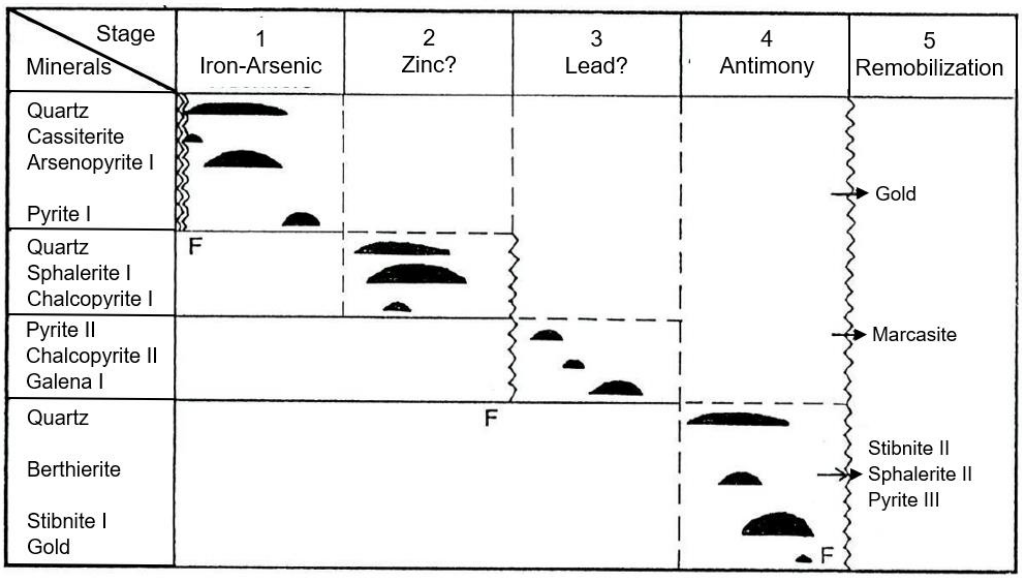

Figure 13 – Paragenetic evolution of the Pinheirinhos mine (translated from Couto, 1993).

3.3.1 Alto do Sobrido Previous Works

As mentioned previously the area used for geophysical methods is restricted to the Alto do Sobrido Sector (Figure 1). This is an area where a lot of exploration work has been done. Some of which will be described in the following paragraphs.

As was on most of the Dúrico-Beirão Mining District, Alto do Sobrido was firstly explored by the Romans for the gold. Here, their works are shown in small underground galleries and open pits located near the contact between the CXG and the base of the Ordovician with the Carboniferous. These works were focused on hydrothermal quartz veins (Parra & Filipe, 1997; Ramos, 1997).

From 1870 to 1970, the Serviço de Fomento Mineiro (SFM) and the Sociedade Mineira do Alto do Sobrido, have performed geological studies in the area that were able to reach a resources evaluation. These studies consisted on the geological cartography of both the surface (1:2.500 scale) and the underground (1:100 scale), mineralogical study of 30 rock samples, sampling in galleries and respective geochemical analysis for elements such as Au, Ag and Sb, and resources evaluation for the quartz veins. These studies revealed that the gold-antimony mineralizations in veins do not have economic interest (Parra & Filipe, 1997).

Between 1988 and 1993, the Consórcio do Baixo Douro (CBD) also studied the Alto do Sobrido area, with a research and exploration contract that included the Dúrico-Beirão Mining District. This started with a strategic geochemical exploration. The anomalous zones located with the strategic exploration were then targeted with a tactical exploration that included: soil geochemical studies, geological cartography at a scale of 1:2.500 and rock sampling. All these studies proved the existence of gold mineralizations in quartz

stockwork and silicified bands, besides the already known quartz veins. In conclusion the CBD determined that there is some potential in the mineralizations of antimony and gold in the areas of Montalto-Tapada-Alto do Sobrido, however these required further exploration (Parra & Filipe, 1997).

In 1994, the Departamento de Avaliação (DA) decided to research the Alto do Sobrido area with the objective of finding gold and antimony mineralizations with economic potential. Up until the end of 1995, they have done a geological study that consisted of cartography of the surface and the underground, as well as structural reinterpretation and sampling of promising structures. This allowed them to: (1) prove that the gold occurrences are not limited to veins, but also happen in fractures and pores of the host rocks; (2) define lithostratigraphic and structural associations to the gold-antimony occurrences; (3) identify Au-Sb resources, in both stockwork and silicified bands, with a spatial positioning propitious to open pit exploration that they were able to quantify (Parra & Filipe, 1997).

More recently, from 2007 to 2010, Kernow Mining Portugal also studied the area of Montalto, Tapada, Pinheirinhos, Corgo, Fontinha, Ribeiro da Serra, Alto do Sobrido and Rebentão, with a research and exploration contract. During this contract they have reviewed previous works, confirmed and corrected some details on the geological cartography of the area, collected several samples, both on the surface and in galleries, reanalysed drilling core samples that were previously done, and did a calculation of the potential for Sb resources existing in the area. With all the studies, Kernow Mining concluded that, with the current prices, the mining of the area would not be viable, which led them to not proceed with the project (Kernow Mining Portugal, 2010).

4. Spatial Analysis of Geochemical Data

4.1 Method

For the geochemical study on this project were utilized stream sediment location points, along with their chemical element analysis, provided by the Consórcio do Baixo Douro (CBD), in order to create drainage basins to see the areas with higher concentrations of certain elements. This process was made with the software ArcGIS, version 10.7.1.

The stream sediment data consists of 1673 samples, that were gathered throughout the entire Valongo Anticline.

Firstly, in this method it is essential to have water lines, which can be obtained from a digital elevation model (DEM). DEM is a raster that shows the elevation on each cell. It is important that it has the best pixel resolution possible, so that the resulting water lines are as close to reality as possible. To have a faster processing, a clipping of the DEM to the study area was done.

Most of the tools used on this method can be found on ArcToolbox's Spatial Analyst Tools within the Hydrology tab.

Using the DEM, a Flow Direction Raster (FD) can be created, with the flow direction tool on ArcGIS. The FD displays the direction of water flow from each cell to its downslope neighbours. In this case there was no need to do this step because Portugal's Flow Direction Raster (Figure 14.A) is available on the Sistema Nacional de Informação de Ambiente website (https://sniamb.apambiente.pt/content/geo-visualizador).

Having FD, it is possible to obtain the Flow Accumulation raster (FA) (Figure 14.B), through the Flow Accumulation tool. This raster shows the accumulated flow on each cell, i.e., shows the water lines. Once FA is available, using the Stream Order tool, the water lines get assigned a numeric order to each cell (Figure 14.C). With this it is possible to distinguish the main water lines (higher values) from their tributaries (lower values).

To avoid the clutter of pixels from the lowest valued tributaries, a hollow colour was assigned to them. It is also possible to apply a conditional on the Stream Order raster, using the Raster Calculator tool on the Map Algebra tab of Spatial Analyst Tools, to only keep the lines with a value higher than 2 (Figure 14.D), for example, but for some stream sediment points the lower valued tributaries were required for their correction, which is discussed in the following paragraphs. This conditional raster can be converted to points using the tools on the Conversion Tools' from Raster tab. The last two steps are not strictly necessary but help with the correction of stream sediment points that will follow.

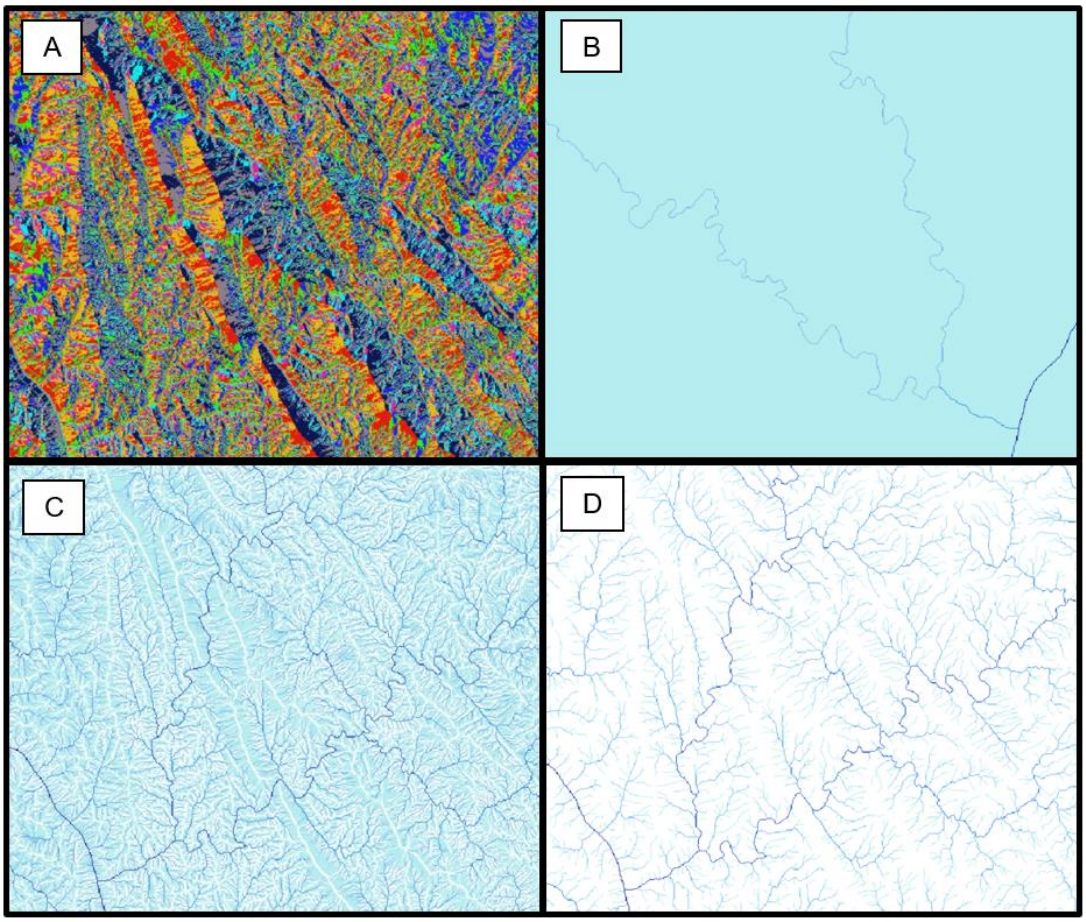

Figure 14 - Steps for the creation of water lines: A - Flow Direction; B - Flow Accumulation; C - Stream Order; D - Stream Order with conditional. (Obtained using ArcGIS software).

With the water lines created, the correction of the stream sediment points' locations can proceed. These points need to be on top of a water line, for the creation of the basins to work. Due mainly to GPS errors, not all the points fall on the water lines, and so they need correction. With the help of the sampling maps, such as the example shown on Figure 15, and using the editor tools on ArcGIS, it is possible to move the points to their correct location. Here is where the points' shapefile of the water lines will help, because by using the snapping tools on the editor, it is certain that the points will land on the water lines.

As was mentioned previously, sometimes it is necessary to place the points on water lines of lower values, in order for the basins to be created.

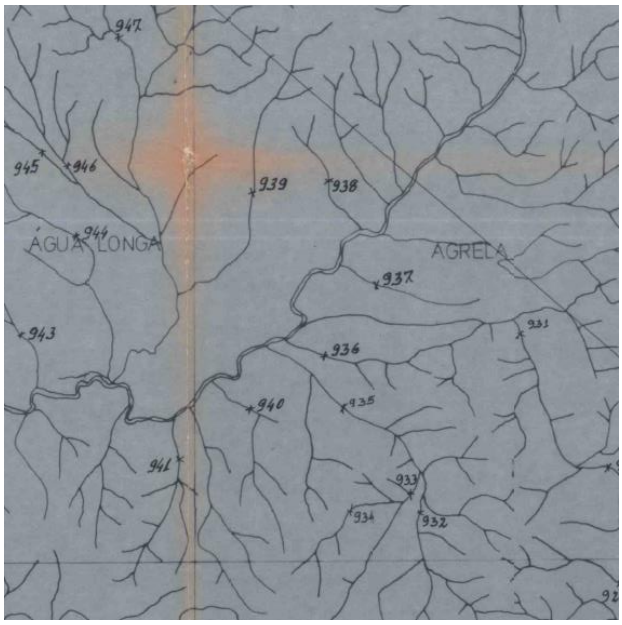

Figure 15 - Cut of a stream sediment sampling map that was provided with the stream sediment data by CBD.

Once every single stream sediment point is corrected, the creations of the basins can be done. To do so the Watershed tool, on the Hydrology tab is used. This tool uses FD and the stream sediment points to create a raster with the basins associated to each point (Figure 16). It was important to change the processing extent in the Environments to "same as layer [name of the stream order raster]" so that the basins appear with their full extent.

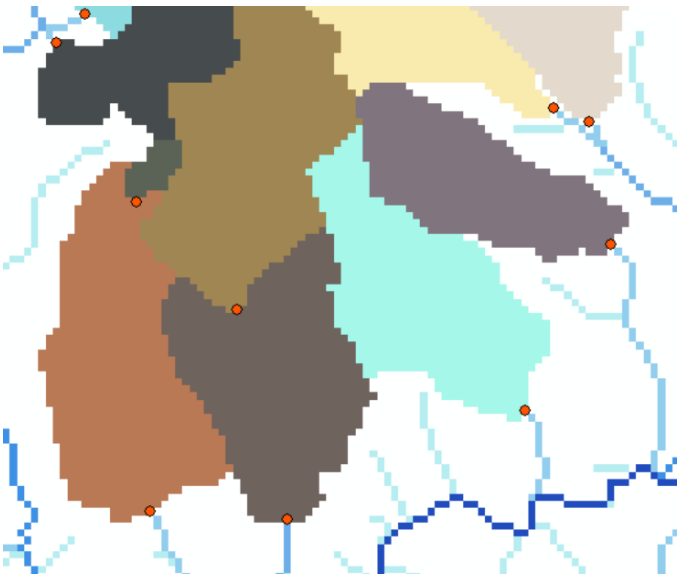

Figure 16 - Cut of the basins generated with the Watershed tool, with the stream sediment points (in orange) used as the control points (Obtained using ArcGIS software).

The basins created with watershed are then converted to a polygon shapefile with the conversion tools. With this conversion there might be more than one polygon that belongs to the same basin. To correct this, it was required to use the Dissolve tool (on Geoprocessing) and select gridcode on the dissolve fields.

To transfer the chemical analysis information from the stream sediments to the basins the Spatial Join tool (ArcToolbox→Analysis Tools→Overlay→Spatial Join) was used, where the target features are the basins, and the join features are the stream sediment points.

Once all the steps are completed, using the symbology tab in properties, it is possible to display the concentration of each element on the basins, with an appropriate colour ramp. These concentration variations within the drainage basins will be demonstrated on the following chapter.

4.2 Results and Discussion

It is possible to determine the locations where an element can be found in higher concentrations through the creation of drainage basins from stream sediment data, with chemical data associated.

As mentioned before, the stream sediment data used in this thesis was gathered by CBD in 1988, and it includes 1673 stream sediment samples, that were collected throughout the entirety of the Valongo Anticline (Figure 17). A chemical analysis was done to these samples and the concentration of several elements of interest was determined.

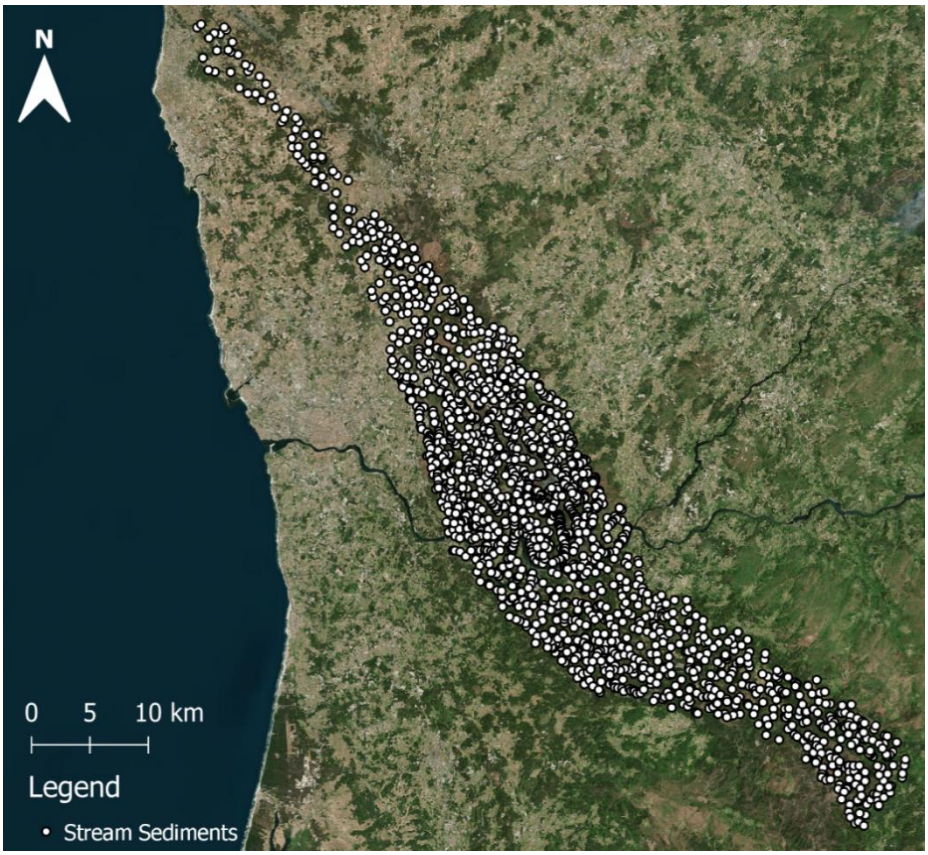

Figure 17 - Location of stream sediment samples gathered throughout the Valongo Anticline by CBD (image obtained with QGIS).

This work will focus on the concentrations of Sb, Au, As, Ag, Pb, Zn, Sn and W, due to them being the ones of higher interest in the Dúrico-Beirã Region. The minimum, maximum and mean values for each of these elements' concentrations, as well as their 75th, 90th, 95th and 99th percentiles can be found on Tables 4 and 5.

Table 4 - Minimum, maximum and mean values of concentrations in ppm of Sb, Ag, As, Sn, W and Pb, and in ppb of Au, from the stream sediment data.

	Sb	Au	As	Ag	Pb	Zn	Sn	W
Minimum	0	0	0	0	0	0	0	0
Maximum	9583	1000	1360	36,9	4600	3959	209	2102
Mean	27,5	38,5	36,3	0,2	51,1	125,3	8,2	7,2

Table 5 - Percentiles (75th, 90th, 95th and 99th) of the concentrations in ppm Sb, Ag, As, Sn, W and Pb, and in ppb of Au from the stream sediment data.

Percentiles	Sb	Au	As	Ag	Pb	Zn	Sn	W
75th	13	20	43	0,1	54	144	8	3
90th	27	60	74	0,2	71	181	15	9
95th	51	140	104	0,3	88	215	20	17
99th	249	516	238	2	174	349	41	76

As determined by Couto (1993) there are four different associations for these elements, which are Au-Sb, Au-As, Pb-Zn(-Ag) and Sn-W. In the following paragraphs and maps, it will be possible to observe the locations of the highest concentrations of each element. Which, in this case, means mostly the concentrations above the 99th percentile.

When it comes to antimony these locations correspond mainly to the areas of known occurrences (Figure 18). These are Ribeiro da Igreja, Abelheira, Ribeiro da Serra, and Alto do Sobrido.

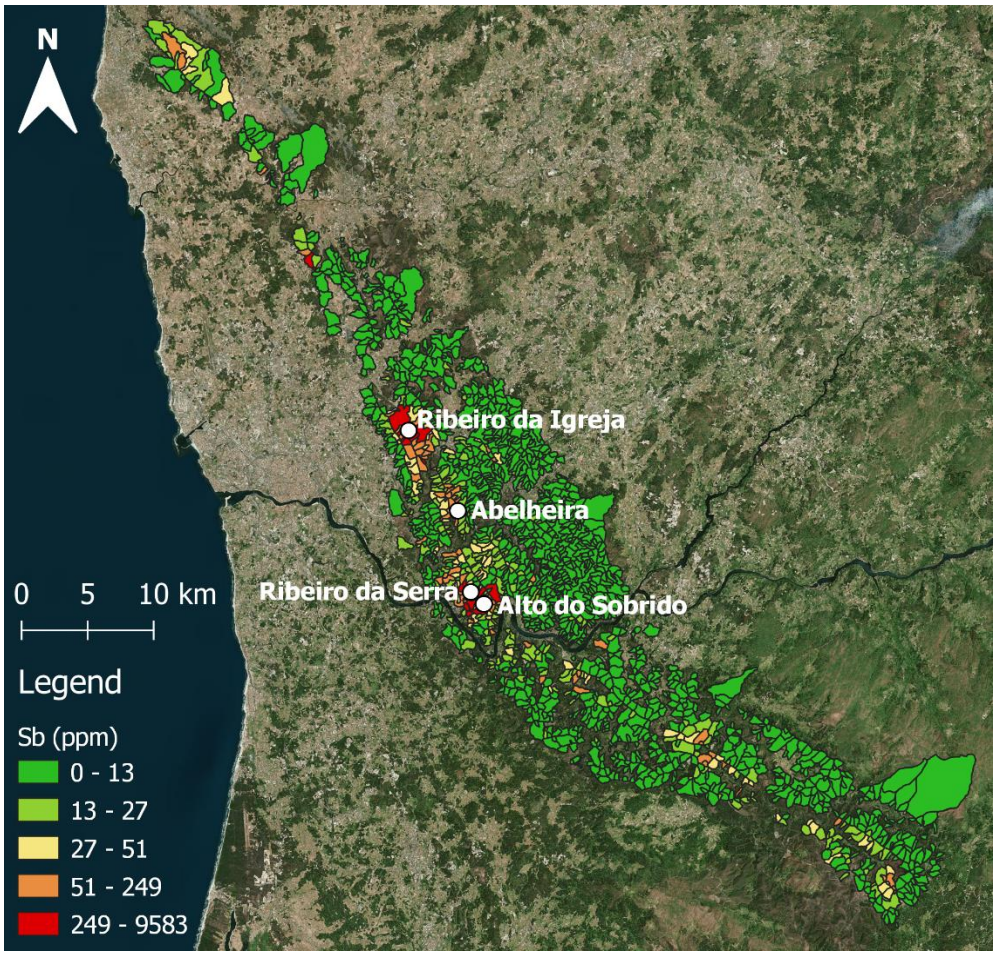

Figure 18 - Antimony concentrations on the drainage basins, and location of the highest concentrations marked by white circles (image obtained with QGIS).

In the area of Ribeiro da Serra can also be found the occurrences of Tapada, Pinheirinhos, Corgo and in the area of Ribeiro da Igreja can be found the occurrences of Vale das Achas, all of which are not marked on these maps, in order to not clutter them.

The highest gold concentrations coincide with the highest antimony concentrations in some locations, such as Ribeiro da Igreja, Ribeiro da Serra and Alto do Sobrido. But there are also other locations with high concentrations of Au, them being Banjas, Coiro de Boi and Montalto (Figure 19).

The highest concentrations of arsenic (1360 ppm and 763 ppm) can also be observed in Ribeiro da Serra and Alto do Sobrido. Other high concentrations of this element can be found at Castromil and Banjas (Figure 20).

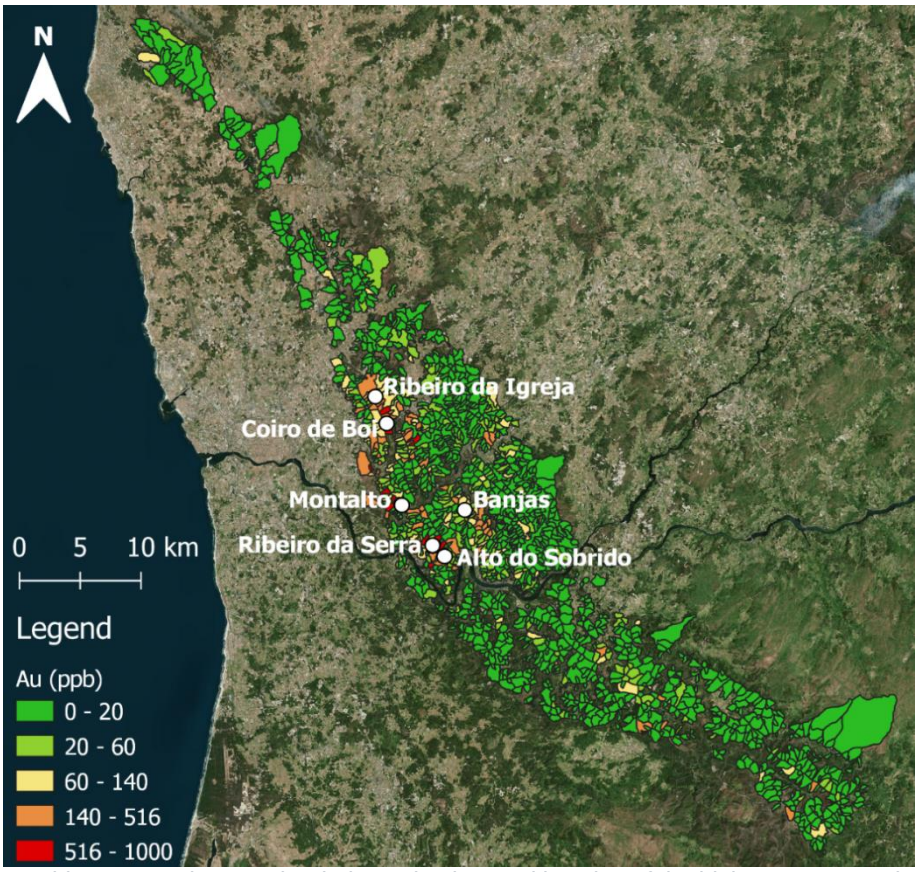

Figure 19 - Gold concentrations on the drainage basins, and location of the highest concentrations marked with white circles (image obtained with QGIS).

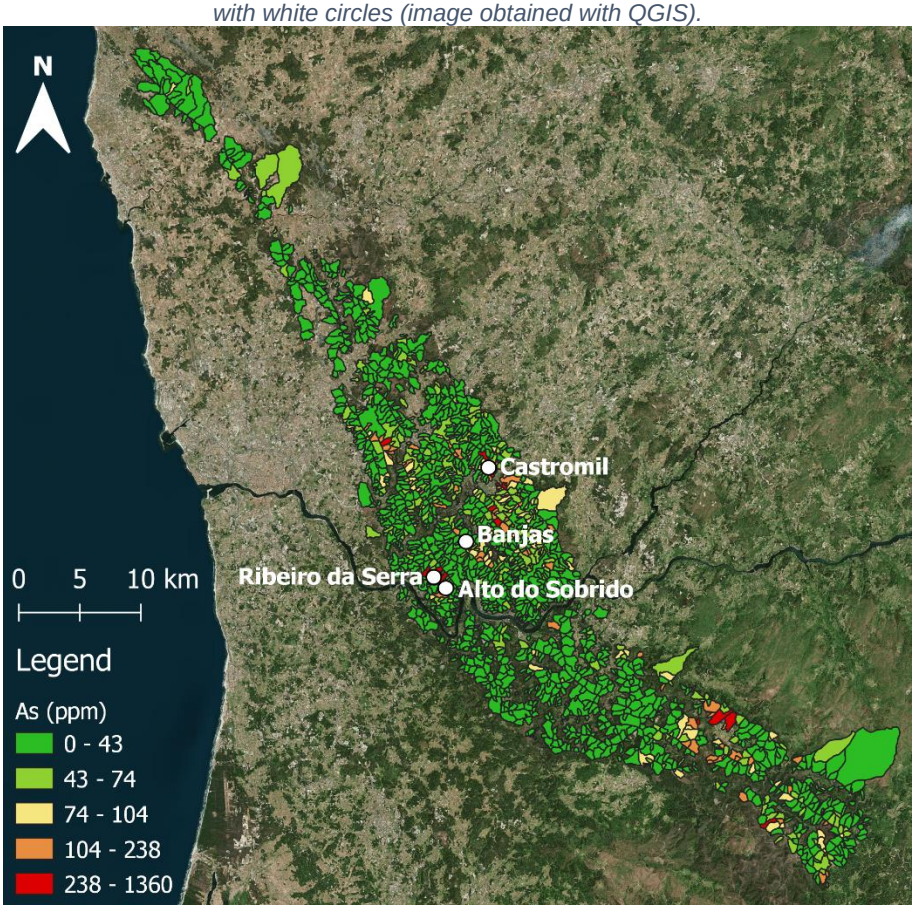

Figure 20 - Arsenic concentrations on the drainage basins, and the location of the higher concentrations marked with white circles (image obtained with QGIS).

Ribeiro da Igreja, Ribeiro da Serra and Alto do Sobrido correspond to a sector where the main association is Sb-Au (Couto, 1993), which is in accordance with the highest values found for these elements in those areas. Even though Couto (1993) says that the iron-arsenic stage is less important on the Ribeiro da Serra – Alto do Sobrido Sector, we can observe the highest arsenic values there.

For the Banjas and Castromil locations, these correspond to the Banjas Sector which has the main association of Au-As. This is also in accordance with the values found on these locations, even though the gold values in Castromil are not the highest.

For the concentrations of silver there are five locations of interest (Figure 21). The one with the highest concentration found (36,9 ppm) can be found in Terramonte, south of the Douro river. The second highest concentration (7,2 ppm) can be found in Gens, a locality of Foz do Sousa. The other three locations with high values correspond to Ribeiro da Igreja, Ribeiro da Serra and Alvarenga.

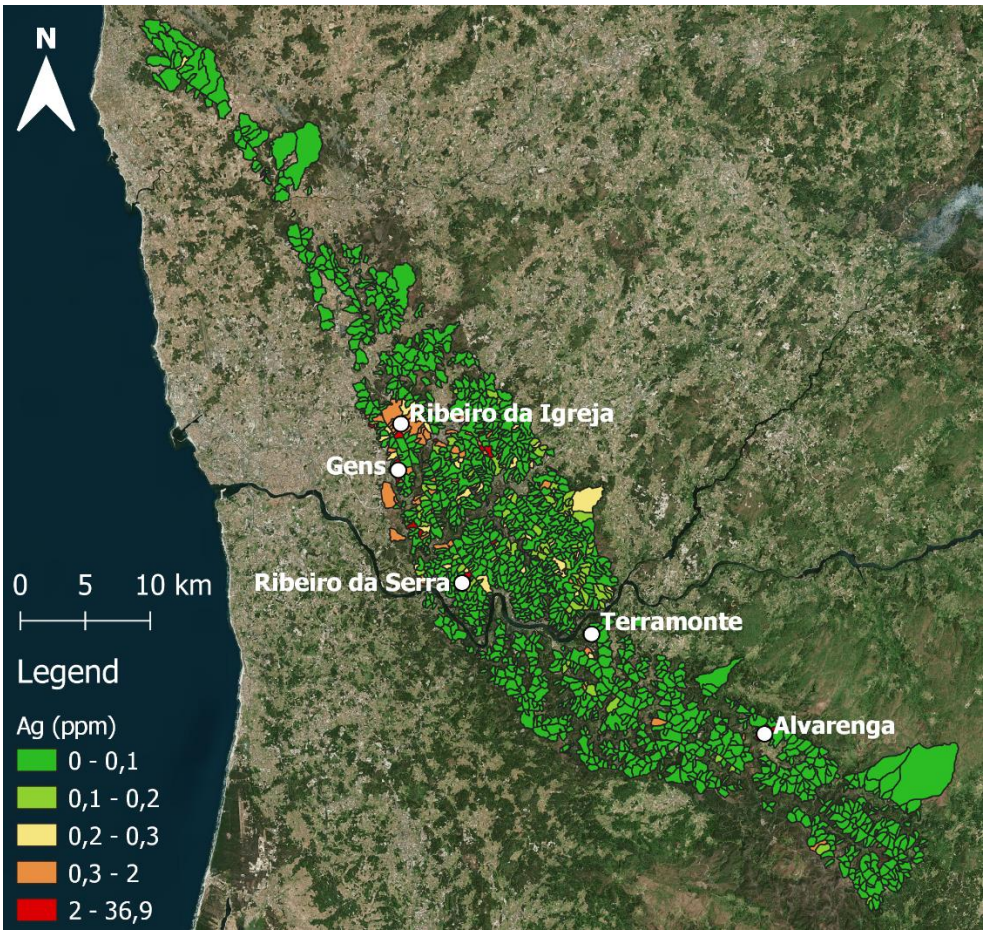

Figure 21 - Silver concentrations on the drainage basins, and the location of the higher concentrations marked with white circles (image obtained with QGIS).

Regarding the Pb concentrations, the higher values can be found in Ribeiro da Igreja, Ribeiro da Serra, Castromil, Terramonte and Alvarenga (Figure 22).

As for zinc concentrations, the higher values are observed in Ribeiro da Igreja and Terramonte (Figure 23).

For Ag, Pb and Zn, the highest values of 36,9 ppm, 4600 ppm and 3959 ppm, respectively, are in Terramonte. This corresponds to the Terramonte sector, that is known for its Pb-Zn(-Ag) association (Couto, 1993).

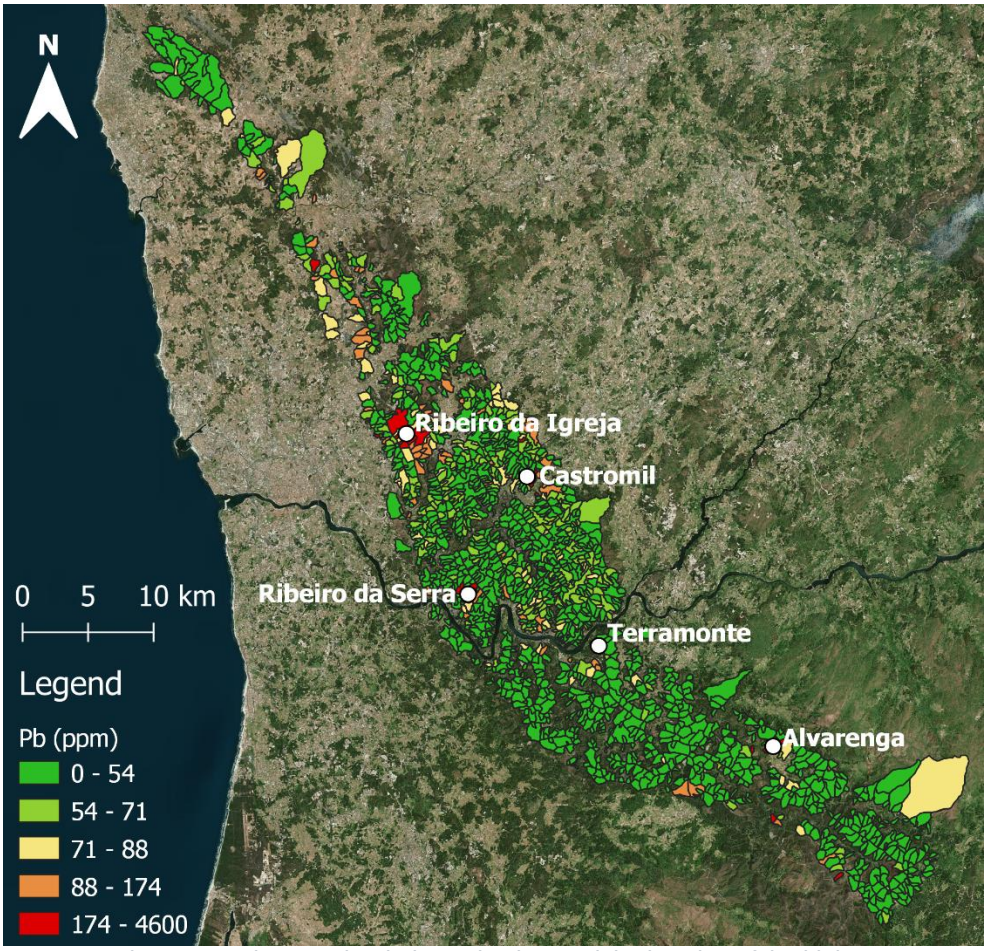

Figure 22 - Lead concentrations on the drainage basins, and the location of the higher concentrations marked with white circles (image obtained with QGIS).

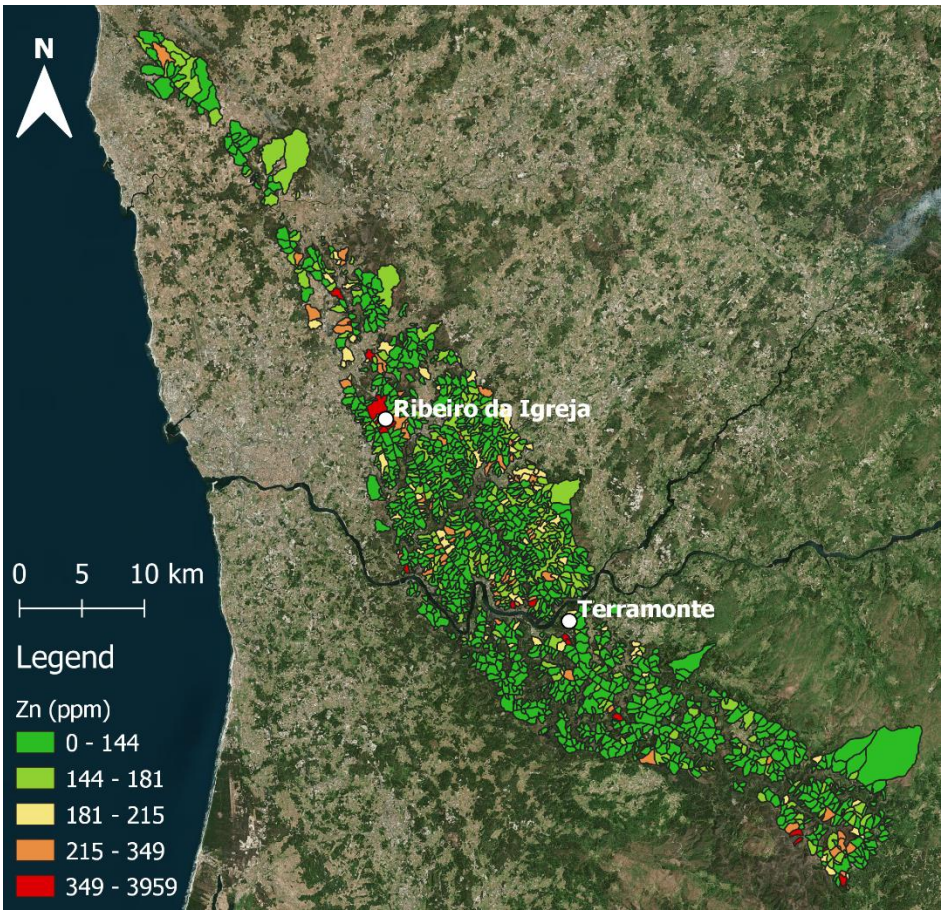

Figure 23 - Zinc concentrations on the drainage basins, and the location of the higher concentrations marked with white circles (image obtained with QGIS).

For both Sn and W, the highest concentrations can be found in Alvarenga and in Covas do Rio, but tungsten also as some high values in Ribeiro da Serra (Figures 24 and 25). In general, these higher values are close to a magmatic source. In the case of Alvarenga it is next to the Alvarenga Granite. As for Covas do Rio, it is close to the porphyritic granites of the area. Here there are also some diabase veins mapped on the Geological Map of Portugal 14-C (scale 1:50.000).

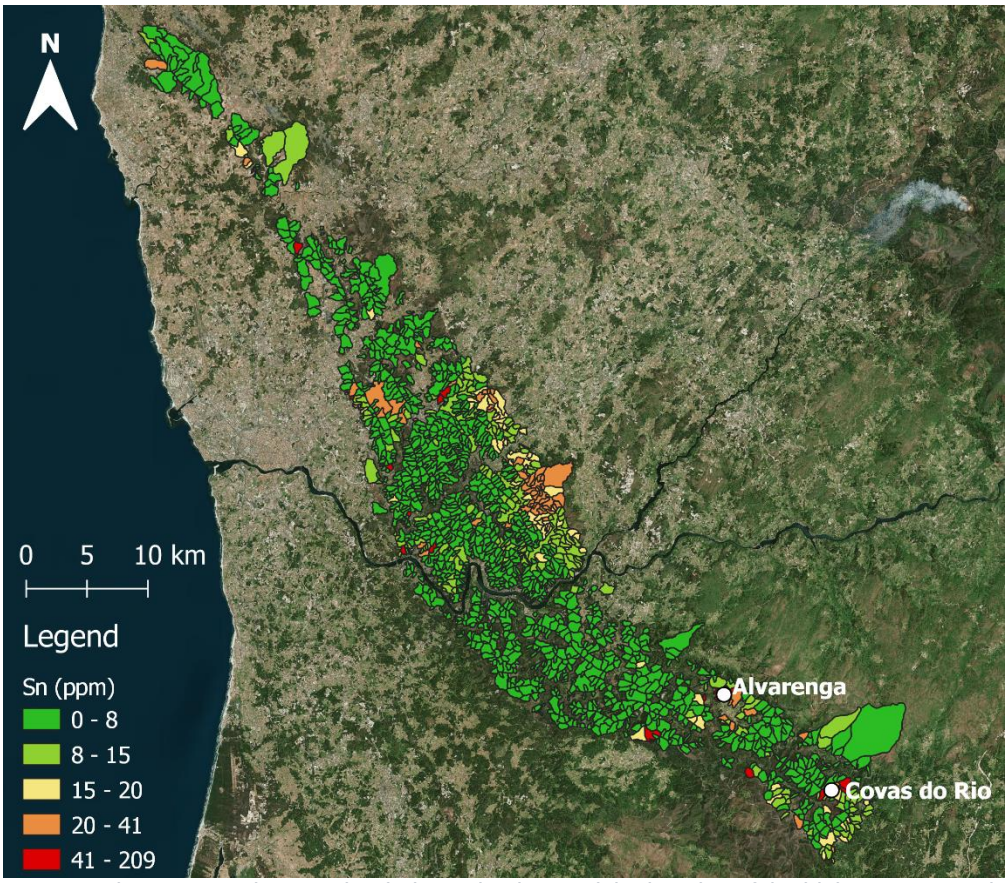

Figure 24 - Tin concentrations on the drainage basins, and the location of the higher concentrations marked with white circles (image obtained with QGIS).

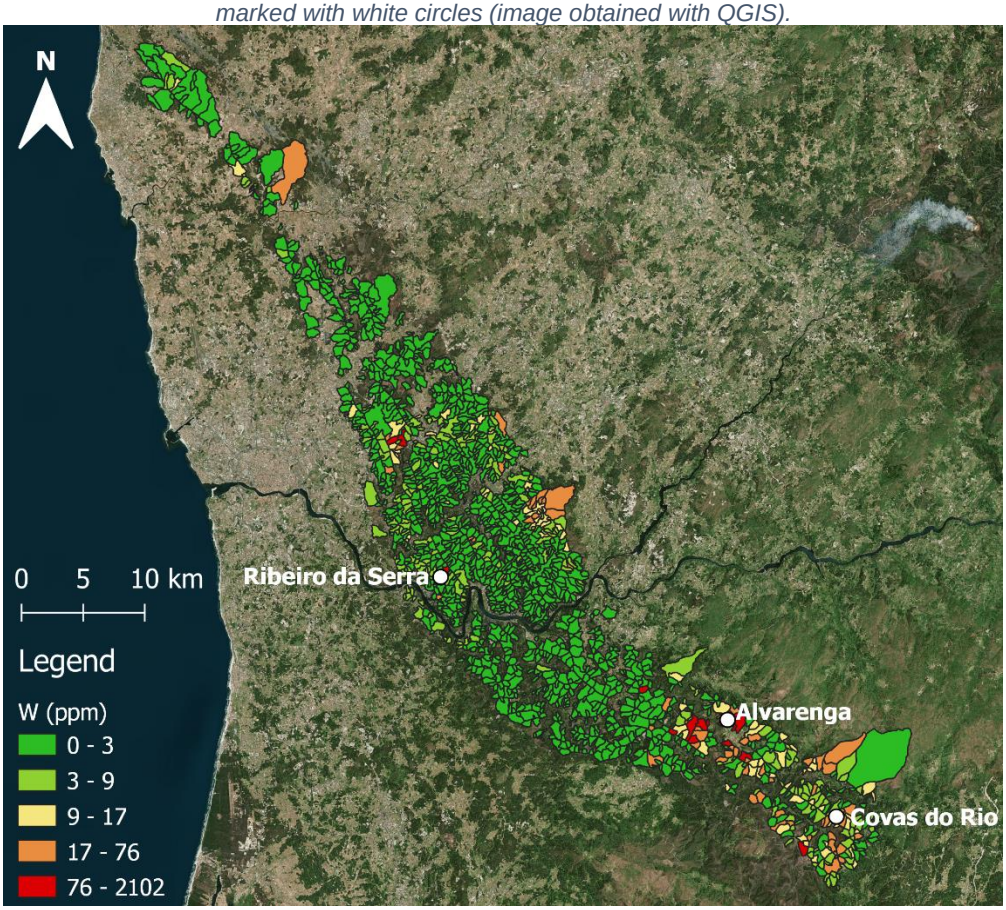

Figure 25 - Tungsten concentrations on the drainage basins, and the location of the higher concentrations marked with white circles (image obtained with QGIS).

5. Gravity Survey

5.1 Method

The gravity method consists in measuring the variations of the Earth's gravity, due to the differences in density of the subsurface rocks.

This surveying method has its basis in Newton's Law of Gravitation, that says that the force of attraction between two masses m1 and m2, whose dimensions are small when compared to the distance between them, is given by:

$$F = \frac{Gm_1m_2}{r^2}$$

Where G is the gravitational constant equal to $6{,}6726 \times 10^{-11}\ m^3kg^{-1}s^{-2}$.

If you consider a spherical and homogenous Earth, with no rotation, with mass M and radius R, with a small mass m on its surface, you can substitute the previous equation and obtain:

$$F = \frac{GM}{R^2}m = mg$$

With this you can see that force, F, is related to mass, m, by g, also known as the gravitational acceleration or gravity.

In an Earth like the one we were considering, gravity would be constant, but the Earth is not spherical or homogenous and it has a rotation, which causes gravity to vary across its surface. For a body with unit mass ($m = 1kg$) the average gravity at sea level is approximately equal to $9{,}81\ m/s^2$ (Kearey *et al*., 2002; Dentith & Mudge, 2014).

The changes that occur in gravitational acceleration due to density changes are very small when compared to the average strength of the Earth's gravitational field. The SI units for acceleration are meters per second square (m/s^2), while the cgs system uses the gal ($1\ gal = 1\ cm/s^2$). These units are too large to be used in gravity surveying, thus the cgs system defined a specific unit known as the milligal ($mGal$), where $1mGal = 10^{-3}\ Gal = 10^{-5}\ m/s^2$. Another alternative is the gravity unit (gu), that corresponds to $1\ gu = 1\ \mu m/s^2 = 10^{-6}\ m/s^2 = 0{,}1\ mGal$.

Gravity anomalies occur when there is a density contrast between a certain body and its surroundings. A gravity anomaly (Figure 26), can be either positive or negative, i.e., if the body is denser than its surroundings, the anomaly is positive, but if it is less dense than its surroundings it will produce a negative anomaly. Table 6 shows a few density ranges of the most common rocks.

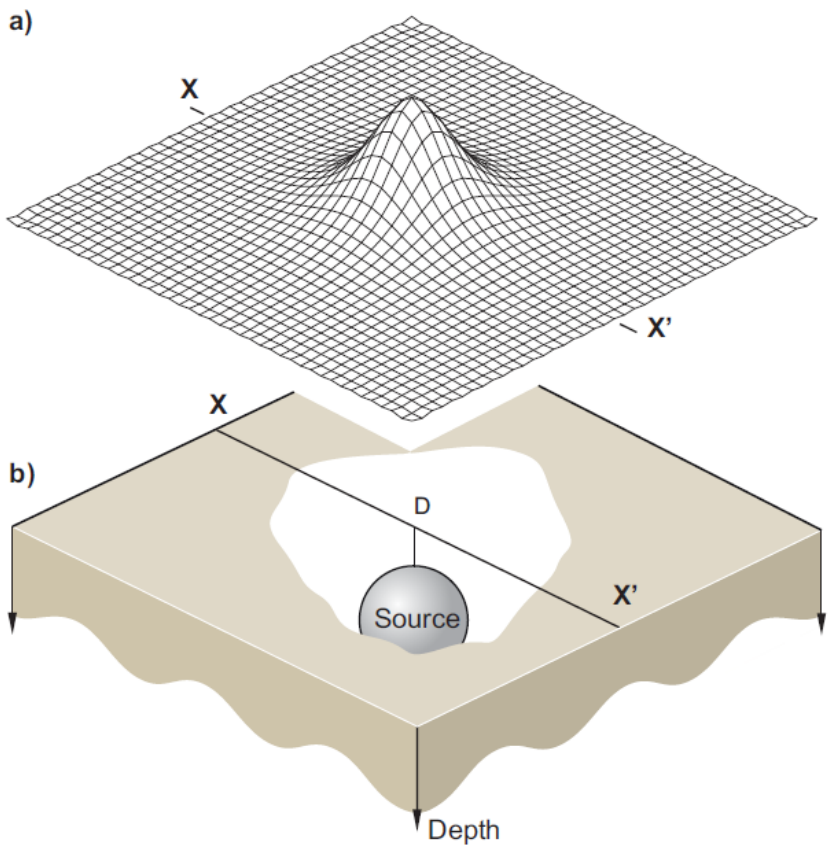

Figure 26 - Example of a positive gravity anomaly (a) from a spherical source on a horizontal surface (b) (Source: Dentith & Mudge, 2014).

Table 6 - Density ranges (in Mg/m^3) for some of the most common rocks (Kearey et al., 2002).

Clays	1,63 - 2,60
Shale	2,06 - 2,66
Sandstone	2,05 - 2,55
Limestone	2,60 - 2,80
Granite	2,52 - 2,75
Granodiorite	2,67 - 2,79
Basalt	2,70 - 3,20
Gabbro	2,85 - 3,12
Gneiss	2,61 - 2,99
Quartzite	2,60 - 2,70
Pyrrhotite	4,50 - 4,80
Magnetite	4,90 - 5,20
Pyrite	4,90 - 5,20
Cassiterite	6,80 - 7,10
Galena	7,40 - 7,60

The instruments used for gravity surveying are called gravity meters or gravimeters, and they measure the differences between the survey stations as well as the reference base station. Thus, the measurements made are relative, and not of the absolute value of gravity. There is no need to measure the absolute gravity because the objective is to observe the relative variations in gravity, caused by the changes in subsurface density.

Gravimeters operate on the general principle of measuring changes in the tension of a spring that has a small mass suspended. This mass is attached to a beam that is pivoted on its other end. Due to changes in temperature and the elastic properties of the spring and the beam, there are some changes in the meter readings. This is called instrumental drift. Although this was a problem for older instruments, modern gravimeters that operate under electronic control have very little drift. Instrumental drift can be monitored by making repeated readings at a reference location (base station) throughout the day (Dentith & Mudge, 2014).

When making a gravity measurement is it necessary to level the instrument, due to gravity being measured in the vertical direction. Modern instruments, that are electronically controlled, only require the operator to approximately level, after which they level themselves automatically.

There are several corrections that need to be done to the gravity measurements, due to the Earth's rotation, tidal effects, instrumental drift and topography. The process of doing these corrections is called gravity reduction and will be described in the following paragraphs.

Tidal Effects Correction

Due to the attraction of the Moon and the Sun, Earth's gravity varies with time. Although the Sun has a lot more mass than the Moon, the latter's proximity to Earth means it has a higher influence on Earth's gravity. The attraction between these bodies and the Earth, causes distortions on the Earth's shape, which leads to changes on its radius. This means that the distance and mass between an observation point and the Earth's centre of mass also changes. This is known as the tidal effects. They produce gravitational deviations of less than 0,3 mGal and vary with time and latitude.

Using the Longman (1959 *in* Dentith & Mudge, 2014) method it is possible to calculate the tidal effect for any time and any location. Modern gravimeters, such as the case of the Scintrex CG-5 used in this survey, automatically calculate and apply the tidal corrections to the measurements.

Instrumental Drift Correction

The drift correction compensates for the drift of the instrument's measurements over time. This correction is based on doing repeated readings on the base station, with recorded times throughout the day. These readings are plotted versus time, and it is assumed that the drift between consecutive readings is linear. In Figure 27 is an example

of a drift correction plot, where **d** is the correction that needs to be subtracted to the reading taken at time **t**.

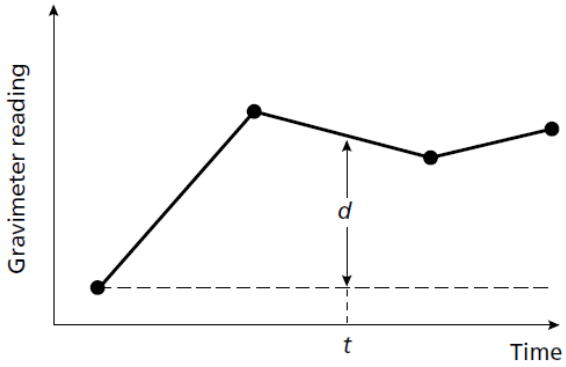

Figure 27 - Example of a gravimeter drift plot (reading versus time), made from the repeated readings at a fixed location (base station), where d is the value to subtract to the reading made at time t. (Source: Kearey et al., 2002).

Latitude Correction

Gravity values differ with latitude, due to the shape of the Earth being a pole flattened ellipsoid and due to its angular velocity decreasing from a maximum at the equator to zero at the poles (Figure 28). The centripetal force caused by the rotation of the Earth, causes gravity to decrease from the poles to the equator. Because the Earth is flattened at the poles, meaning they are closer to its centre of mass than the equator, this makes gravity increase from the equator to the poles. The amplitude of this effect is reduced due to the mass underlying the equator being greater than the one underlying the poles. With all these effects summed up, the gravity at the poles surpasses the gravity at the equator by approximately 5 186 mGal.

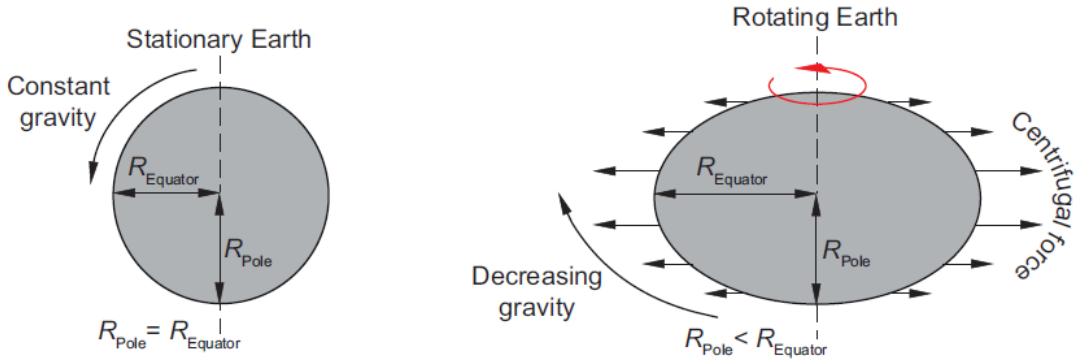

Figure 28 - Difference in Earth's gravity, if it was stationary and with its rotation (Source: Dentith & Mudge, 2014).

The variation of gravity with latitude, also known as normal gravity, is defined as the gravity on the surface of the reference spheroid (or reference ellipsoid), which is the idealised geometric figure, to where all geographical locations are referenced, in terms of their geographic coordinates, latitude and longitude.

The latitude correction is given by the International Gravity Formula for corrections where the absolute gravity is used, which is periodically updated. The International Gravity Formula of 1967, in mGal, is the following:

$$g_{norm} = 978\,031{,}85 + 5\,162{,}927\ sin^2\phi + 22{,}95\ sin^4\phi$$

Where g_{norm} corresponds to the normal gravity at a latitude ϕ, and the sea-level gravity at the equator is $978031{,}85$ mGal. This formula replaced the 1930 version, with slightly different constants.

A more recent formula appeared with the Geodetic Reference System (GRS80 spheroid), whose spheroid is similar to the World Geodetic System of 1984 (WGS84 spheroid). This is the Gravity Formula 1980 given by Moritz (1980 in Dentith & Mudge, 2014; Milsom & Eriksen, 2011):

$$g_{norm} = \frac{978\,032{,}677\,15\ (1 + 0{,}001\,931\,851\,353\ sin^2\phi)}{\sqrt{(1 - 0{,}006\,694\,380\,022\,9\ sin^2\phi)}}$$

In this case the gravity at the equator is $978\,032{,}677\,15$ mGal.

For this work the formula that is used is the one adjusted to the WGS84 ellipsoid, that is (Defense Mapping Agency, 1987):

$$g_{norm} = \frac{978\,032{,}677\,14\ (1 + 0{,}001\,931\,851\,386\,39\ sin^2\phi}{\sqrt{(1 - 0{,}006\,694\,379\,990\,13\ sin^2\ \phi}}$$

When these gravity formulas are used, the correction is made by subtracting the normal gravity to the absolute gravity.

For the cases where the absolute gravity is not used, the correction is made with the latitudinal gradient of normal gravity, which represents the change in gravity with north-south distance from the base station. This gradient is given by:

$$g_{\phi(N-S)} = 0{,}00812\sin(2\phi)\ gu/m = 0{,}812\ \sin(2\phi)\ mGal/km$$

Where the latitude (ϕ) is positive in the northern hemisphere and negative in the southern. The gradient is subtracted for stations located on the pole side of the base station and added for stations on the equatorial side.

Free-air Correction

The free-air correction (Figure 29(a)) corrects the decrease in the gravity due to the height in free air, that results from an increased distance to the centre of the Earth. To

reduce the measurements to the reference spheroid from their height h (in meters), it is necessary to add (if above sea-level) the free-air correction (FAC), calculated with:

$$FAC = 0{,}3086h\ mGal$$

Bouguer Correction

Because topographic masses are irregularly distributed, their effects on gravity are difficult to predict, so it is necessary to do an approximation. This approximation assumes that topography can be represented by the Bouguer plate, which consists in a flat plate with constant density and thickness equal to the height of the gravity station above the reference spheroid. The Bouguer effect on gravity is positive when above sea-level, so the Bouguer Correction (BC) (Figure 29(b)) needs to be subtracted:

$$BC = 0{,}04191\rho h\ mGal$$

With density (ρ) in Mg/m^3 and height (h) in meters. If the measurements are made on sea surface, then the Bouguer correction needs to be added, to account for the lack of rocks between surface and seabed. When using the average density of 2,67 Mg/m^3, the Bouguer Correction is equal to 0,1119 mGal/m.

Terrain Correction

To account for the topography relief around the gravity station it is necessary to do the terrain correction. When observing Figure 29(c), the areas marked with A were part of the Bouguer correction, even though there is no rock there. The Bouguer correction overcorrected in these areas, so they need to be restored by a positive correction. In the area marked with B, there are rocks that were not accounted for in the Bouguer correction, and that exert an upward pull, which causes gravity to decrease. So, again, the terrain correction needs to be positive.

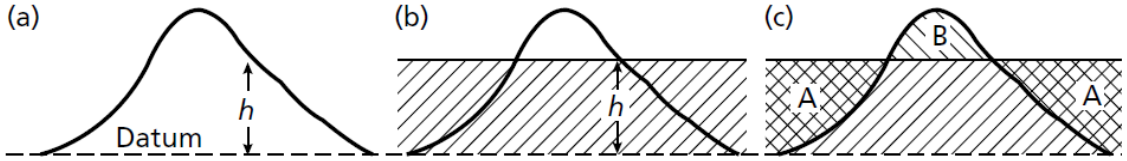

Figure 29 - (a) Free-air correction for an observation done at height h above the reference spheroid (datum); (b) Bouguer Correction, with a Bouguer plate of thickness h extending to infinity in both horizontal directions; (c) Terrain corrections for the areas A and B (Source: Kearey et al., 2002).

To apply the terrain correction, a chart divided by radial and concentric lines into several compartments, also known as the Hammer chart (Figure 30), is used.

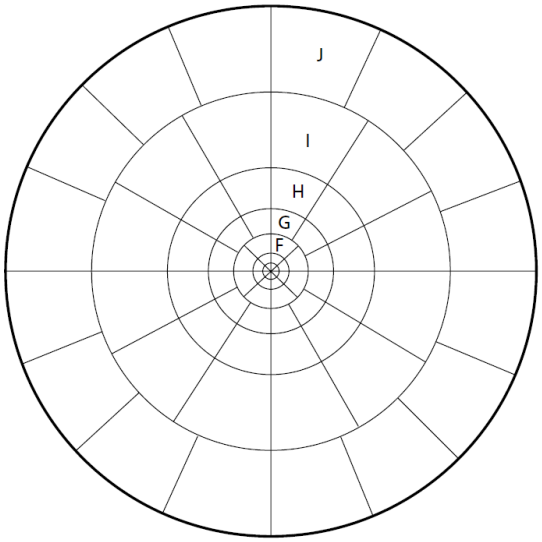

Figure 30 - Hammer chart used in terrain corrections (Source: Kearey et al., 2002).

This chart is placed on top of a topographic map with its centre on the gravity station and the average elevation of each compartment is determined. Then the elevation of the gravity station is subtracted from these values. Afterwards, the following formula is used in order to make the corrections for each sector (Kearey *et al*., 2002):

$$TC = 0{,}04191\frac{\rho}{n}\left(r_2 - r_1 + \sqrt{{r_1}^2 + z^2} - \sqrt{{r_2}^2 + z^2}\right)\ mGal$$

Where TC is the terrain correction for each compartment, ρ is the density used in the Bouguer correction, n is the number of compartments in each zone, r_1 and r_2 are the inner and outer radius for the zone in meters, respectively, and z is the modulus of elevation difference between the observation point and the mean elevation in the compartment in meters. The values of r_1, r_2 and n for each zone can be found on Table 7. Finally, the terrain correction is computed by summing the gravitational contribution of all compartments.

Table 7 - Values of r_1, r_2 and n for each zone of the Hammer chart (Source: Kearey et al., 2002).

Zone	r_1	r_2	n
B	2,0	16,6	4
C	16,6	53,3	6
D	53,3	170,1	6
E	170,1	390,1	8
F	390,1	894,8	8
G	894,8	1529,4	12
H	1529,4	2614,4	12
I	2614,4	4468,8	12
J	4468,8	6652,2	16
K	6652,2	9902,5	16
L	9902,5	14740,9	16
M	14740,9	21943,3	16

Free-air Anomaly and Bouguer Anomaly

Gravity data can be displayed in many forms. The free-air anomaly and the partial and complete Bouguer anomalies are the most common ways of presenting the data.

Firstly, perturbations to the gravity field, that are not of geological origin, are compensated and result in the observed gravity (g_{obs}):

$$g_{obs} = gravimeter\ reading + Tidal\ Correction + Drift\ Correction$$

The observed gravity can then be reduced to either the Free-air or the Bouguer anomalies. The Free-air Anomaly (FAA) consists in the observed gravity minus the latitude correction, summed to the free-air correction.

$$FAA = g_{obs} - g_{\phi} + FAC$$

The Bouguer Anomaly (BA) can be divided into two: the partial and the complete anomalies.

$$Partial\ BA = FAA - BC$$

$$Complete\ BA = FAA - BC + TC$$

The Bouguer anomaly consists in a broad and gently varying regional anomaly, on which local anomalies may superimpose. Usually, these local anomalies are the prime interest of gravity surveying, so from the Bouguer anomaly is removed the regional anomaly, in order to isolate the residual anomaly (Figure 31).

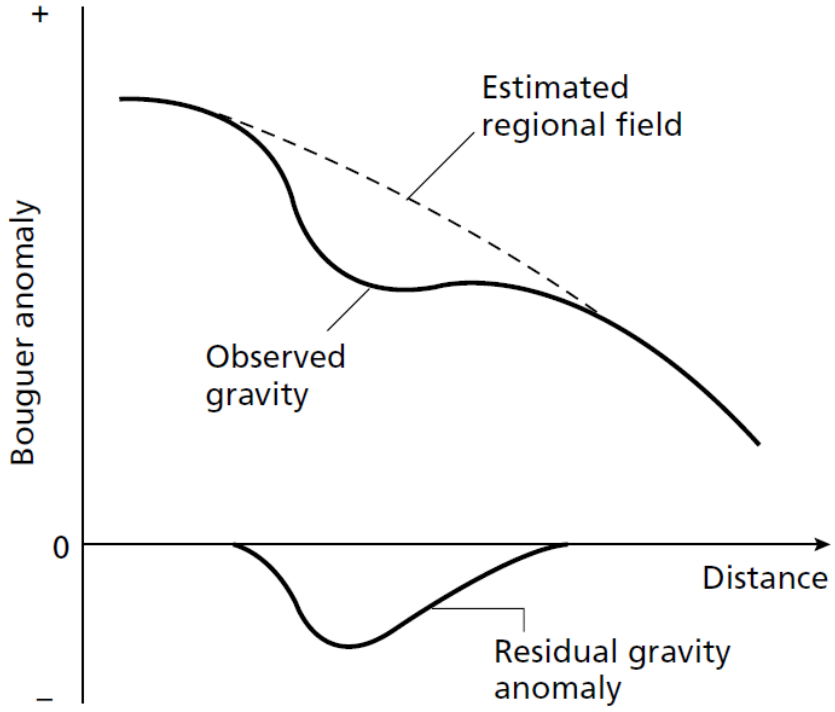

Figure 31 - The Bouguer anomaly's observed gravity, the regional anomaly and the residual anomaly (Source: Kearey et al., 2002).

Field Work

To perform a gravity survey, it is necessary to have at least one base station. In our case two bases were chosen, due to the fact that this survey was included in a larger survey made for the AUREOLE project. The first chosen base is located in the Geophysical Institute of the University of Porto, called base 9993 and the second one is located in Paredes, and is called base 9994 (Figure 32). In this figure can also be observed the 276 stations measured for the AUREOLE project. Since the absolute gravity value was known at the Institute it was only necessary to do relative gravity measurements between the two bases to determine the difference between them and define the absolute gravity value at Paredes.

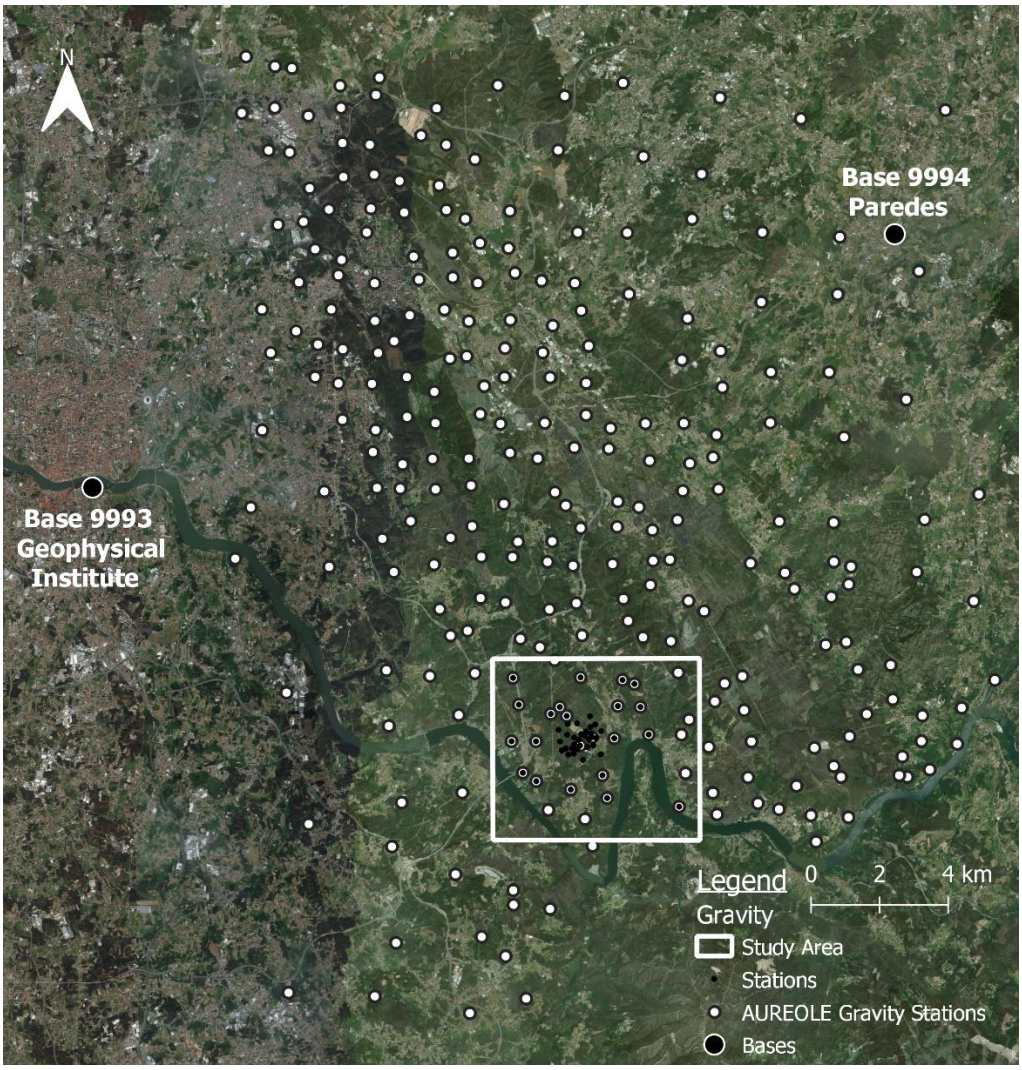

Figure 32 - Location of the Paredes (9994) and the Geophysical Institute (9993) bases, as well as the location of the survey area and gravimetric stations (image obtained with QGIS software).

Once the bases were defined, the survey could begin. Every day of field work started and ended with a reading at one of the bases, so that the instrumental drift could be corrected.

This sub-survey of the AUREOLE project is composed of 50 stations (Figure 33) that were gathered within the study area, with a higher density of points, where the Alto do Sobrido and Ribeiro da Serra mines are located, and a lower density in the surrounding areas. The location of the measurements had to be adapted to the available roads and to the existing type of terrain. For each reading the gravimeter was placed on the most stable type of ground possible, so that the levelling was not affected. Due to this, the spacing between points varies from 120 meters in the centre to around 1 km in the peripheral areas.

For every station, 3 readings of 100 seconds each were made, in order to decrease the error associated with the measurements. If a reading had a large error associated, then it was disregarded, and another reading was performed.

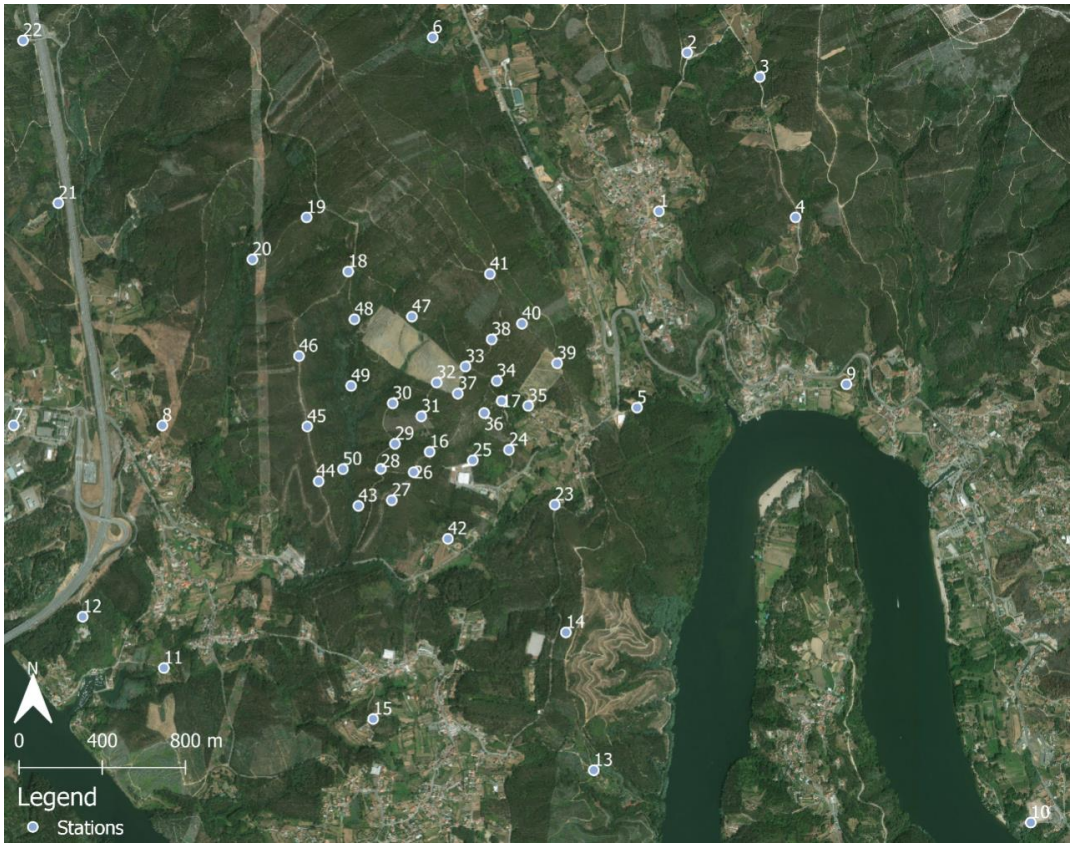

Figure 33 - Location of the stations of the gravimetric survey (image obtained using QGIS software).

The equipment used in this survey was the Scintex CG-5 Autograv (Figure 34). This is a microprocessor-based gravimeter, with a range of over 8000 mGal and a resolution of 0,001 mGal, which enables it to be used in either smaller and detailed surveys, such as the one in this thesis, or larger scale regional surveys. During the 100 second recording time the variations of the position of the mass are registered as an oscillating signal whose statistics are thus obtained in order to both define a reading as well as its quality. Using the GPS positioning the gravimeter automatically corrects for the Earth's tidal effects.

Figure 34 - Scintrex CG-5 Autograv gravimeter being levelled on the field to perform a reading.

For the rest of the corrections, it is necessary to have very precise longitude, latitude and elevation. So, for every gravimeter reading, the Stonex S850A differential GPS was used to make these measurements (Figure 35). The Stonex S850A has a horizontal precision of 2,5mm ± 1ppm, and a vertical precision of 5,0mm ±1ppm. The measurements carried out for this project had an average associated error of 0,016m horizontally and 0,032m vertically.

Figure 35 – On the left: differential GPS Stonex S850A in its case; On the right: Stonex S850A and gravimeter CG-5 Autograv being used on the field.

5.2 Results and Discussion

The gravity survey was done throughout the entire *geophysical methods'* study area (described in chapter 2.1), which contains the mines of Tapada, Ribeiro da Serra and Alto do Sobrido.

As was previously mentioned, in this survey 3 measurements of 100 seconds were done on 50 stations (Figure 33). An average value was determined for each station from those 3 readings.

The gravimeter's drift produced an increase in the relative values, which was corrected utilizing the readings at the beginning and end of each day at the bases.

Once the drift was corrected, the absolute gravity values for all stations were calculated, by using the absolute and relative values of the two base stations. The rest of the reduction of the gravity data (correction of latitude, free-air, bouguer and terrain) was applied to the obtained absolute values of the stations to finally acquire the survey area's Complete Bouguer Anomaly. Part of the terrain correction was done with field data and another was carried out using Geosoft's Oasis Montaj software (version 8.4), using a 20x20 meters DEM. All the following maps were also created on Oasis Montaj.

In the Complete Bouguer Anomaly (Figure 36) occurs a decrease in the values of gravity from South to North. This is also the case for the Regional Anomaly (Figure 37) that was obtained from the entire set of gravity data collected for the AUREOLE project.

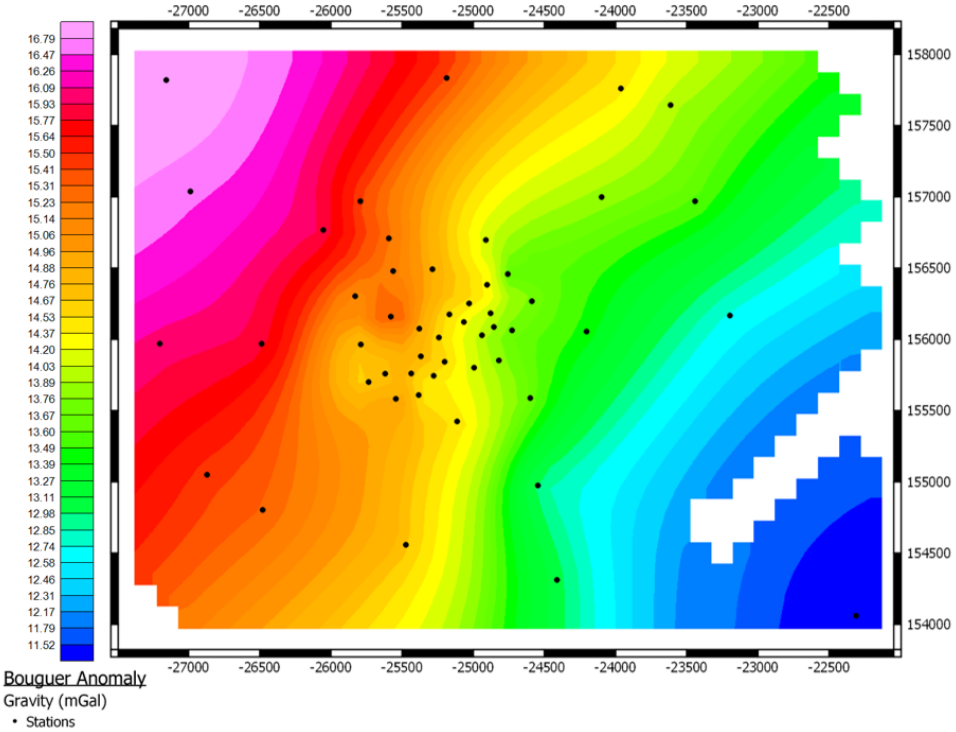

Figure 36 - Complete Bouguer anomaly acquired through the gravity survey. Small circles correspond to the 50 stations of the study area (coordinates: ETRS89 TM06) (map obtained with Oasis Montaj software).

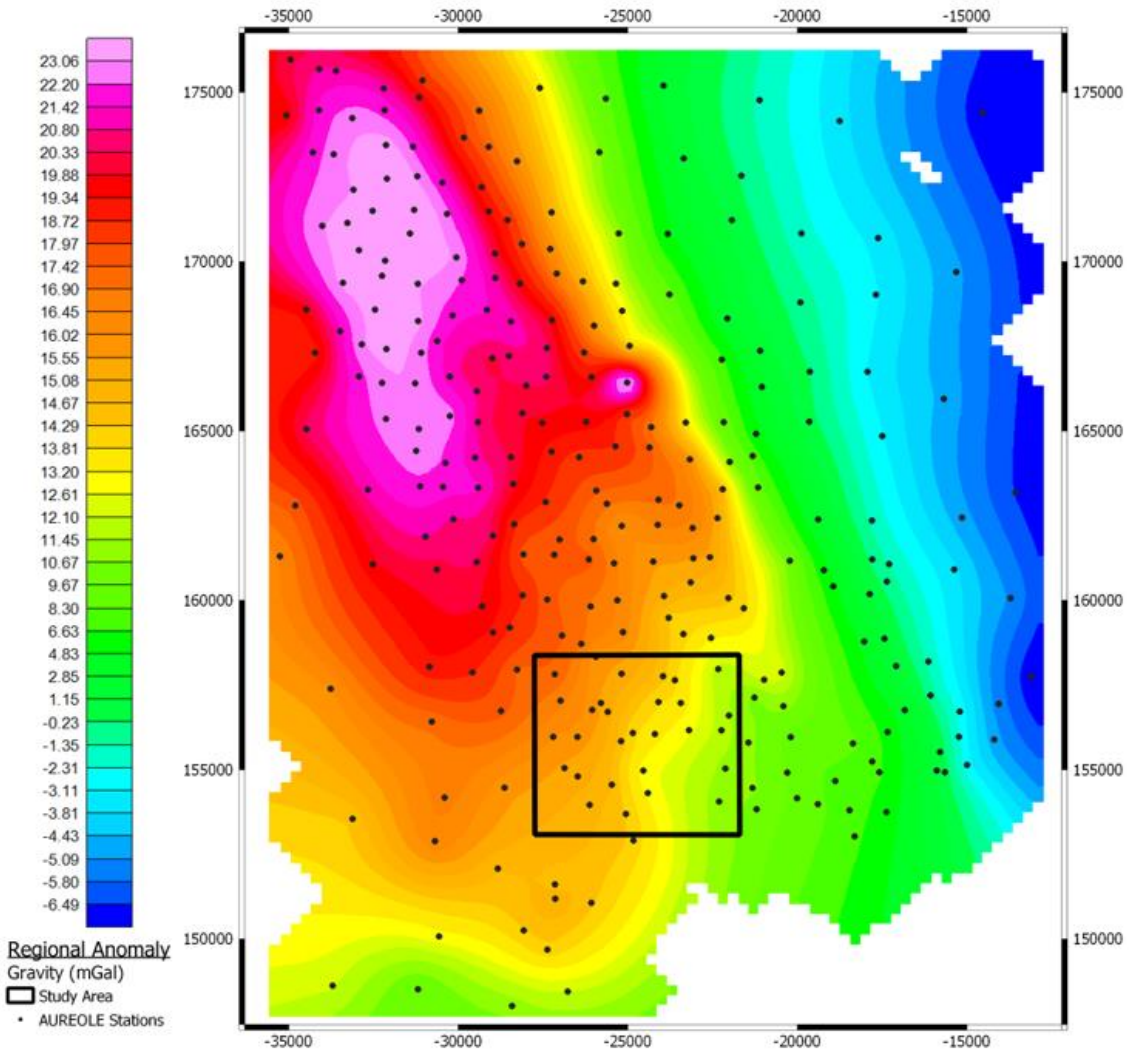

Figure 37 - Regional Anomaly obtained from the data collected on the larger survey of the AUREOLE project, with the study area marked with a black rectangle (Coordinates: ETRS89 TM06) (map created with Oasis Montaj software).

In order to visualize the actual anomalies of the study area it was required that the Regional Anomaly be subtracted from the Complete Bouguer Anomaly, which results in the Residual Anomaly of the area (Figure 38).

In Figure 38 it is also possible to observe the mapped lithologies from sheet 13-B of the Portuguese Geological Maps on top of the residual anomaly. The residual anomaly map is focused on the area where there is a higher density of stations, because the interpolation on the edges, where the stations are scarcer, is exaggerated.

Observing Figure 39 there is the residual anomaly with the location of the known veins that were mapped by Kernow Mining (2009) on their 5th report of activities, where they gathered information from older reports and added new information.

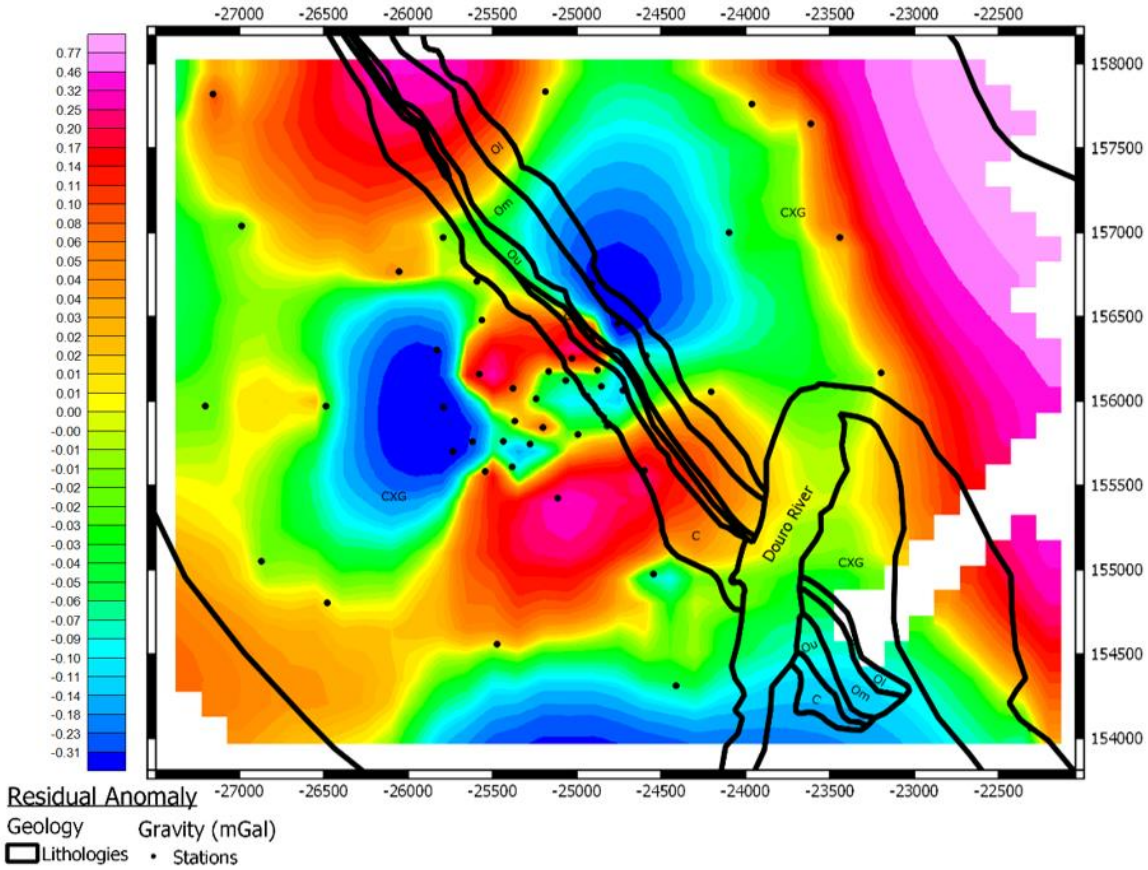

Figure 38 - Residual Anomaly with the location of the stations and mapped lithologies (C – Carboniferous; D – Devonian; Ou – Upper Ordovician; Om – Middle Ordovician; Ol – Lower Ordovician; CXG – Schist-Greywacke Complex).

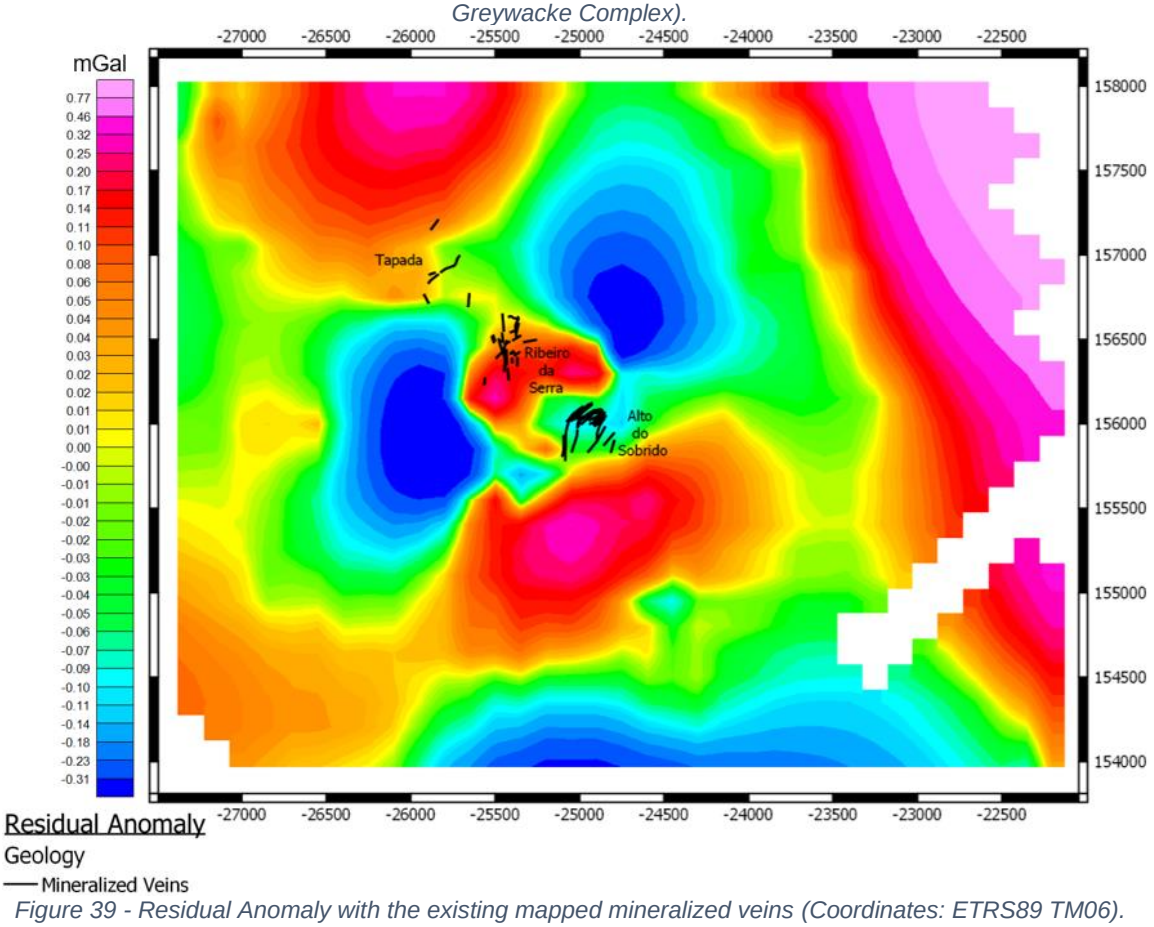

Figure 39 - Residual Anomaly with the existing mapped mineralized veins (Coordinates: ETRS89 TM06).

In the residual anomaly map, it is possible to observe zones of negative anomalies (lower densities) and zones of positive anomalies (higher densities).

According Gumiel (1983), regionally there is a spatial correlation between the Sb-Au mineralizations and the post-orogenic granites in the Dúrico-Beirã Region, and at a larger scale, a spatial correlation between the mineralizations and basic rock dikes can also be seen. Vallance et al. (2003) did a geochemical study about the Castromil gold deposit that supports the presence of a granite at depth. Couto et al., (2007) acquired data that suggest a genetic connection between the Sb-Au mineralizations and non-outcropping granites, and that these may have been a source of fluids, metals, and sulphur, while acting as a heat source, that improved hydrothermal circulation. These non-outcropping granites were reported to have been observed in one of the galleries of the Ribeiro da Serra mine (Couto et al., 1999; Couto, 2014).

With this it is possible to propose the hypothesis that these zones of lower density values could in fact correspond to a granitic source for the hydrothermal fluids that gave origin to the mineralized veins of Tapada, Ribeiro da Serra and Alto do Sobrido.

A 2D model was created from a section (Figure 40) with an orientation of SW-NE. Having this hypothesis as a starting point, the creation of the model used the mapped lithologies and a granite that was introduced where the negative anomalies occur.

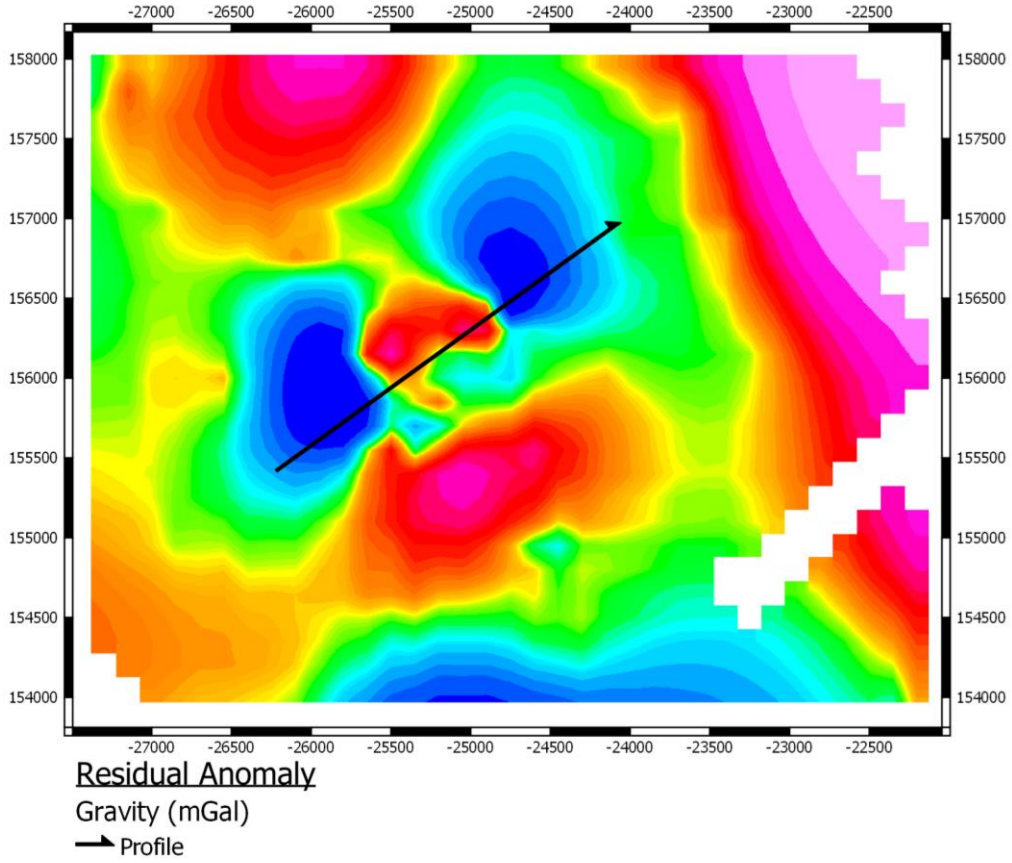

Figure 40 - Location of the section done for the creation of the 2D model (Coordinates: ETRS89 TM06).

Due to the fact of not being able to measure densities with confidence in our study area, through either direct methods or Nettleton or Parasnis methods, the densities used in this model are theoretical and are based on previous works related to this one, i.e., where the gravity method was used for areas with CXG and granites. Once the values were gathered from these works, a mean value was calculated and used in the modelling. The following table contains the values of densities for the different lithologies of each work, as well as the calculated mean (Table 8).

Table 8 - Values of density (g/cm^3) for CXG, granites and quartzites from previous works, and the mean values calculated from them.

	Machadinho (2014)	Ribeiro (2017)		Cruz (2020)				Mean
CXG	2,74	2,75	2,766	2,74				2,749
Granite	2,61	2,566	2,67	2,50	2,53	2,56	2,58	2,574
Quartzite	2,69	----------		----------				2,69

The obtained model can be seen on Figure 41. For the densities of the lithologies from the Middle Ordovician to the Carboniferous, since they are mainly schists, they started with the same density as the CXG, and then were slightly adjusted through inversion in order to fit the gravimetric anomaly.

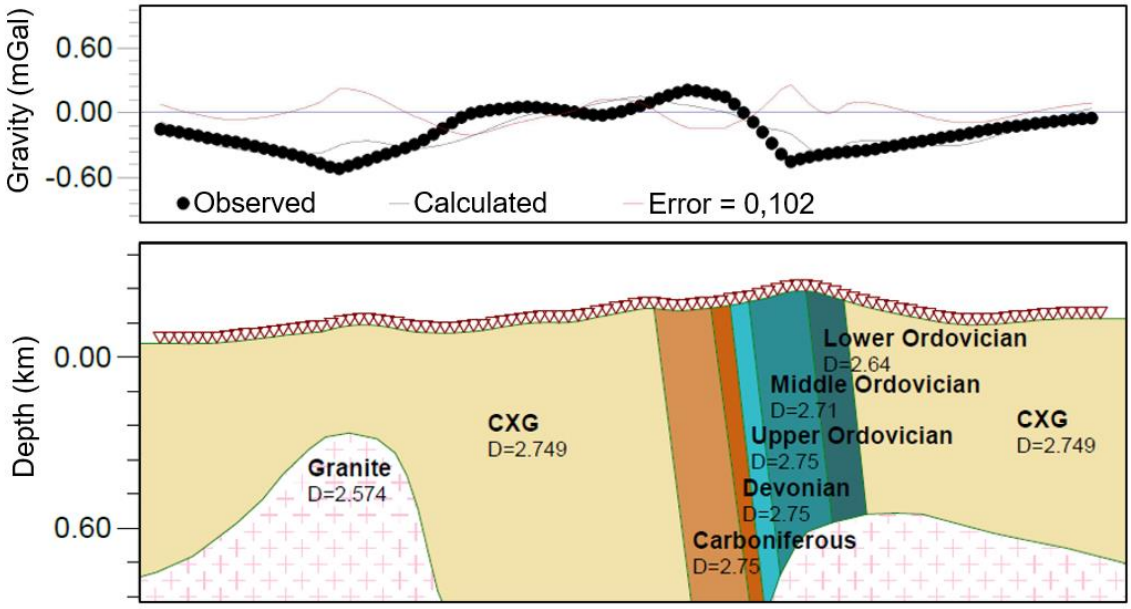

Figure 41 - 2D model created from the section of Figure 40, for the residual anomaly obtained through the gravity survey.

6. Electromagnetic Survey (VLF)

6.1 Method

Electromagnetic (EM) methods use electromagnetic fields to obtain a response from ground. The primary EM field is created by a transmitter that provides an electric current through a small coil or a large loop of wire. When a conducting body is present, this primary field induces alternating currents (or eddy currents) on the conductor, that generate a secondary EM field, which is then detected by a receiver coil, through the secondary field's induced eddy currents. The receiver responds to both the primary and secondary fields (Figure 42). The difference between the transmitted field and the received fields allows for a better understanding of the conductor body, in terms of its geometry and electrical properties (Kearey *et al*., 2002).

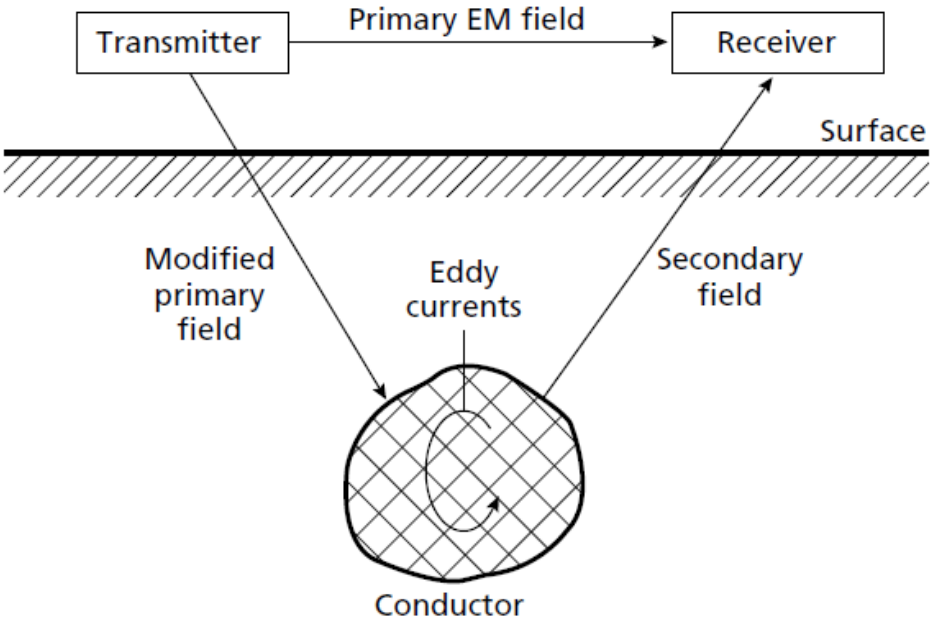

Figure 42 – The principle of electromagnetic methods (source: Kearey et al., 2002).

Very Low Frequency (VLF)

The VLF method utilizes low frequency waves, within the range of 15 to 30 kHz, that are transmitted continuously by approximately 42 stations around the world, as the primary field. These frequencies are used for long-range communication and for navigational systems, usually within the military (Kearey *et al*., 2002; Milsom, 2003). The signal from these stations is used in several applications, such as ground water detection, soil engineering, nuclear waste detection and mineral exploration (Sundararajan *et al*., 2006 *in* Zhang, 2015). This method is a sort of "passive" geophysical method and an inductive exploration technique, which is mainly used in the mapping of shallow subsurface structures where the primary EM waves induce eddy currents (Ajiboye, 2019).

The electromagnetic field is basically planar and horizontal at long distances from the source of the VLF waves. Therefore, the electric component of the field is in the vertical

plane and the magnetic component is perpendicular to the direction of propagation in the horizontal plane (Figure 43). The best targets for this method are tabular conductors in a resistive host rock (Kearey *et al*., 2002; Ajiboye, 2019).

When a conductor strikes towards the direction of propagation, the magnetic vector intersects it, and generates eddy currents, consequently producing a secondary field. However, when the conductor is perpendicular to the direction of propagation, the magnetic vector cannot intersect it effectively, thus it will not create a secondary electromagnetic field (Kearey *et al*., 2002). With the instruments used nowadays this is not a problem, because the instruments receive waves from three different frequencies. With this you can choose 3 different directions of propagation, so that the conductor is always intersected by the magnetic vector.

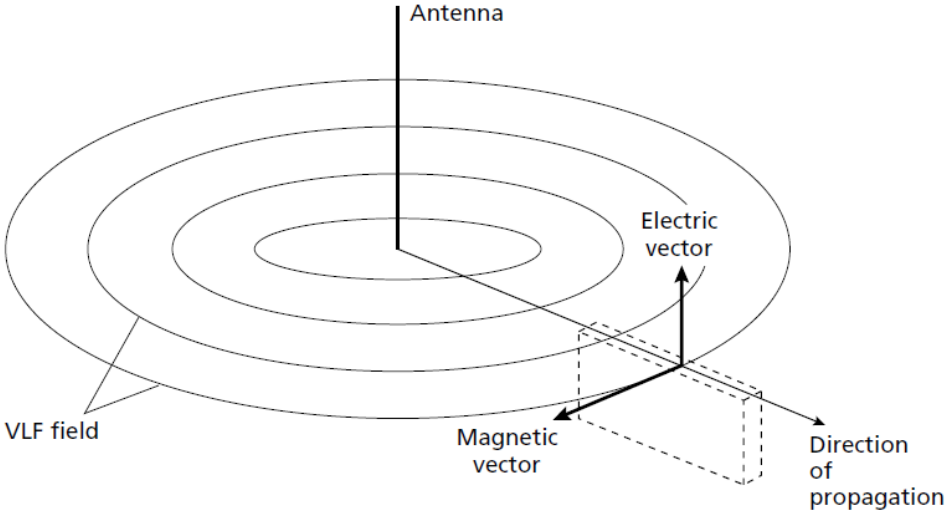

Figure 43 - VLF method's principle. In this case the conductor (dashed lines) strikes in the direction of propagation, being cut by the magnetic vector of the electromagnetic field. (Source: Kearey et al., 2002).

A VLF anomaly is represented by the change in the direction of the electromagnetic vector due to the conductive materials in the subsurface. The detection of these anomalies is possible due to VLF receivers recording the in phase and quadrature components of the vertical secondary field relative to the primary horizontal field (Ajiboye, 2019).

There are some factors that influence VLF readings, such as the topography and the presence of surface water. Irregular terrains can cause anomalies that cause the obtained readings to be different than the ones made on flat ground. Bodies of water, such as lakes or rivers, have high contrast in conductivity with the ground surrounding it, which can create anomalies in the measurements (Zhang, 2015; Ajiboye, 2019).

Field Work

The equipment used for the electromagnetic survey is the EDA OMNI PLUS VLF (Figure 44). This is a microprocessor-based magnetometer/VLF system that is capable of measuring changes or contrasts detected by the two geophysical methods. In this case the equipment was used solely with the VLF system and with a three-component sensor, that measures the magnetic component of the secondary VLF field, and probes attached through the VLF circuitry, that measure the electric component of the secondary field.

For the calibration of the OMNI PLUS it was necessary to make 150 readings, on frequencies ranging from 15,0 to 30,0 kHz, with intervals of 0,1 kHz. With these readings it was possible to understand which stations around the world had higher values of the electromagnetic field and which are consequently better for the VLF method in the study area. This resulted in three frequencies: 19,2 kHz from India; 22,1 kHz from the United Kingdom; 23,4 kHz from Germany. All of these come from different directions which will allow the survey to observe conductor bodies with almost every orientation. These directions are also the best fit for the profiles performed, and for the orientation of the known mineralizations (Figure 45).

Figure 44 – EDA's OMNI PLUS equipment used in the electromagnetic survey. On the top of the image is the console and down is the antenna with the three-component sensor.

The survey was made in 5 profiles with a spacing between stations of 5 meters. One measurement was made on each station, for a total of 283 stations (Figure 45). Two of the profiles were made in the same line with opposite directions and on different days to make sure the equipment was working properly. All the profiles were done around the location of the Alto do Sobrido mine, where most of the mineralizations occur.

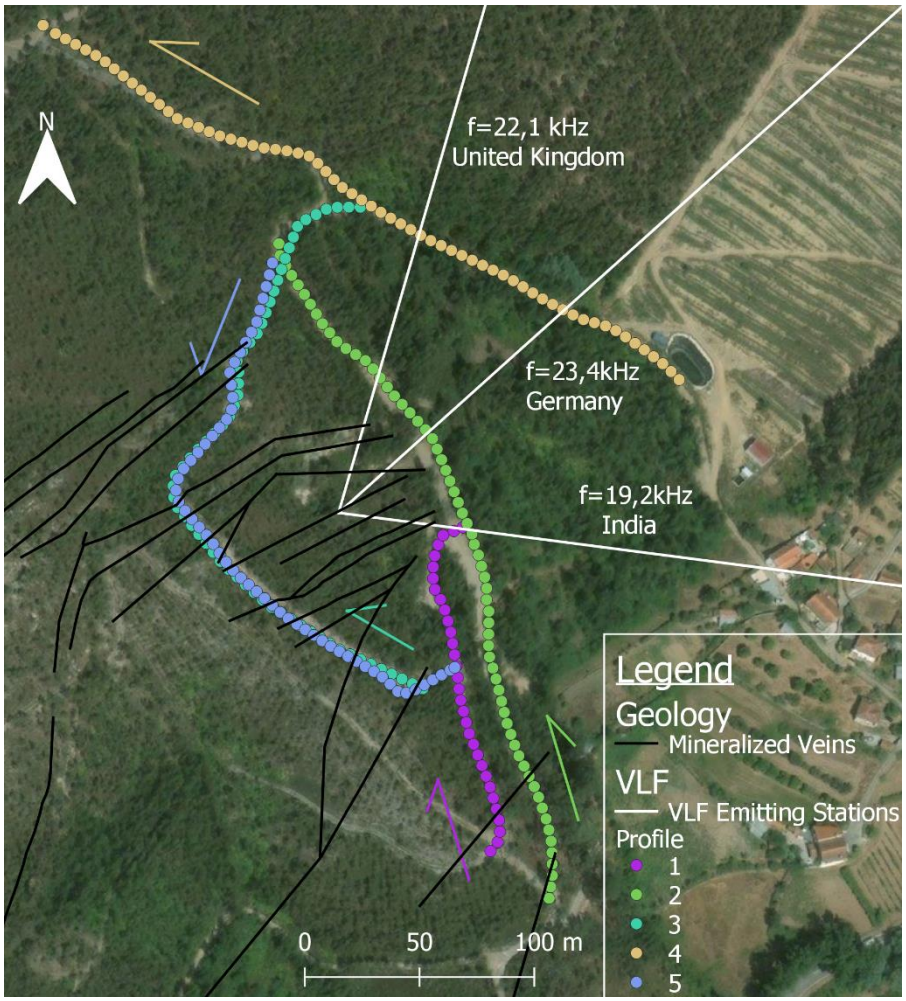

Figure 45 - Location of the VLF survey stations, coloured different for each profile with arrows pointing the direction of each profile, as well as the mineralized veins and the direction of each frequency (image acquired through QGIS).

6.2 Results and Discussion

The results of the electromagnetic (VLF) survey are obtained in 3 different sections of resistivity for each one of the profiles (Figure 45). These sections correspond to the three different frequencies that were used for the survey: 19,2 kHz, 22,1 kHz and 23,4 kHz.

Before each survey day, a test was performed on the equipment to ensure that it was working correctly, and that all the frequencies were being received properly. For profile 5, frequency 19,2 kHz did not have a good signal, so it will not be used in the interpretation of the data.

The sections that will be displayed in this chapter were acquired with the software EMTOMO VLF2Dmf. In this case the software used the values of in-phase and quadrature of each station (Table B in Appendix 2) to perform an inversion of the data and infer sections of resistivity of the ground. These sections go to around 160 meters of depth, but the first 40 meters are the most reliable.

The sections for each of the profiles can be found on the following Figures 46, 48, 50, 51 and 53 with sections A, B and C corresponding to frequencies 19,2 kHz, 22,1 kHz and 23,4 kHz, respectively.

Profile number 1 is the shortest and is composed of 32 stations. In the three sections of Figure 46 it is possible to observe an area of lower resistivity on the northern side of the profile. This area is near the contact between CXG and the Carboniferous and the mineralized veins (Figure 47). This contact is made by the Dúrico-Beirã Shear Zone (DBSZ), which makes the rocks in this area more weathered than its surroundings, which could explain the decrease in resistivity, but it could also be due to the presence of the mineralized veins.

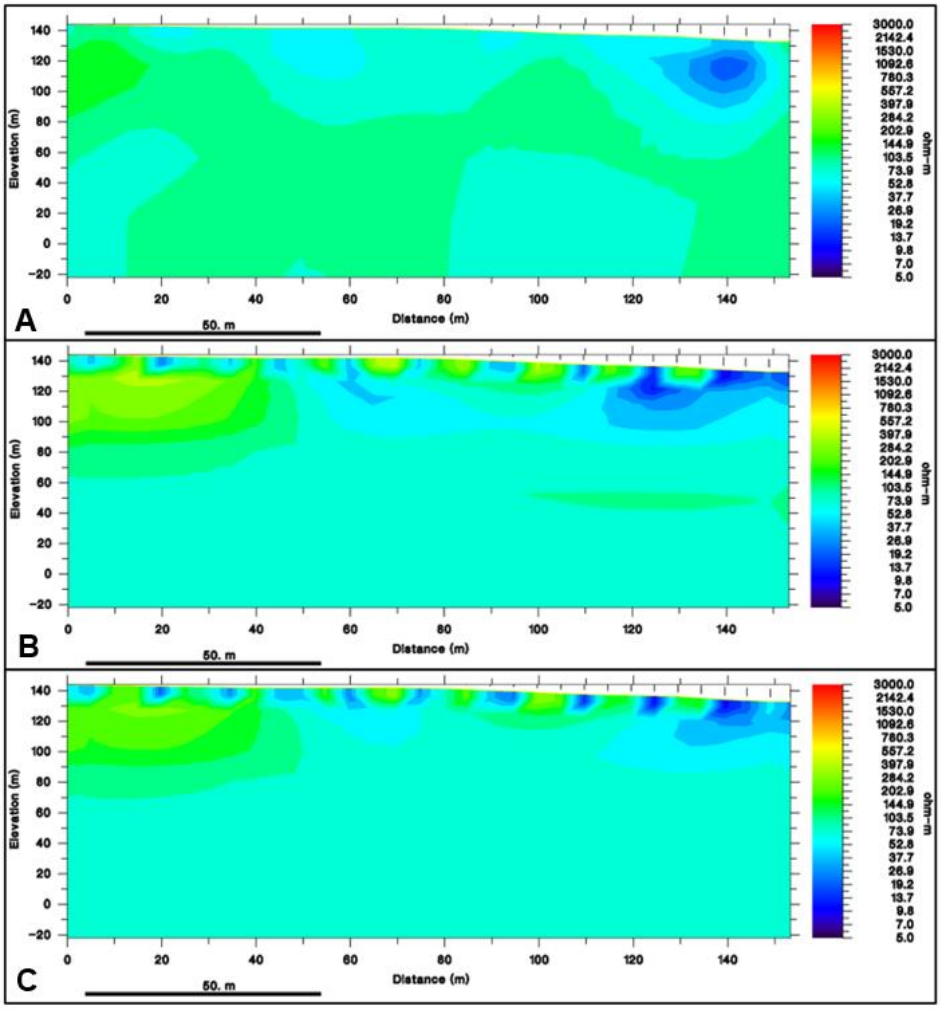

Figure 46 - Resistivity sections for the frequencies 19,2 kHz (A), 22,1 kHz (B) and 23,4 kHz (C) of profile 1 (sections obtained with VLF2Dmf software).

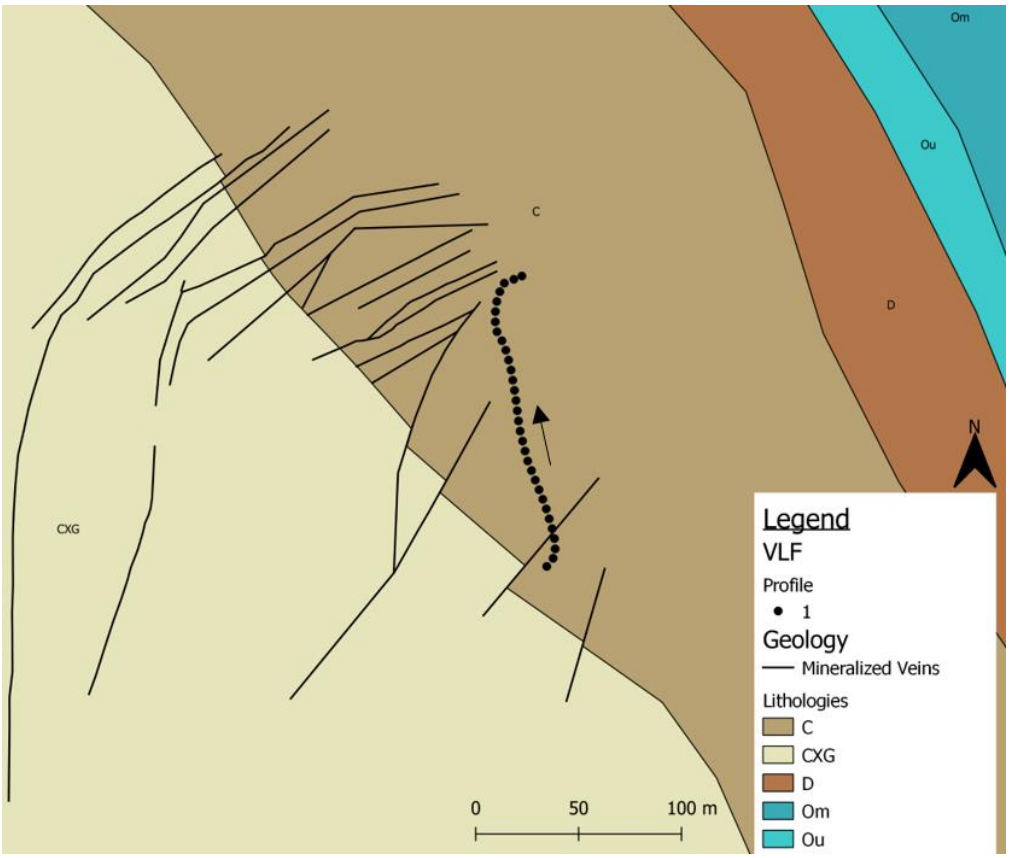

Figure 47 – Map of Alto do Sobrido with the location of profile 1 (direction marked with an arrow), the mineralized veins and the lithologies present (C – Carboniferous; D – Devonian; Ou – Upper Ordovician; Om – Middle Ordovician; CXG – Schist-Greywacke Complex).

The second profile is composed by 65 stations. In Figure 48 A, B and C can be seen the resistivity sections for each of the frequencies. In these sections, in the northern side of the profile, it is possible to see an increase in resistivity on the surface, but at around 20 meters of depth the resistivity drops. This difference is more noticeable on section B, where on the surface the value of resistivity is around 1000 Ohm·m and at 20 meters depth changes to approximately 5 Ohm·m. The location of this area of lower resistivity does not match the location of any known veins but could be due to either their elongation or related subsurface veins that are not yet mapped (Figure 49).

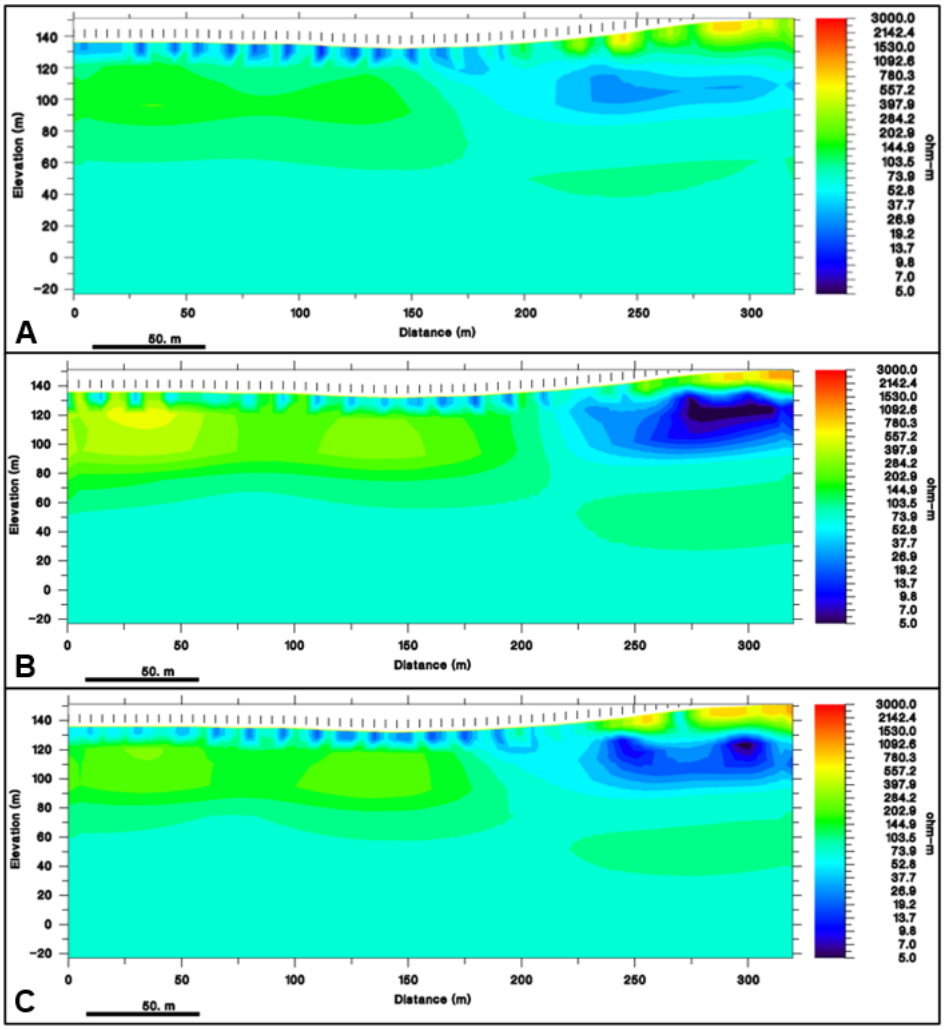

Figure 48 - Resistivity sections for the frequencies 19,2 kHz (A), 22,1 kHz (B) and 23,4 kHz (C) of profile 2 (sections obtained with VLF2Dmf software).

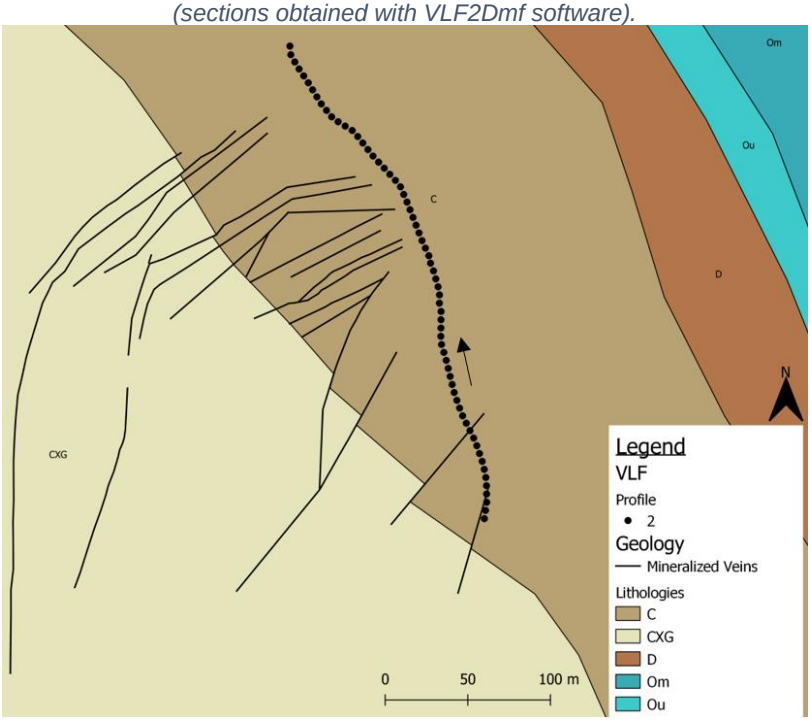

Figure 49 - Map of Alto do Sobrido with the location of profile 2 (direction marked with an arrow), the mineralized veins and the lithologies present (C – Carboniferous; D – Devonian; Ou – Upper Ordovician; Om – Middle Ordovician; CXG – Schist-Greywacke Complex).

In profile 3 there are 62 stations. The sections for this profile can be found in Figure 50. Here it is possible to see three areas of lower resistivity.

Profile 5 is located in the same path as profile 3, but the start and end stations do not coincide and are offset for approximately 50 meters. These two profiles were made in opposite directions.

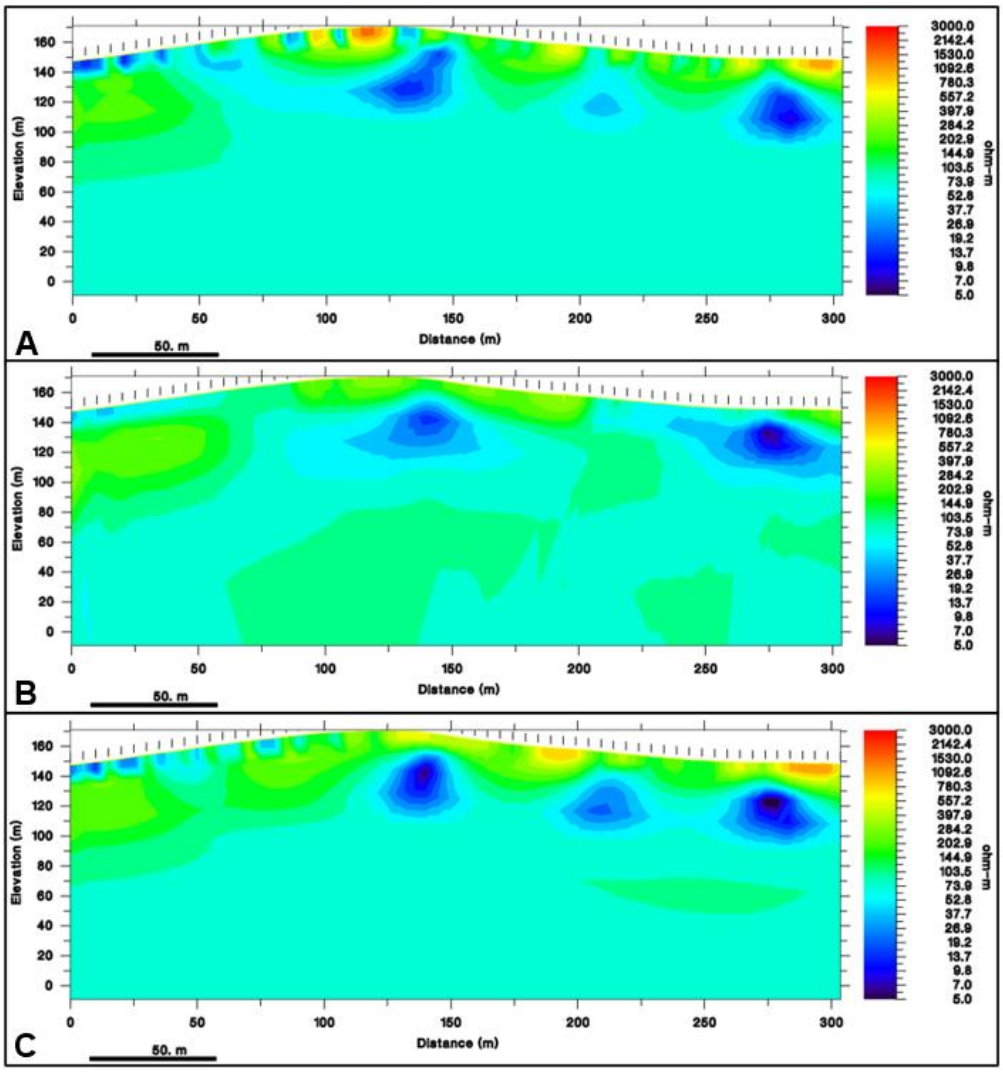

Figure 50 - Resistivity sections for the frequencies 19,2 kHz (A), 22,1 kHz (B) and 23,4 kHz (C) of profile 3 (sections obtained with VLF2Dmf software).

The 5th profile is composed of 59 stations, and it has areas of lower resistivity (Figure 51), that seem to correspond to the ones found on profile 3. These areas are likely due to the weathering and/or fracturing of the rocks that occur around the DBSZ that makes the contact between the CXG and the Carboniferous. These could also occur due to most of the mineralized veins occurring in these areas (Figure 52).

The lower resistivity area located at approximately 210 meters distance in profile 3 and 125 meters in profile 5, cannot be found on the 22,1 kHz sections. But appear on the

other sections, especially on the 23,4 kHz sections, which could indicate that this structure or weathering zone has an orientation close to NE-SW.

In profile 5 occurs an area of higher resistivity near the surface, that did not appear on the sections from profile 3.

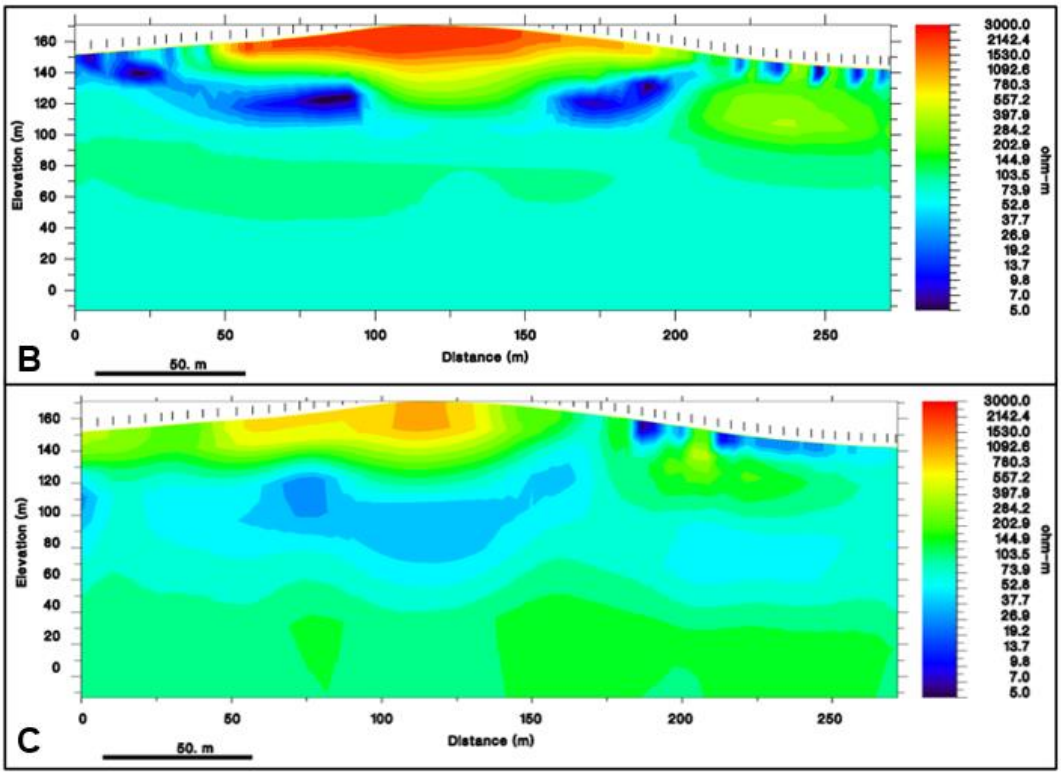

Figure 51 - Resistivity sections for the frequencies 22,1 kHz (B) and 23,4 kHz (C) of profile 5 (sections obtained with VLF2Dmf software).

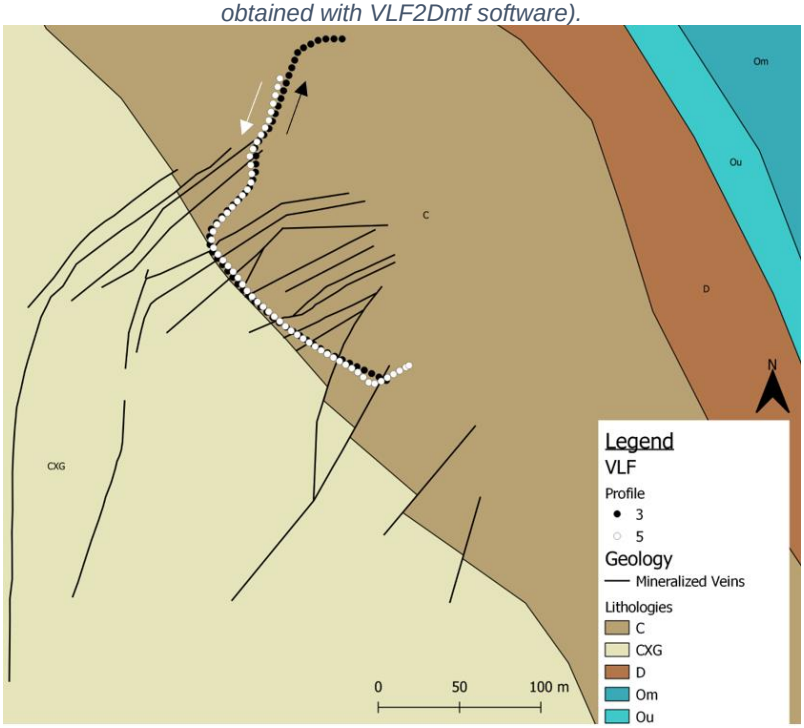

Figure 52 - Map of Alto do Sobrido with the location of profiles 3 and 5 (directions marked with arrows), the mineralized veins and the lithologies present (C – Carboniferous; D – Devonian; Ou – Upper Ordovician; Om – Middle Ordovician; CXG – Schist-Greywacke Complex).

Profile number 4 comprises 65 stations. This profile was made entirely within the rock formations of the Carboniferous. Unlike what happen in the other profiles, the three sections here are quite different from each other (Figure 53). There is only one area of lower resistivity that can be observed at approximately 280 meters distance, that appears on all three sections. This area isn't close to any known veins (Figure 54), so it is possible that it corresponds to a vein that isn't mapped yet or to a weathered area.

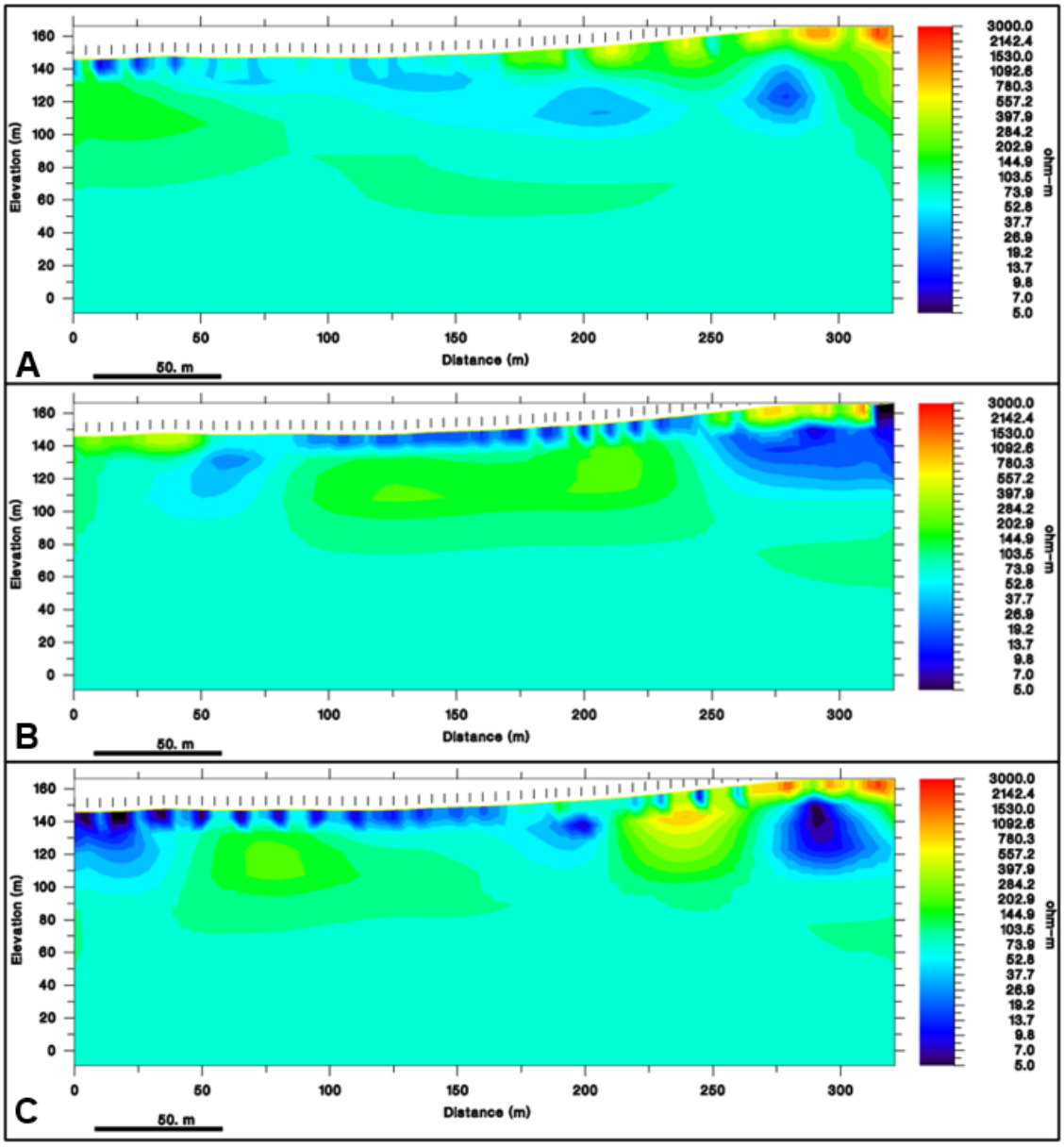

Figure 53 - Resistivity sections for the frequencies 19,2 kHz (A) 22,1 kHz (B) and 23,4 kHz (C) of profile 4 (sections obtained with VLF2Dmf software).

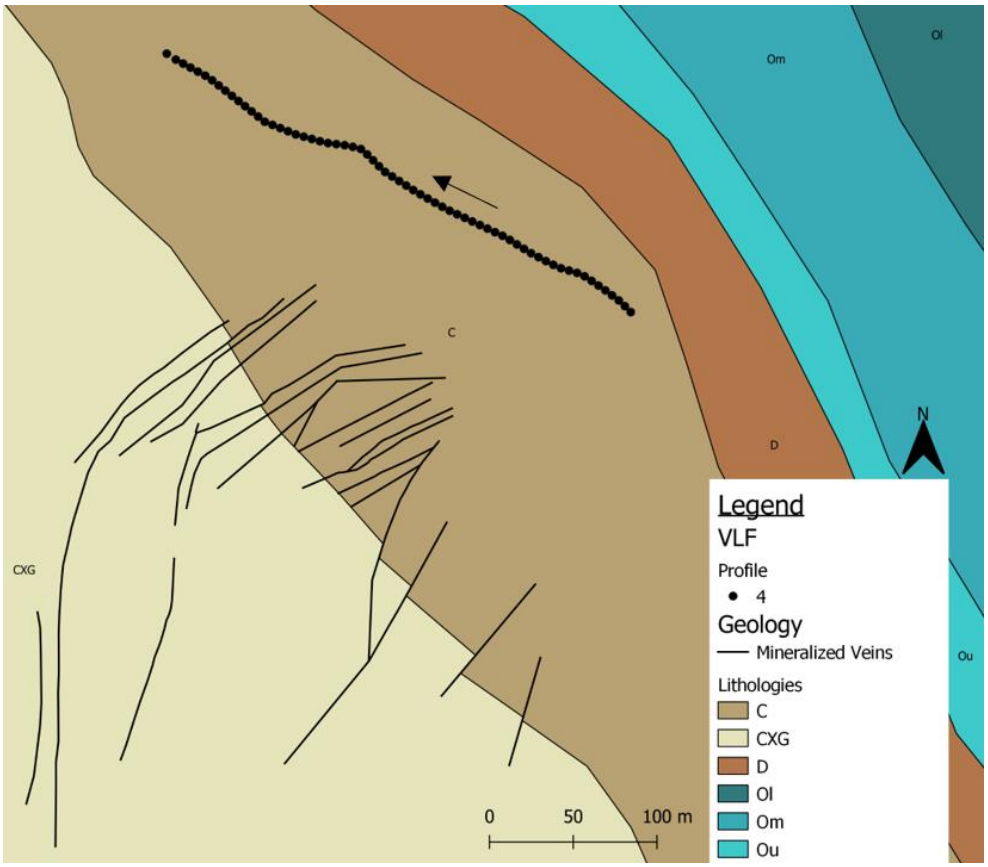

Figure 54 – Map of Alto do Sobrido with the location of profile 4 (direction marked with an arrow), the mineralized veins and the lithologies present (C – Carboniferous; D – Devonian; Ou – Upper Ordovician; Om – Middle Ordovician; Ol – Lower Ordovician; CXG – Schist-Greywacke Complex).

For a better analysis and understanding of the relations between the VLF sections, 3 of them were projected in 3D along with the lithologies and mineralized veins (Figure 55).

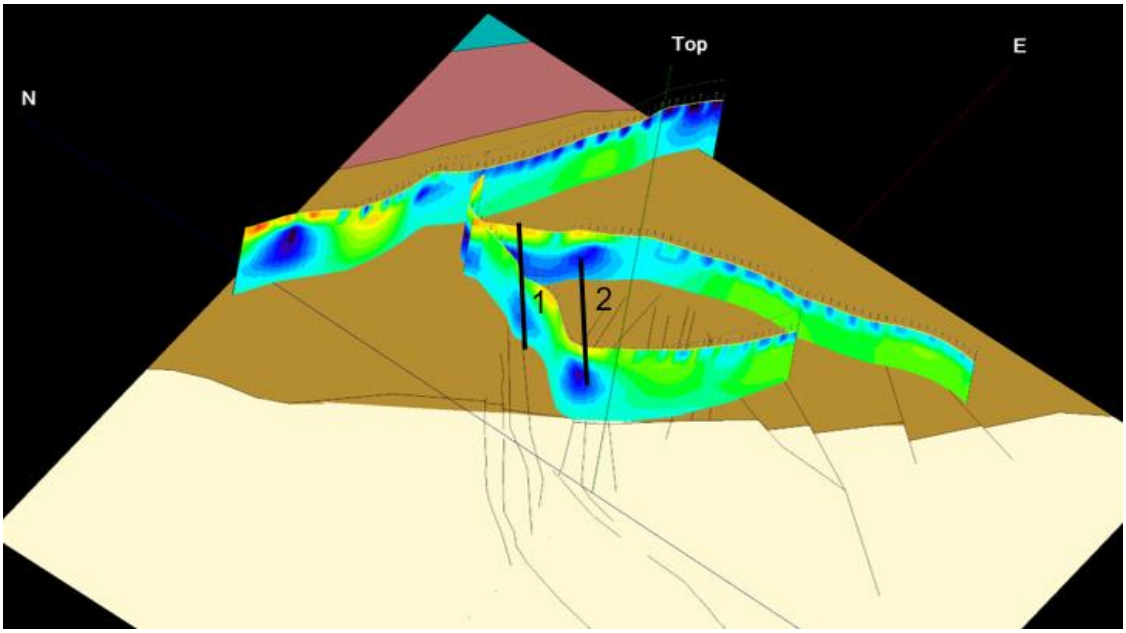

Figure 55 – Sections of frequency 23,4 kHz of profiles 2, 3 and 4, projected in 3D on top of the lithologies and the mineralized veins (image obtained with Rockworks).

In this figure it is possible to observe an alignment marked with 1, of two lower resistivity area, that matches the location and orientation of a mineralized vein. The alignment marked with 2 is parallel to the one marked with 1 and could also be due to a mineralized vein zone, although in this case the veins seem to be turning a little more to the east.

7. Magnetic Survey

7.1 Method

The magnetic method consists of measuring changes in the Earth's magnetic field, caused by variations in the subsurface rocks' magnetic properties, in particular, its magnetic susceptibility.

A material can have two types of magnetism, H: the first is called remnant magnetism and it is inherent to the material; the second is called induced magnetism, where the material is magnetized by an external magnetic field. The overall magnetism of a body is the vector sum of its induced and remnant magnetism (Dentith & Mudge, 2014).

Using a bar magnet, it is possible to better understand the principles of magnetism (Figure 56). The fundamental element of magnetism is the magnetic pole. These can be either positive or negative, which are referred to as north and south poles, respectively. Magnetic poles of equal strength, but opposite polarity always occur as a pair, and are called a Magnetic Dipole.

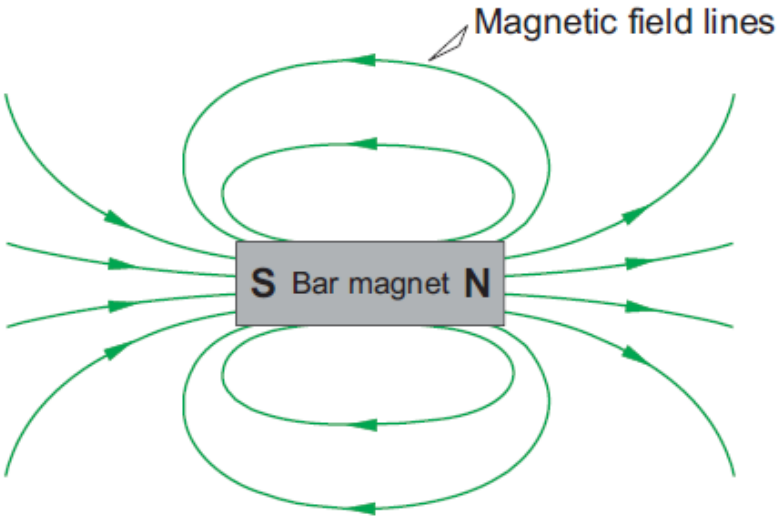

Figure 56 - Bar magnet's field lines. The lines are closer to each other on the poles, which means the field is stronger there (Source: Dentith & Mudge, 2014).

The direction of the magnetic field, B, is assumed to be directed away from the north (positive) pole, towards the south (negative) pole. The field lines are closed, and the strength and orientation vary with the location relative to the poles.

An object's magnetism (or magnetizing force), H, on the SI measurement system, is defined in terms of an electric current flowing through a loop of wire producing the same magnetism. So, the units used are the amperes/meter (A/m), although, in geophysics, the milliamperes/meter (mA/m) is commonly used. For the cgs measurement system, the magnetism unit is the Gauss (G), which corresponds to 1000 A/m.

For the strength of the magnetic field, B, the SI unit used is the tesla (T), but this unit is too large to be used in geophysics, so the nanotesla (nT) is preferred. The cgs unit used is the gamma (γ), where 1 γ is equal to 1 nT.

Magnetism is associated to few elements (Fe, Ni, Co, Cr, Mn and some rare earth elements), of which iron is the most common in geologic materials. Iron is one of the most abundant elements on Earth, consisting of around 28 to 33% of its mass, and it occurs in all the Earth's layers (core, mantle and crust) (Moskowitz *et al*., 2015).

When a material is placed in a magnetic field, it may acquire magnetization, M, in the direction of that field. This process is called induced magnetization or magnetic polarization, and it is the result of the alignment of elementary dipoles within the material (Kearey *et al*., 2002).

The intensity of the induced magnetization, M_i, is proportional to the intensity of the magnetism, H, of the inducing field through:

$$M_i = kH$$

Where k, is the magnetic susceptibility of the material. Due to both H and M_i being measured in A/m, the magnetic susceptibility, k, is dimensionless. When a magnetic material is placed in a magnetic field, the magnetization it acquires, gives rise to another magnetic field in the region occupied by that material (Kearey *et al*., 2002)

Types of Magnetism

The magnetic properties of a material are established by the electron spins and their orbital motions in the atoms, the concentration of magnetic atoms or ions, the interaction between the atoms and the molecular lattice structure. Due to this, there are different types of magnetism: Diamagnetism, Paramagnetism, Ferromagnetism.

Diamagnetic materials are the ones where the atomic electron spins align in a way that their magnetic dipoles are in opposition to the external magnetic field. These have a weak negative magnetic susceptibility. In geophysical surveying this type of materials can be considered non-magnetic.

Paramagnetic materials' electron spins line up to make their magnetic dipoles in the same direction as the external magnetic field. These show a weak positive magnetic susceptibility.

To understand ferromagnetism, the concept of magnetic domains is useful. These domains are volumes in the structure of a material, within which the magnetic vectors are parallel.

A material is non-magnetic when the domains are randomly oriented, so that they cancel each other (Figure 57.a). When an external magnetic field is applied, normally the Earth's magnetic field, the domains align with this external field and the material becomes magnetic with an induced magnetization (Figure 57.b). The more domains that align, the greater the magnetism, with the highest magnetism possible being acquired when all the domains are aligned (Figure 57.c). Iron is the most important ferromagnetic material, but materials with this kind of magnetism rarely occur in the nature (Dentith & Mudge, 2014).

If the external field is sufficiently strong it can cause irreversible changes to the domains, and the material acquires remnant magnetism. Otherwise, the domains reverse to their original state (Dentith & Mudge, 2014).

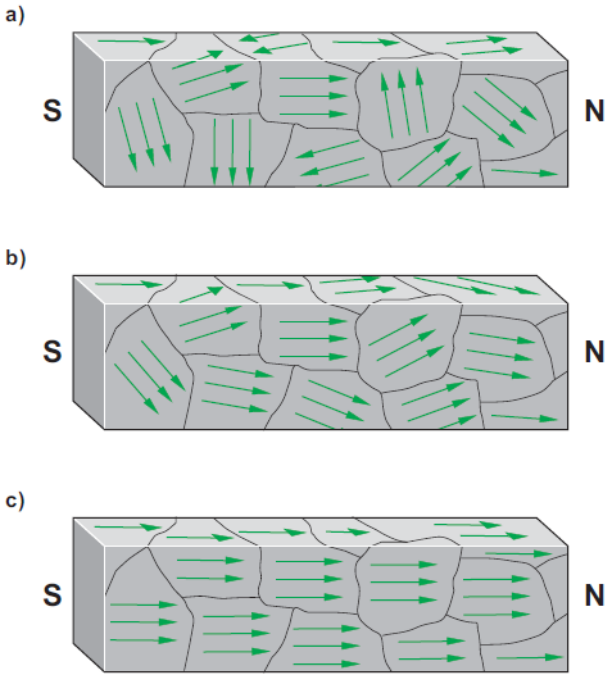

Figure 57 – Schematic illustration of a piece of iron's magnetic domains: (a) Magnetic domains are randomly oriented in an unmagnetized piece of iron; (b) Alignment of the domains due to the presence of an external field; (c) All the domains are aligned, acquiring magnetic saturation. (Source: Dentith & Mudge, 2014).

Within ferromagnetism there are three types (Figure 58): Ferromagnetic, Antiferromagnetic and Ferrimagnetic.

In the ferromagnetic type, the intra-domain magnetic dipoles are parallel, and the material has a high magnetic susceptibility and an intrinsic magnetism. The antiferromagnetic type is when the intra-domain magnetic dipoles are antiparallel and have equal strength. And the ferrimagnetic type is when the magnetic dipoles are

antiparallel, but their strength is not equal. Ferrimagnetic materials have high magnetic susceptibility and can acquire remnant magnetism.

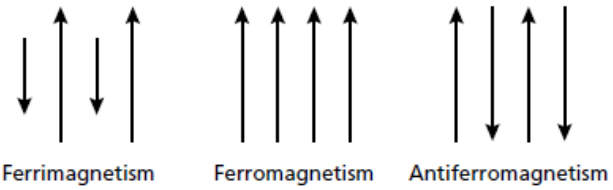

Figure 58 - Schematic representation of the strength and orientation of elementary dipoles for the different types of ferromagnetism (Source: Kearey et al., 2002).

Rock Magnetism

In general, most rock forming mineral have a very low magnetic susceptibility, and the rocks' magnetic character is usually due to small proportions of magnetic minerals that they contain.

The most common magnetic mineral is magnetite (Fe_3O_4), whose Curie temperature is 578 ºC. It is acceptable to classify the magnetic behaviour of rocks according to their overall content in magnetite, even though the size, shape and dispersion of magnetite can influence a rock's magnetic character.

Basic igneous rocks usually have a high magnetite content, which makes them highly magnetic. With the increase in acidity of igneous rocks, the content in magnetite tends to decrease. Metamorphic rocks also have a variable magnetic character.

The magnetite content and, thus the overall magnetic susceptibility, of rocks is, in general, varying, and there can be significant overlaps between different lithologies. We must also take into account that other minerals also contribute to the bulk magnetic susceptibility, of a certain rock formation. Usually, it is not possible to determine the lithology with only magnetic information. Nonetheless, sedimentary rocks are effectively non-magnetic. When magnetic anomalies are observed on sedimentary areas, this is normally due to an underlying igneous or metamorphic basement or due to intrusions on the sediments.

The Earth's Magnetic Field and Magnetic Anomalies

Magnetic anomalies caused by rocks are localized effects that overlay the Earth's normal magnetic field (or the geomagnetic field). Due to this it is necessary to comprehend the geomagnetic field in order to understand the magnetic anomalies. Unlike the Earth's gravity field, the geomagnetic field has irregular variations in both orientation and intensity with latitude, longitude and time (Kearey *et al*., 2002).

The relatively stable main field that originates from the Earth's core is known as the internal field. This is the field responsible for the induced and remnant magnetism on rocks. There is also an unstable component of the geomagnetic field, that is associated with variations on time scales of a second to months. This component occurs due to sources external to the Earth and is known as the external field. These variations that happen, due to the external field, during a magnetic survey need to be corrected, so that the measurements reflect only the spatial variations in the field (Dentith & Mudge, 2014).

The Earth's total magnetic field vector, B, has a vertical component, Z, and a horizontal component, H, that points to the magnetic north (Figure 59). The angle formed between B and H is the inclination, I, and the angle between H (magnetic north) and the geographic north is the declination, D.

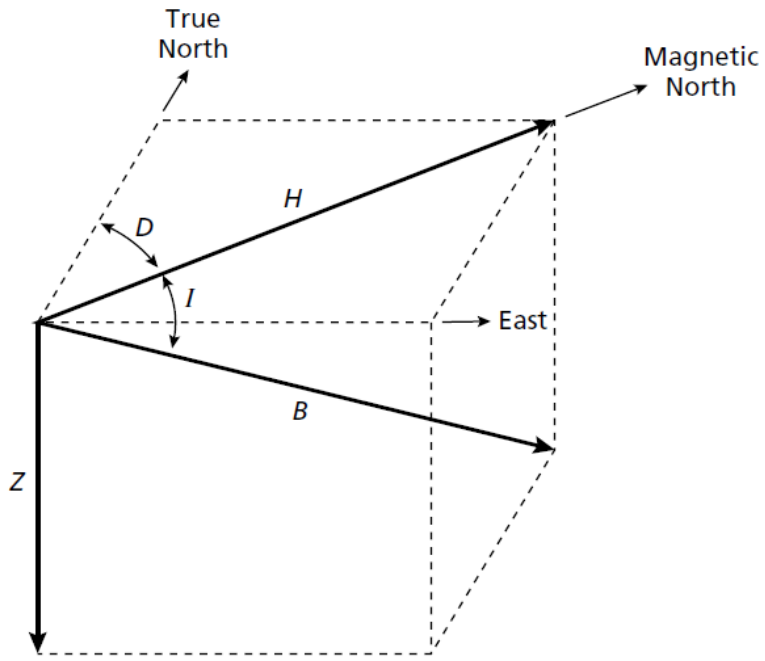

Figure 59 - The geomagnetic elements of the Earth's field (Source: Kearey et al., 2002).

The intensity of the geomagnetic field, B, varies from 25 000 nT, on the equator, to around 70 000 nT in the poles. The inclination of the magnetic field is generally downwards in the northern hemisphere, and upwards in the southern hemisphere, being vertical in the magnetic poles (+90º in the magnetic north pole and -90º in the magnetic south pole). The inclination is zero in the magnetic equator, which does not always coincide with the geographic equator.

The internal field is described by a mathematical model, known as the International Geomagnetic Reference Field (IGRF) (Figure 60), which is updated every five years. There is also a provisional field, that corresponds to a prediction of the changes that will occur to the geomagnetic field for the next five years (Figure 61).

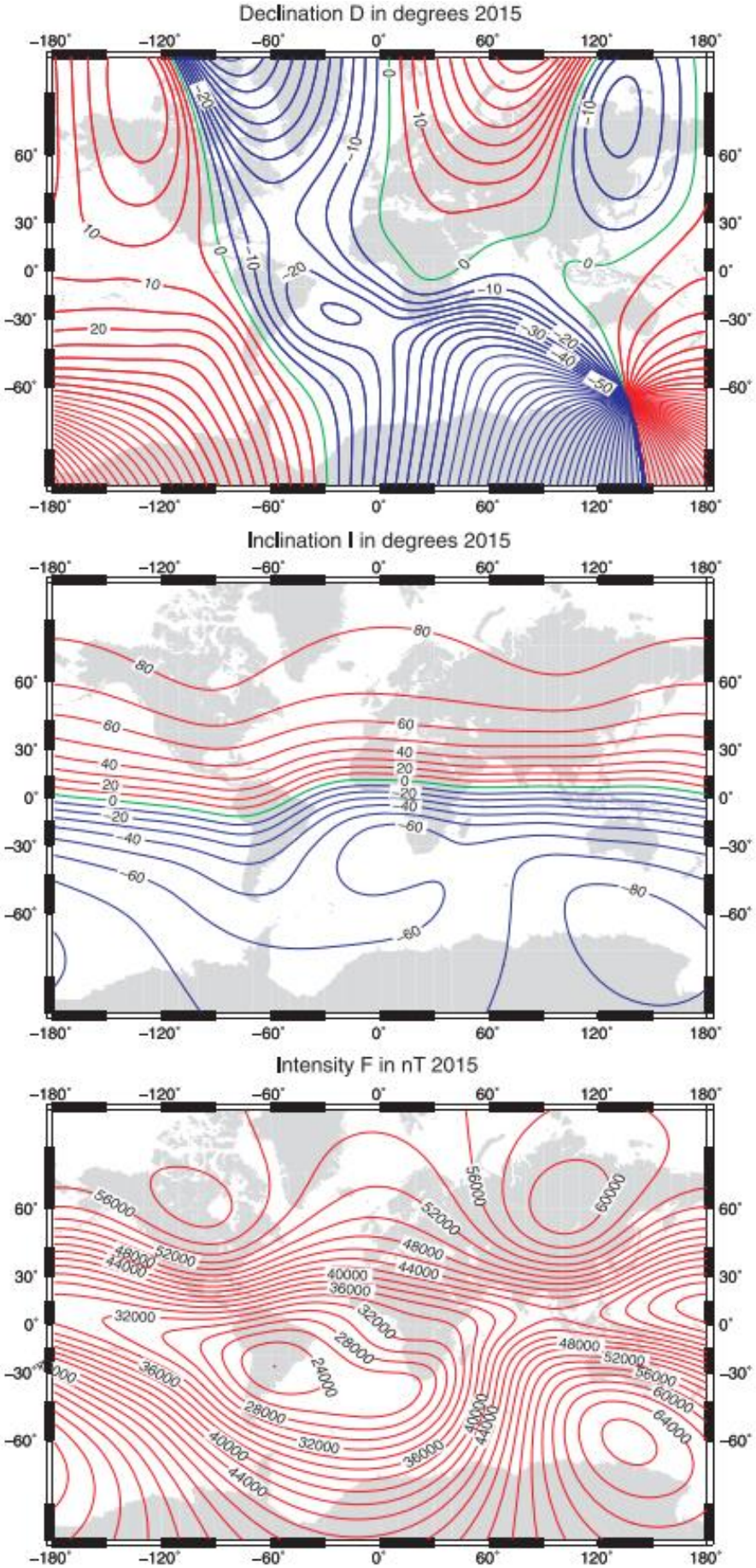

Figure 60 - International Geomagnetic Reference Field (Source: Thébault et al., 2015).

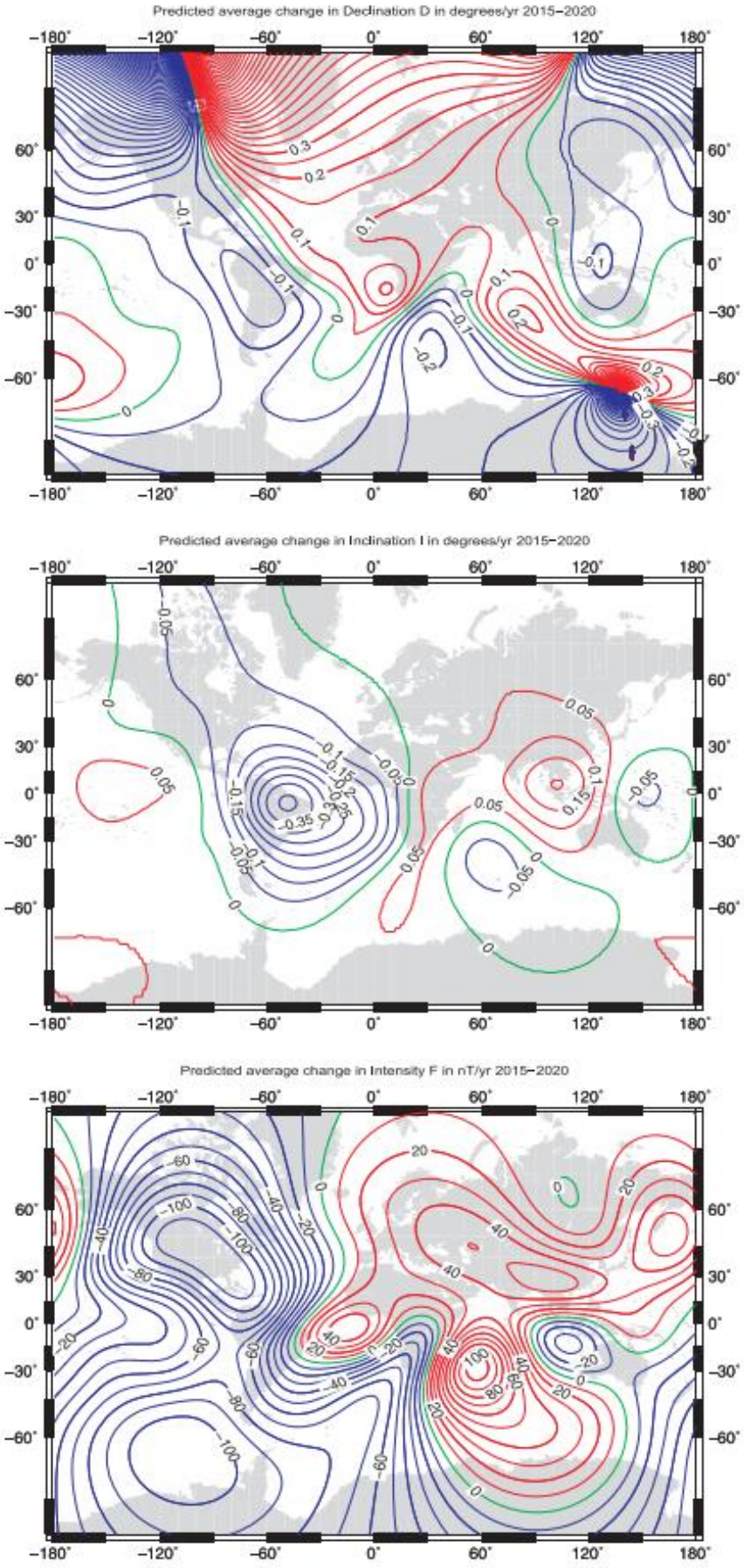

Figure 61 – 2015 International Geomagnetic Reference Field's predicted changes for the next five years (Source: Thébault et al., 2015).

Just like what happens with gravity surveying, in magnetic exploration it is also necessary to do a reduction of the data. This reduction or correction of the magnetic data is mainly aimed at removing the effects of temporal variations in the geomagnetic field, that occur during the survey process.

Diurnal Variations Correction

Variations in the field strength that occur in very short periods of time are usually manually removed from the survey data and the base station record.

Once this is corrected, it is necessary to correct the diurnal variations. These are the variations that occur due to electrical currents flowing in the ionosphere and are associated with radiation from the Sun. Diurnal variations can range up to 30 nT and are at a minimum at night. They also vary with latitude and are higher in the equatorial areas.

To correct these variations, it will be necessary to make repeated readings at a base station, similar to what was done for the correction of instrumental drift in the gravity survey. Since magnetometers do not drift, these readings are made solely to correct for the temporal variations.

With these readings it is possible to correct each recording, by knowing at what time they were done.

Geomagnetic Field Correction

The geomagnetic field appears as a large-wavelength regional field, which can be removed in order to increase the resolution of magnetic anomalies associated with geological sources.

For surveys at a small scale, the geomagnetic field varies smoothly and for small amounts, so it can be removed as a single regional field.

Elevation and Terrain Corrections

The Earth's Magnetic Field doesn't vary much with the distance to the centre of the Earth. It goes from 0,03 nT/m at the poles to -0,015 nT/m at the equator. In the presence of geological sourced anomalies, these variations can be important, but this is usually not a problem for ground surveys, so the elevation correction isn't usually applied.

Topography can also have significant influence on ground magnetic surveys, but it depends on the magnetic properties of those topographic features, which isn't completely predictable. Due to this, topography corrections aren't normally applied.

With the correction of the diurnal variations and the geomagnetic field, the data should only show magnetic anomalies, which correspond to the spatial variations caused by the varying magnetic properties of the subsurface.

First Vertical Derivative

First vertical derivative (1VD) tends to sharpen the edges of anomalies and enhance shallow features. The vertical derivative map is much more responsive to local influences than to broad or regional effects and therefore tends to give sharper picture than the map of the total field intensity. Thus, the smaller anomalies are more readily apparent in areas of strong regional disturbances. In fact, the first vertical derivative is used to delineate high frequency features more clearly where they are shadowed by large amplitude, low frequency anomalies.

$$1VD = \partial M \partial z$$

1VD maps are commonly used to enhance the shorter wavelength signal. In the current work we noticed how well the linear features were defined compared to the total field maps (Figures 63, 64 and 65).

Field Work

For the magnetic survey, two different equipments were used: a GEM Systems' GSM-19 Magnetometer (resolution of 0,01 nT and an accuracy of 0,2 nT), which is a portable, high sensitivity, microprocessor-based equipment, and Elsec Proton Magnetometer with a resolution of 1 nT.

The survey started with measurements made in 3 profiles, with a spacing of 5 meters between stations, and afterwards were added some more stations with a higher spacing between them. The first stations, made in profiles, were done with a smaller spacing because they are located in the area of previous mining works where the interest was higher. The stations performed afterwards were done to add more information about the surroundings of this area, in order to obtain a more complete map. There is a total of 228 station (Figure 62), with one measurement made per station.

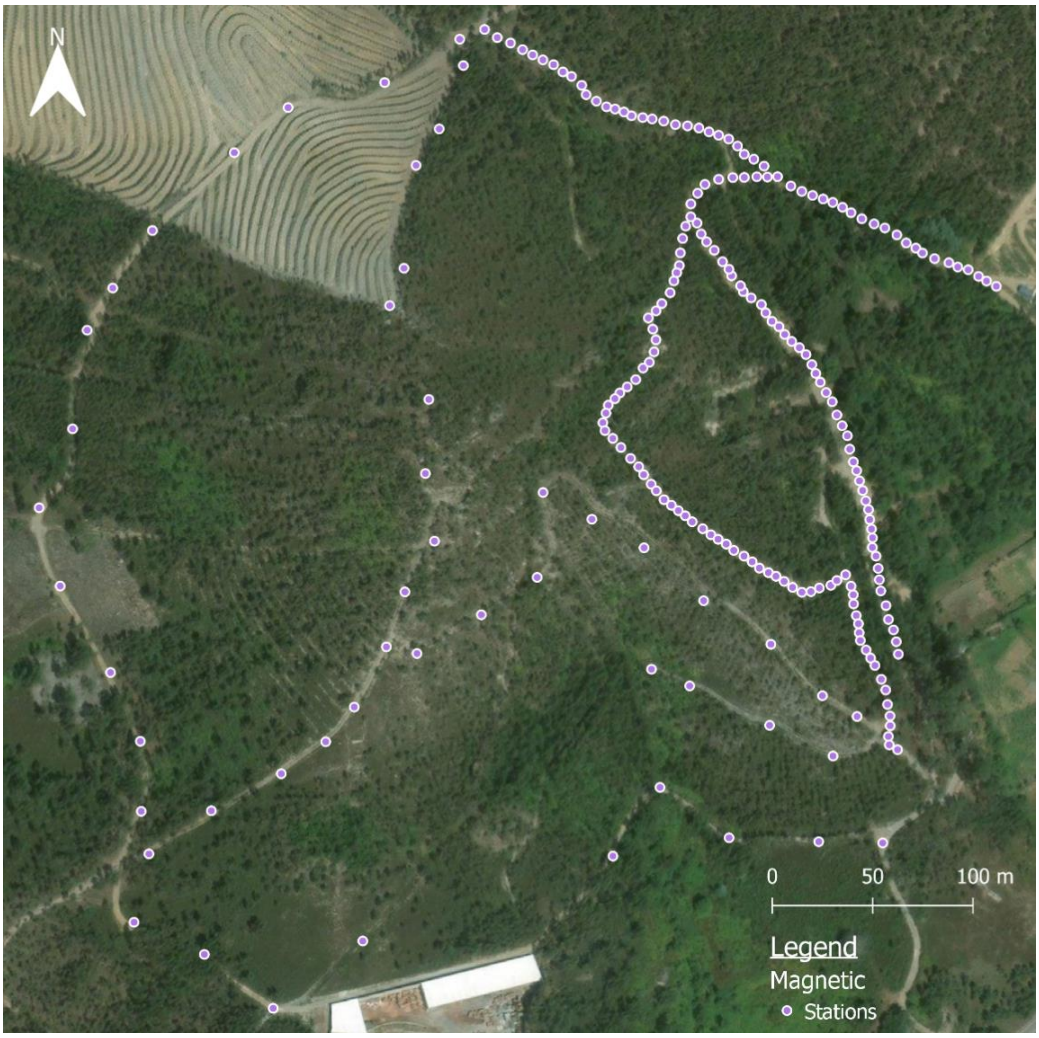

Figure 62 - Stations done for the magnetic survey (image acquired with QGIS).

7.2 Results and Discussion

Before creating maps with the measurements made in the 228 stations of the survey it was necessary to correct the field values from the diurnal variations of the magnetic field. This was done using base measurements at the beginning and end of each survey period (made in segments of just a few hours). The values that were obtained after the correction can be found in Table C in Appendix 3. The minimum, maximum and mean values of all stations can be found in Table 9.

Table 9 - Minimum, maximum and mean values obtained from the field values of all the stations.

	Field (nT)
Minimum	44951,5707
Maximum	45077,5300
Mean	45012,0122

Once the values were corrected an interpolation map was created from them (Figure 63).

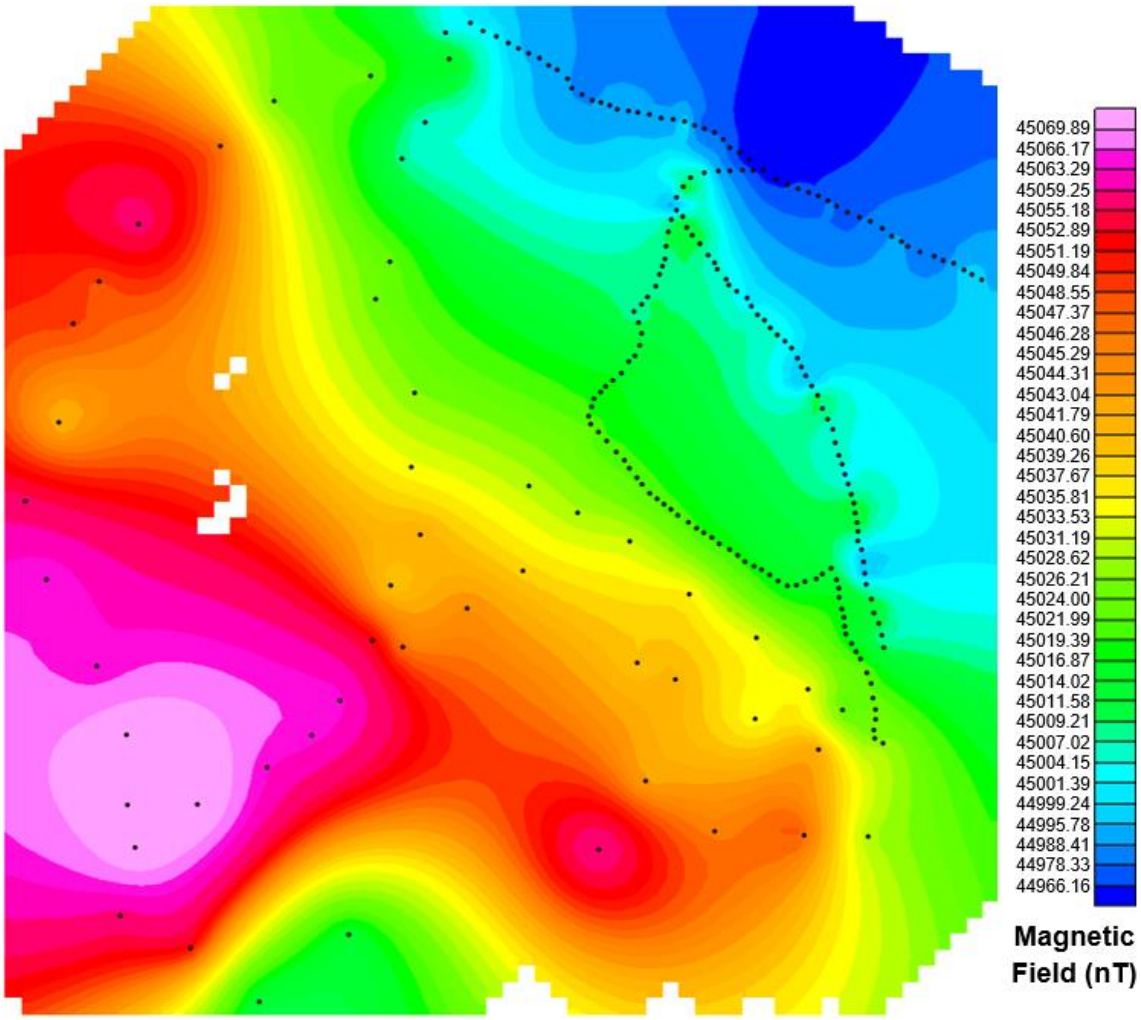

Figure 63 - Interpolation of the magnetic field values obtained in the survey with the magnetic stations (black dots) (map created with Oasis Montal).

In this map it is possible to observe a decreasing general tendency in the magnetic field from the SW to the NE. To this map was applied a bandpass filter to obtain a residual map where the anomalies are visible (Figure 64). To make these smaller scale anomalies even more distinct, a vertical derivative filter was applied (Figure 65).

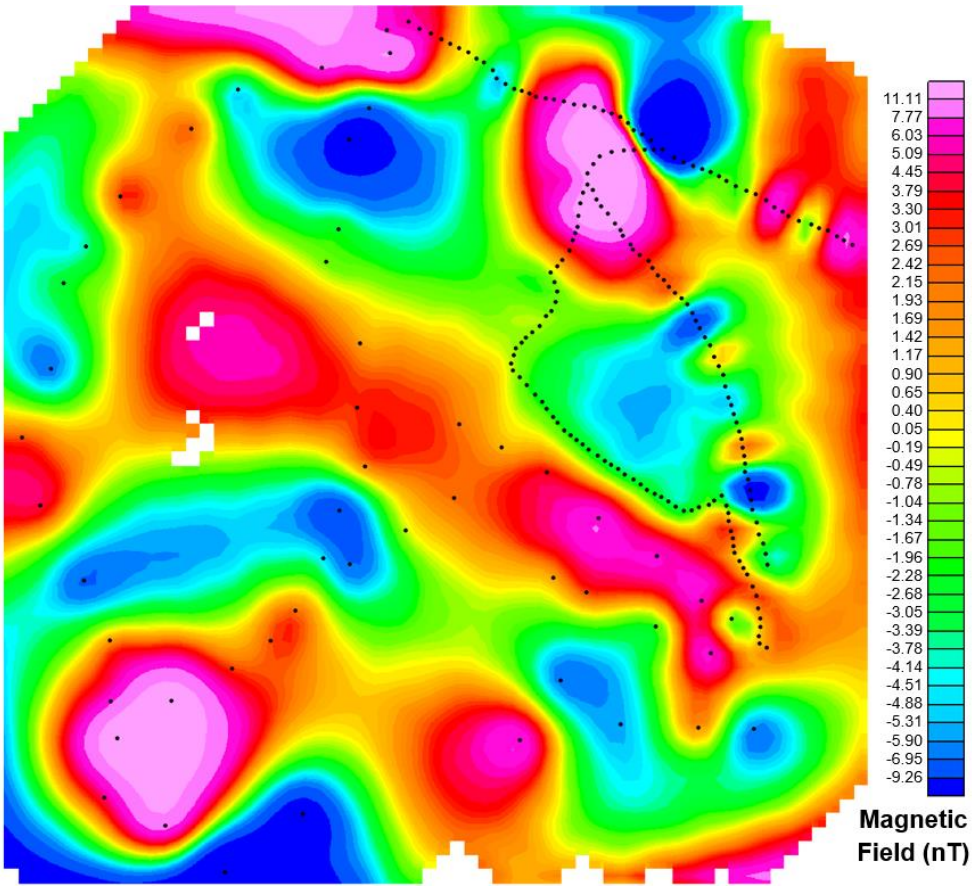

Figure 64 – Residual anomaly map obtained through a bandpass filter (map done with Oasis Montaj).

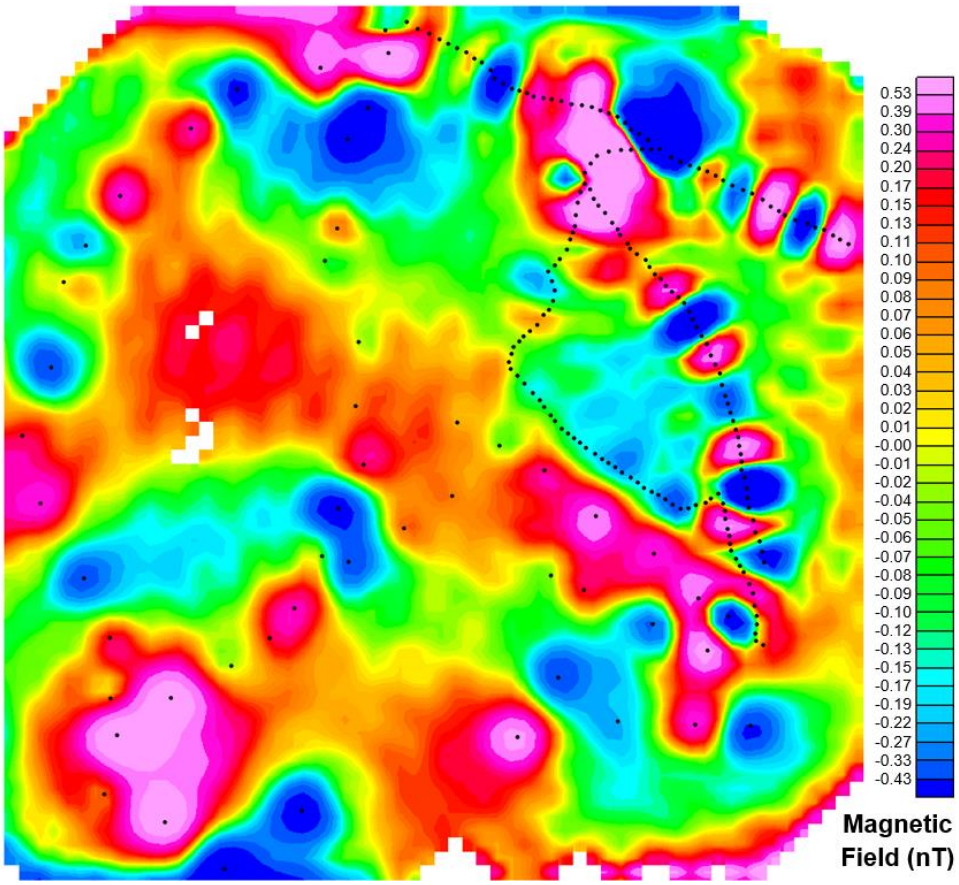

Figure 65 - Residual anomaly map with anomalies more visible, obtained through a vertical derivative filter (map created with Oasis Montaj).

In the Northern hemisphere at mid latitudes, such as ours, a magnetic anomaly, due to a mass or vertical dyke, generally occurs when a there is a high field value followed by a low field value. This is observed throughout the entire map, but there are some clear smaller anomalies located in the area of the old mining works of Alto do Sobrido, in the eastern part of the maps. These smaller anomalies could occur due to the spacing in this area being smaller, but since they are located in the area of mining works it is also possible that they appear due to the presence of mineralized veins or even smaller faults that are associated with the DBSZ (Figure 66). These can also be due to the presence of diabase/dolerite veins that are known to have magnetite and that are usually associated with the mineralizations.

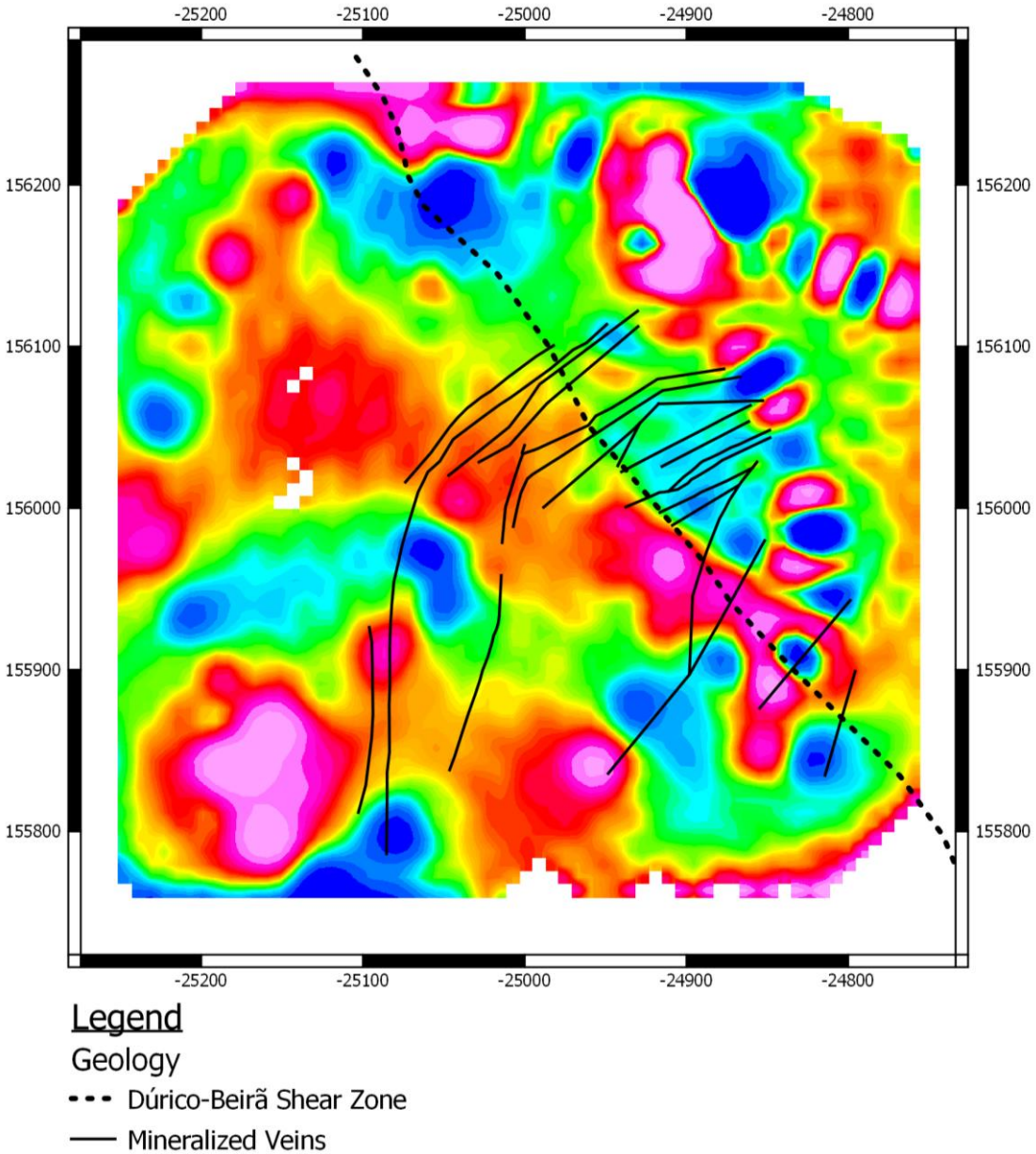

Figure 66 - Vertical derivative residual anomaly map with the mineralized veins mapped by Kernow Mining (2009) on their 5th report of activities (Coordinates: ETRS89 TM06).

8. Radiometric Survey

8.1 Method

Radiometric surveying is a passive geophysical method that measures naturally occurring radioactivity in the form of gamma-rays (γ-rays). Most of the radiation comes from mineral species that contain radioactive isotopes of potassium (K), uranium (U) and thorium (Th). Historically in mineral prospecting, radiometric surveys were used in the identification of anomalies caused by outcropping and highly radioactive deposits of uranium. Nowadays, it is used more towards geological mapping than pure anomaly detection (Dentith & Mudge, 2014).

An atom with equal number of protons and electrons is electrically neutral. An atom's number of protons corresponds to its atomic number (Z), which defines the atom's chemical properties, as well as its place in the periodic table of elements. The number of neutrons in the atom's nucleus is called the neutron number (N), and the sum of the neutron number with the atomic number gives the atomic mass number (A) of the element. Atoms of the same element with different neutron numbers are called isotopes and are distinguished by their atomic mass number (Keary *et al*., 2002; Dentith & Mudge, 2014).

Some isotopes are unstable (i.e. radioactive) and spontaneously emit radiation when they disintegrate into a more stable isotope. There are three types of emissions that are known as alpha- (α), beta- (β) and gamma- (γ) radiation. The process of emitting each type of radiation is called α-decay, β-decay and γ-decay, respectively. The original isotope, pre-decay, is called the parent, while the post-decay isotopes are called daughters. Each daughter isotope can themselves be radioactive, which forms a decay series that continues until a stable (i.e., non-radioactive) isotope is produced (Keary *et al*., 2002; Dentith & Mudge, 2014).

Alpha- and beta-decays correspond to the emission of particles: a helium nucleus (^4He) for alpha-decay and an electron (β^-) or positron (β^+) for beta-decay (Figure 67). Whereas gamma-decay is the emission of high frequency electromagnetic radiation. The particles of alpha- and beta-decay originate from within the atomic nuclei, which causes a change in atomic number, therefore creating a different element. Gamma-decay follows alpha- or beta-decays and does not alter the elements atomic or mass number. Another process that produces gamma-radiation is called K-capture. It is when an inner-orbital electron is captured by the nucleus and a proton is converted to a neutron, which causes a different element to be created (Figure 67). Gamma-radiation emission corresponds to the decrease in energy from the parent's excited state to the daughter's grounded or less excited state. The amount of energy depends on the parent-daughter

combination and since that energy can be measured, it is possible to infer the type of emitting isotope present (Keary *et al*., 2002; Dentith & Mudge, 2014).

$$^{A}_{Z}\text{Parent} \rightarrow {}^{4}_{2}\text{He} + {}^{A-4}_{Z-2}\text{daughter} \qquad \alpha\text{-emission}$$

$$^{A}_{Z}\text{Parent} \rightarrow e^{-} + {}_{Z+1}{}^{A}\text{daughter} \qquad \beta\text{-emission}$$

$$^{A}_{Z}\text{Parent} + e^{-}_{\text{orbital}} \rightarrow {}_{Z-1}{}^{A}\text{daughter} \qquad \text{K-capture}$$

Figure 67 - Chemical equations for alpha- and beta-decays, as well as K-capture mechanism (Dentith & Mudge, 2014).

Alpha-, beta- and gamma-radiations have very different penetrating properties. Alpha and beta particles are absorbed by a negligible thickness of rock and soil. However, gamma-radiation can penetrate significantly further than the other two, which makes it the type of emission mainly used in geophysical radiometric surveys. But only gamma-rays that originate from a few tens of centimetres below the surface can be detected on a radiometric survey (Keary *et al*., 2002; Dentith & Mudge, 2014).

There are three isotopes of importance for radiometric surveys: potassium-40 (^{40}K), thorium-232 (^{232}Th) and uranium-238 (^{238}U). Potassium-40 decays in two ways: β-emission or K-capture. In 89% of the cases ^{40}K decays by β-emission to ^{40}Ca and on the other 11%, it decays by K-capture to ^{40}Ar. When K-capture occurs, there is the emission of gamma-rays with an energy of 1.46 MeV, which is a known peak in the ^{40}K's energy spectrum. For ^{232}Th that peak is at 2.62 MeV, and for ^{238}U it is at 1.76 MeV (Figure 68) (MeV = 10^6 electronvolts, where one electronvolt is the energy acquired by a particle of unit charge falling through a potential of one volt) (Keary *et al*., 2002; Dentith & Mudge, 2014).

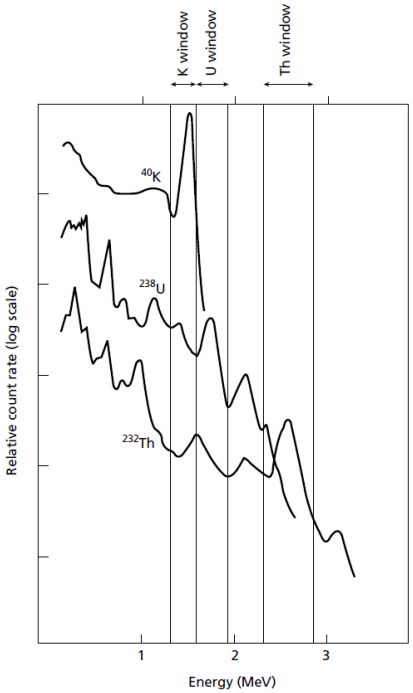

Figure 68 - Energy spectrum for ^{40}K, ^{232}Th and ^{238}U and each measurement window (Keary et al., 2002).

Field Work

The instrument used for radiometric surveying is called a gamma-ray spectrometer. The one used on this study is the model GR-320 Exploranium (Figure 69), which is a portable spectrometer.

A gamma-ray spectrometer is an extension of the scintillation counter or scintillometer. When gamma-rays are photoelectrically absorbed in thallium activated sodium iodide crystals they produce flashes of light, i.e., they scintillate. These flashes of light can be detected by a photomultiplier. These measurements of gamma-radiation on a scintillometer will provide results in counts per minute. A gamma-ray spectrometer can discriminate the source from which the ray is emitted from. Using the intensity of the scintillation pulses, which are proportional to the energy of the original gamma-ray, and knowing the peaks of each element, the spectrometer can display the counts per minute or ppm of each element separately (Keary *et al*., 2002; Milsom, 2003).

Figure 69 - Gamma-ray spectrometer GR-320 Exploranium on the field.

The radiometric survey was accomplished by performing measurements throughout the study area, similarly to what was carried out in the gravimetric survey. There were a total of 43 measured stations (Figure 70), with a minimum of two measurements of 60 seconds being done per station.

These readings provided values of counts converted to either percentage for potassium (K) or ppm for both uranium (U) and thorium (Th). A total radiometric count was also made.

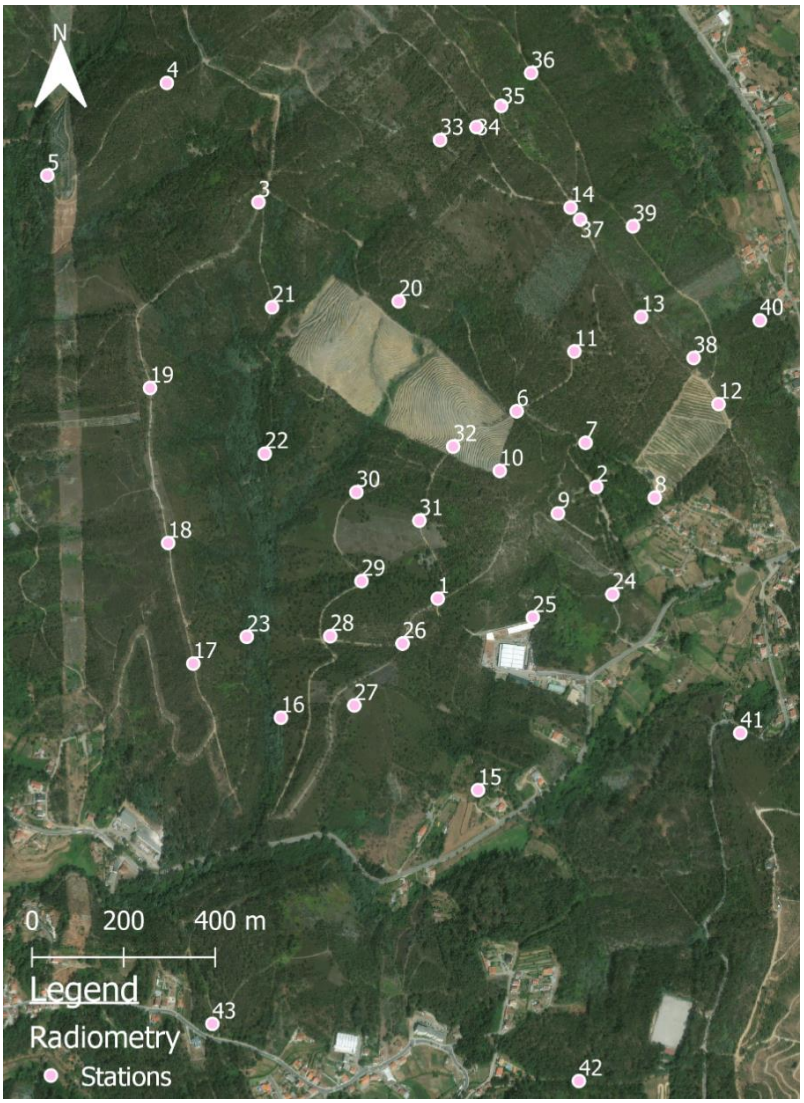

Figure 70 - Stations done for the radiometric survey (image acquired with QGIS).

8.2 Results and Discussion

The concentration and count average values of K, U, Th and Total of the 2 measurements of the 43 stations that were measured during the survey can be found on Table D in Appendix 4.

With these values it was possible to create interpolated maps, using Oasis Montaj software. The resulting maps for each element and for the total with its concentration values can be viewed in Figure 71.

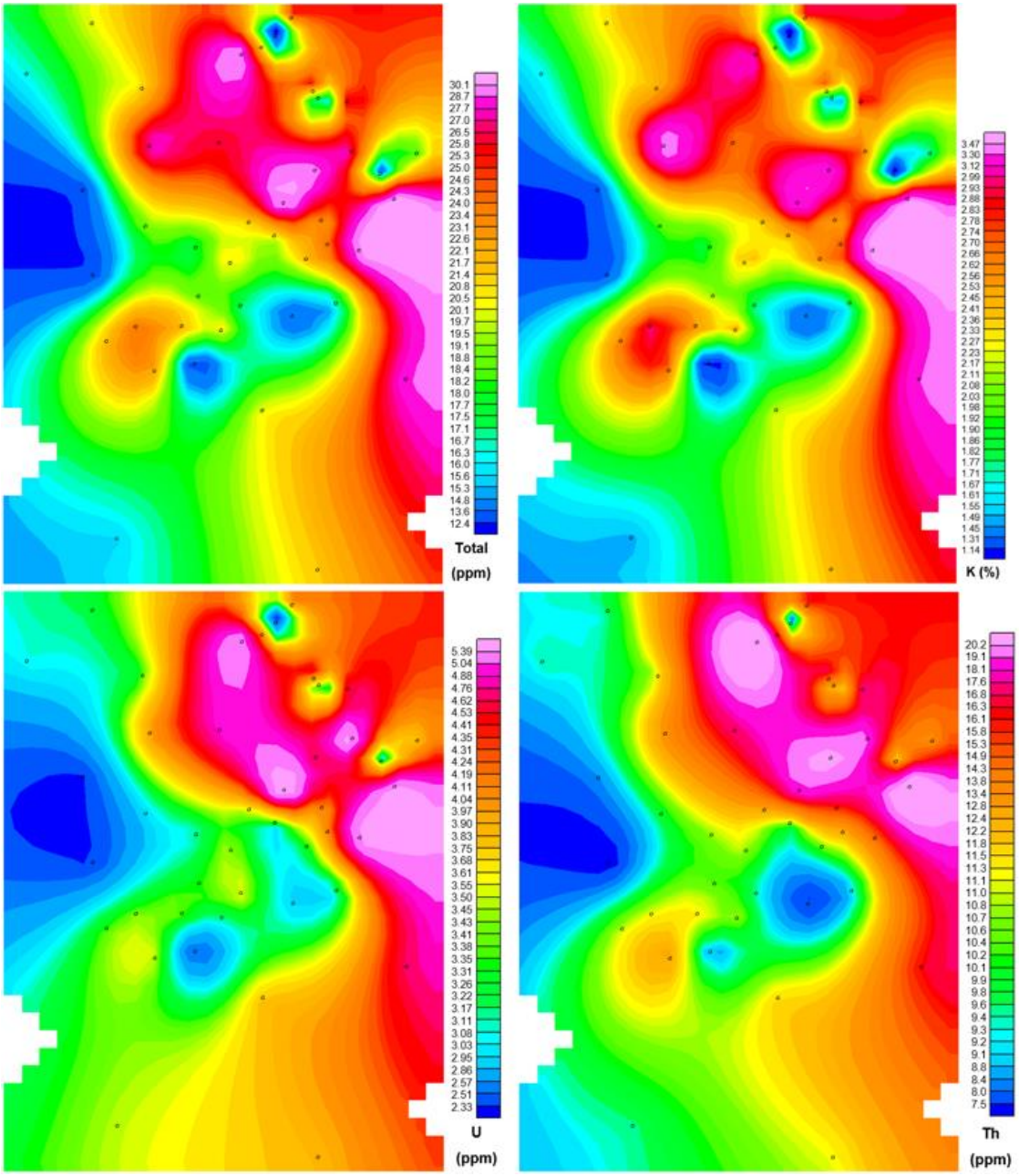

Figure 71 - Interpolation maps for the concentration (% and ppm) of the three elements (K, U and Th) and the total (map created with Oasis Montaj).

Observing Figure 72 it is possible to examine these maps with the mapped lithologies from sheet 13-B of the Geological Maps of Portugal (1:50.000).

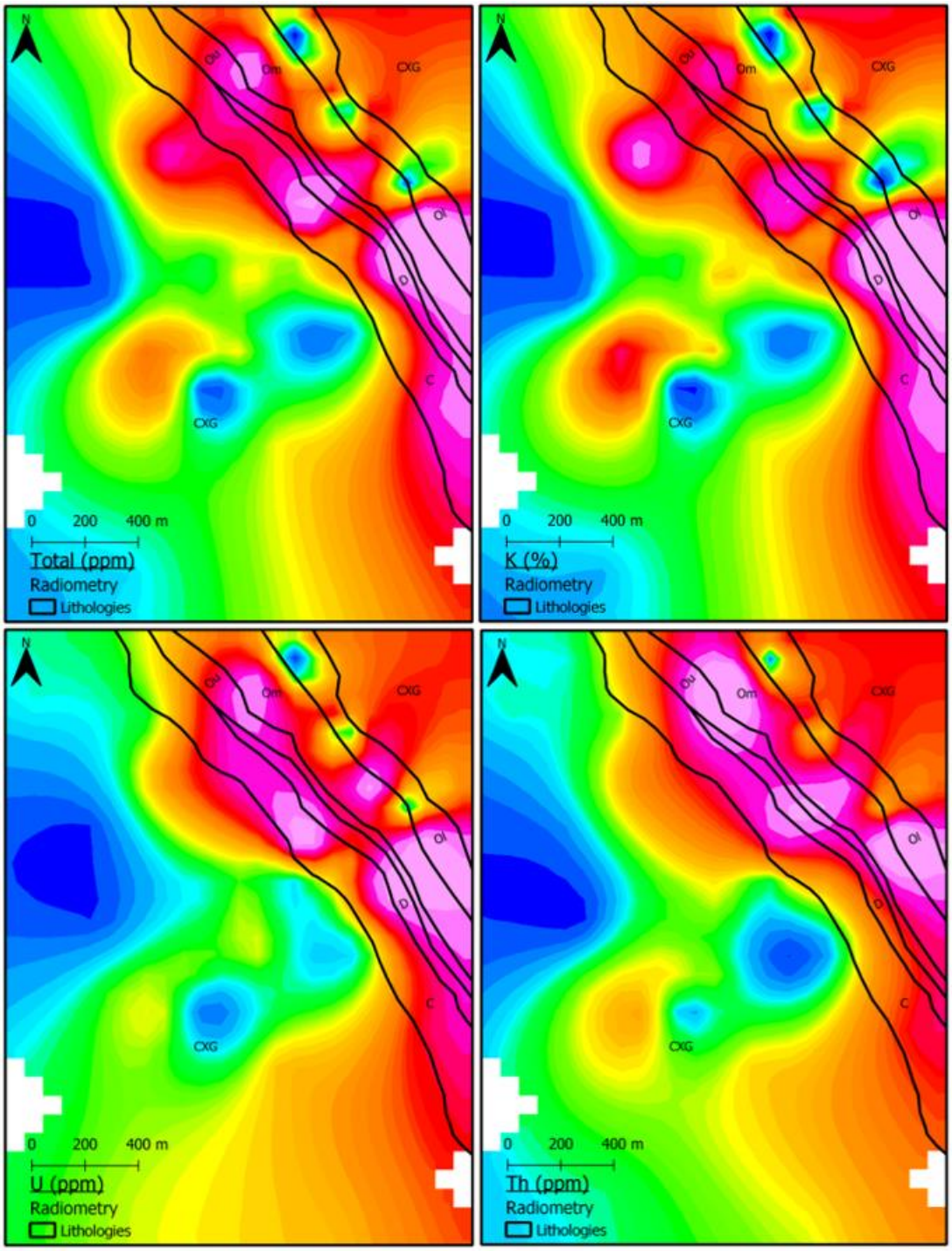

Figure 72 – Maps from Figure 64 with the mapped lithologies from the 13-B Geological Map of Portugal (1:50.000) (C – Carboniferous; D – Devonian; Ou – Upper Ordovician; Om – Middle Ordovician; Ol – Lower Ordovician; CXG – Schist-Greywacke Complex) (images obtained with QGIS).

In most of these maps it is possible to observe small areas of lower concentrations in the NE aligned with an approximate orientation of NW-SE. While performing the measurements in the field on the quartzite formations (Lower Ordovician) it was clear that these measurements were the ones with the lower concentration values of K, U and Total. And by comparing the location of these lower concentration areas with the

geological map, it is possible to assume that these correspond to the location of the quartzites.

When looking at the Th map, this NE areas no longer have lower concentrations, which is also concordant with what was observed in the field for the quartzites.

Where the lithologies from the Carboniferous to the Middle Ordovician are located, higher values occur on all four maps, but when located on the CXG formation the values go down again.

In alternative to the four concentration maps, the following Figure 73 presents a relatively common way of visualizing gamma-ray spectrometry data, which allows the representation of the three elements simultaneously.

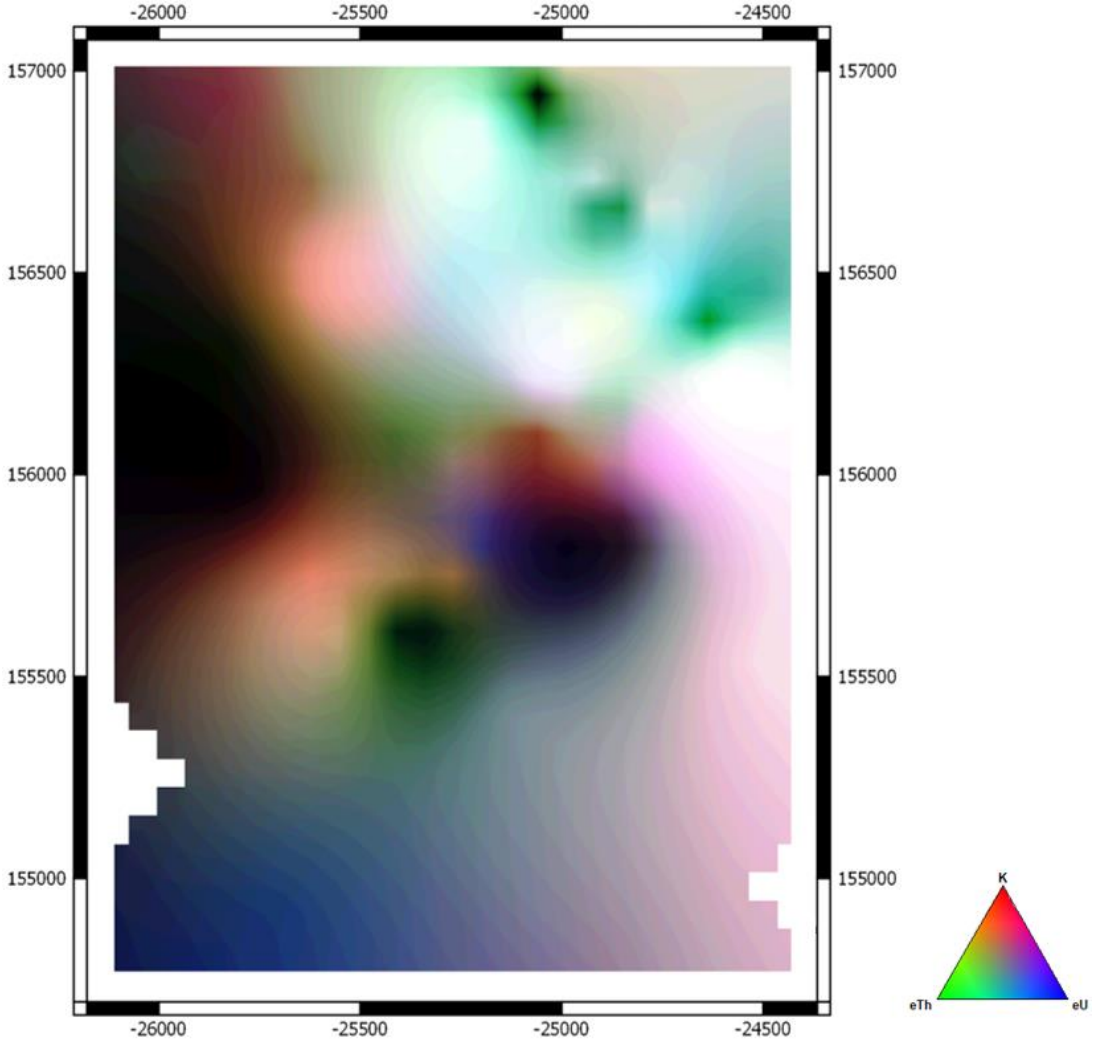

Figure 73 - Ternary representation of the three elements of the gamma-ray spectrometry data (Coordinates: ETRS89 TM06).

9. Correlation Between Methods

9.1 Gravity and Radiometry

As was previously mentioned in the Gravity chapter, there is a hypothesis that the hydrothermal fluids that created the Au-Sb mineralizations could have originated from a granitic source located in depth. Finding a correlation between the radiometric method, which is a method that analyses the concentrations of chemical elements at the near subsurface, and the gravimetric method, which is may be sensitive to density anomalies at greater depths, could contribute to show that this granitic intrusion chemically influenced its embedding rocks all the way to the upper subsurface.

Thus, to test this, a correlation was done between the maps obtained from both methods. Before doing the correlation, it was necessary to normalize the grid maps, to have grids with values between -1 and 1. The normalized maps can be observed in Figures 74 and 75.

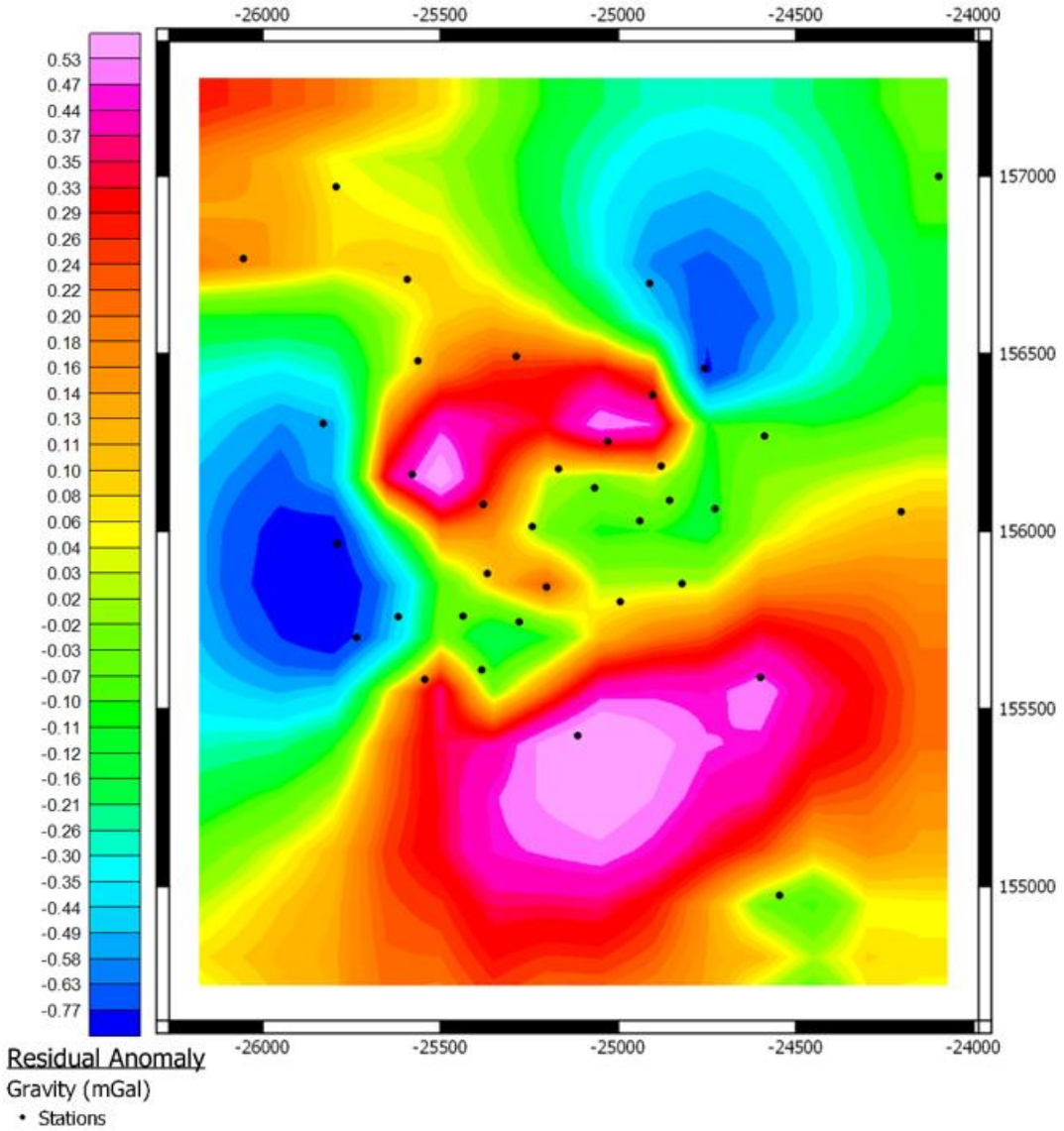

Figure 74 - Normalized gravity's residual anomaly map, cut to the location of the radiometry maps, with the location of the gravity survey stations.

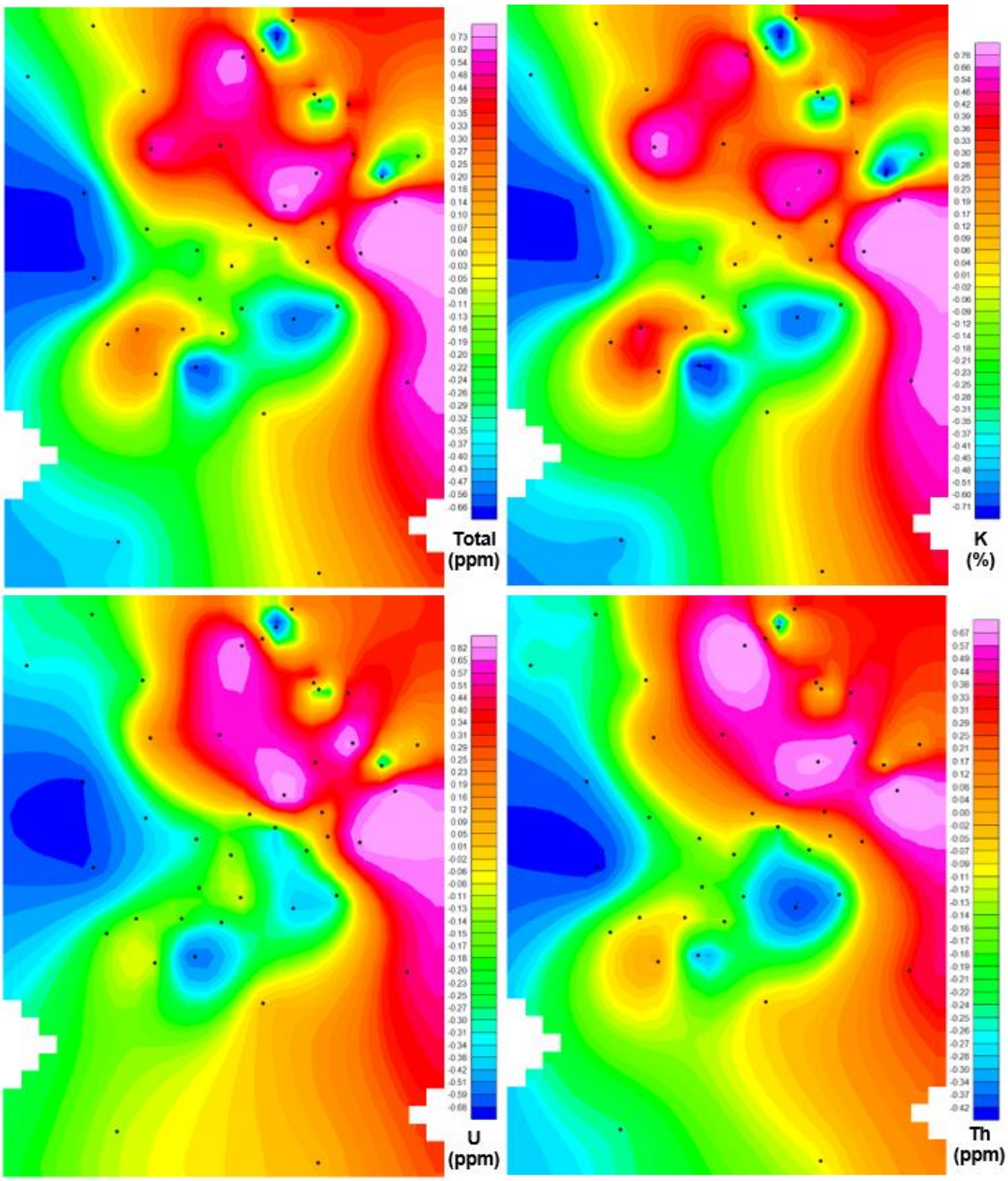

Figure 75 - Normalized radiometry grid maps for concentrations of K, Th, U and total, with the location of the radiometric survey stations.

Once the normalization was done, each of the radiometry maps was multiplied by the gravimetric residual anomaly map. Four correlation maps were obtained (Figure 76). In these maps, correlation occurs when high or low values geographically coincide in both methods, and inverse correlation occurs when high values on one method coincide with low values on the other.

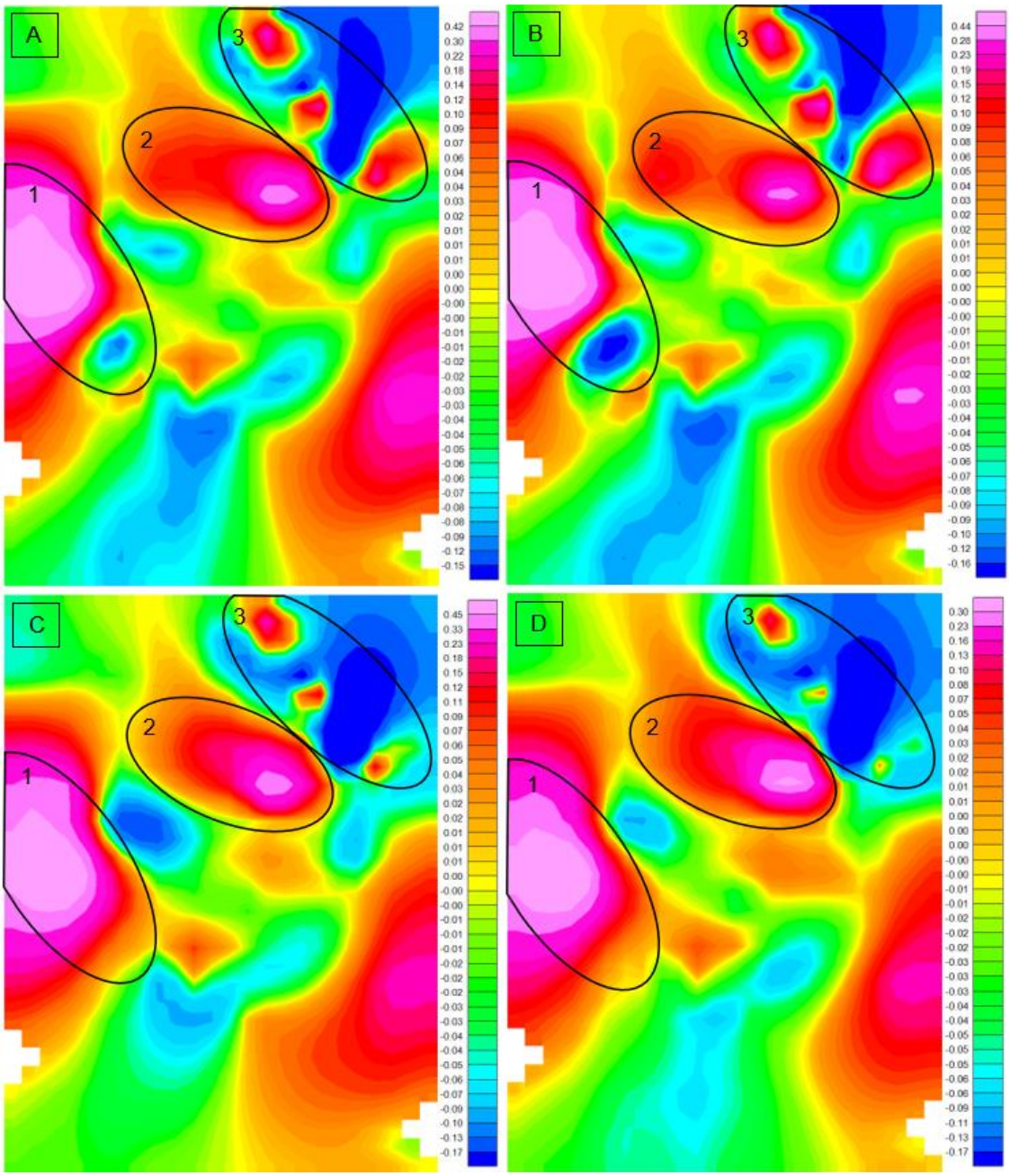

*Figure 76 - Correlation maps between the gravity residual anomaly map and the 4 radiometric maps (**A**: total; **B**: K; **C**: U; **D**: Th).*

All the four correlation maps are similar to each other. In Figure 76 it is possible to see two areas where the correlation between the maps is higher. The area marked with 1, corresponds to the area of lower density and lower concentration values. This is also the location where the gravimetric modelling and inversion hypothesis places the granitic intrusion.

The area marked with 2, corresponds to the area where the lithologies from the CXG and the Middle Ordovician to the Carboniferous occur, which are the embedding rocks of the intrusion. This area has both higher values of density, as well as higher

concentration of K, Th, U and Total, which could indicate that there was an enrichment of these lithologies, due to the presence of the granitic intrusion at depth.

There is also a third area, marked with 3, where it is possible to see the small areas with higher correlation values. These correspond to the location of the Ordovician quartzites, which have lower values of density and lower concentration values, and are more visible in Total, K and U maps, as expected.

9.2 Magnetic and Electromagnetic (VLF)

Both of these methods were carried out on a smaller scale, more focused on the Alto do Sobrido mining area, and both methods have profiles of similar spacing. So, in this chapter a comparison between the three profiles that these methods have in common will be done.

To compare both methods with the three profiles, three figures were created with the sections of all VLF frequencies and a profile for the magnetic residual anomaly values on top of each section. These can be observed in the following figures (Figures 77, 78 and 79).

On VLF profiles 2 and 4 the magnetic profiles do not cover the entire section, so they were placed on their corresponding location.

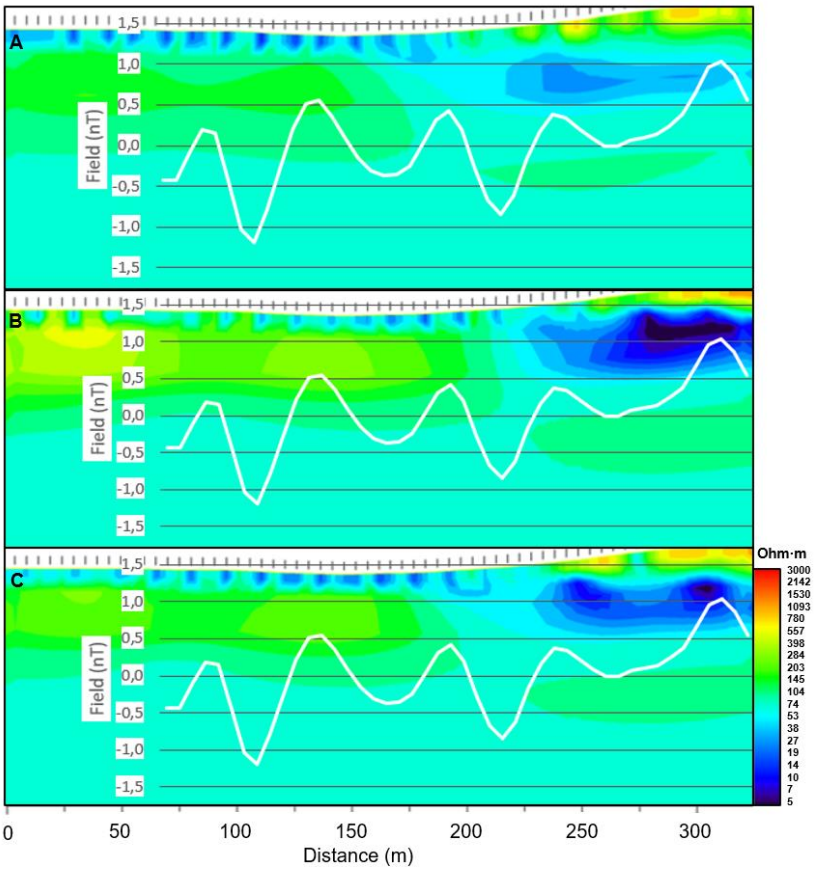

Figure 77 – Sections from VLF's profile 2 (A: 19,2 kHz; B: 22,1 kHz; C: 23,4kHz), with magnetic field profile variations.

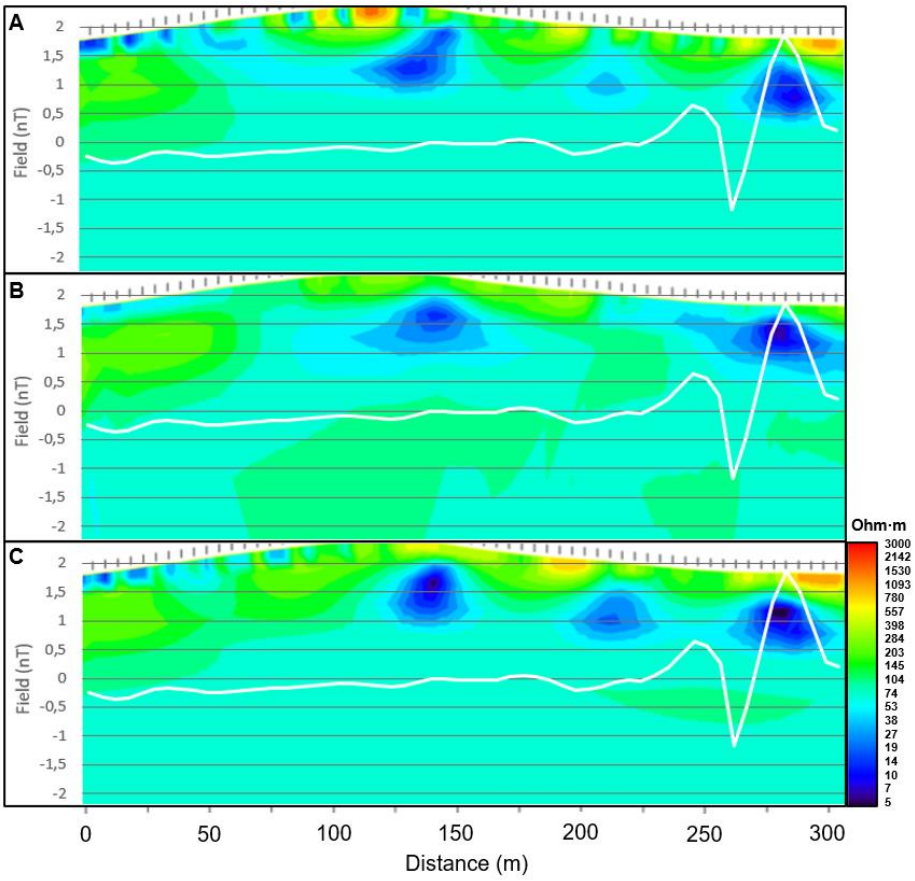

Figure 78 – Sections from VLF's profile 3 (A: 19,2 kHz; B: 22,1 kHz; C: 23,4kHz), with magnetic field profile variations.

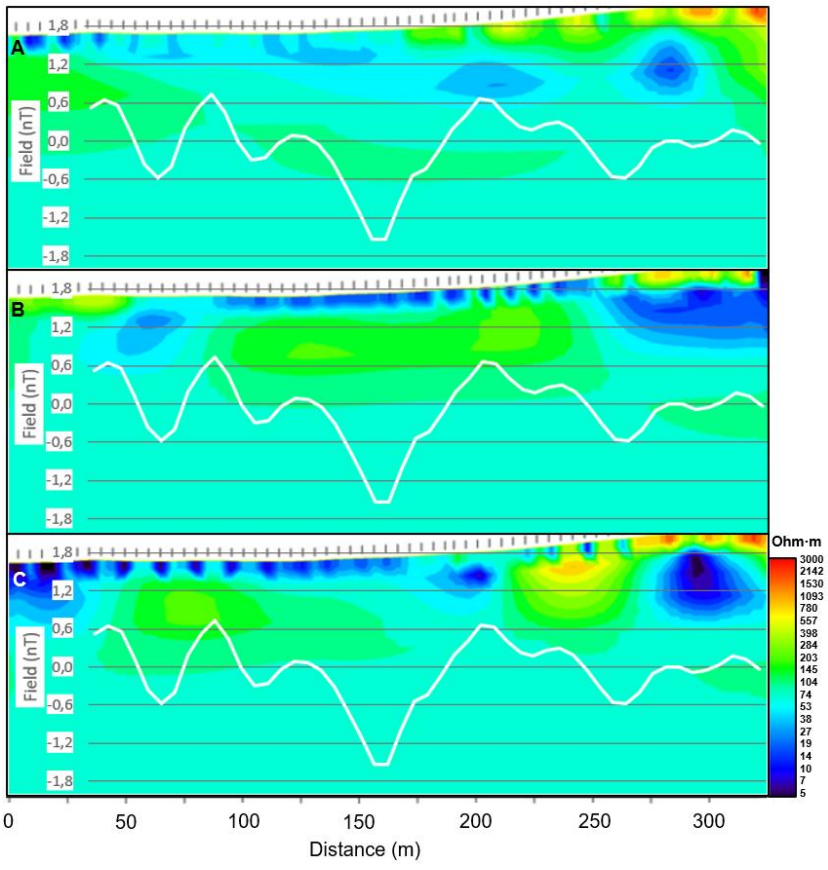

Figure 79 – Sections from VLF's profile 4 (A: 19,2 kHz; B: 22,1 kHz; C: 23,4kHz), with magnetic field profile variations.

The VLF profiles show the location of conductive bodies, up to 40 meters of depth, while the magnetic method may show a sensitivity to a different depth and distance scale. So, the sections of VLF do not always have a correlation to the magnetic method. However, there are some areas on these figures that seem to have some connection between the two methods.

In profile 2 (Figure 77) there is one area of lower resistivity, and in the same location there are two magnetic anomalies. But there are also other magnetic anomalies that do not have a correspondent lower resistivity.

In profile 3 (Figure 78), there is a clear magnetic anomaly on the location of the low resistivity area at the northern edge of the VLF section. But there are two other areas of lower resistivity, that do not show a magnetic anomaly.

In profile 4 (Figure 79), there isn't a clear correlation between the two methods, although there are some small magnetic anomalies on the right side of the sections, where a low resistivity area occurs.

These anomalies that have correlation to low resistivity areas could correspond to the location of mineralized veins, where they could be weathered and have a high decrease in resistivity. They could also correspond to fractured areas, or areas of altered sulphides.

To better analyse these correlations, the sections from the 3 profiles where projected in 3D on top of the magnetic anomaly map (Figure 80).

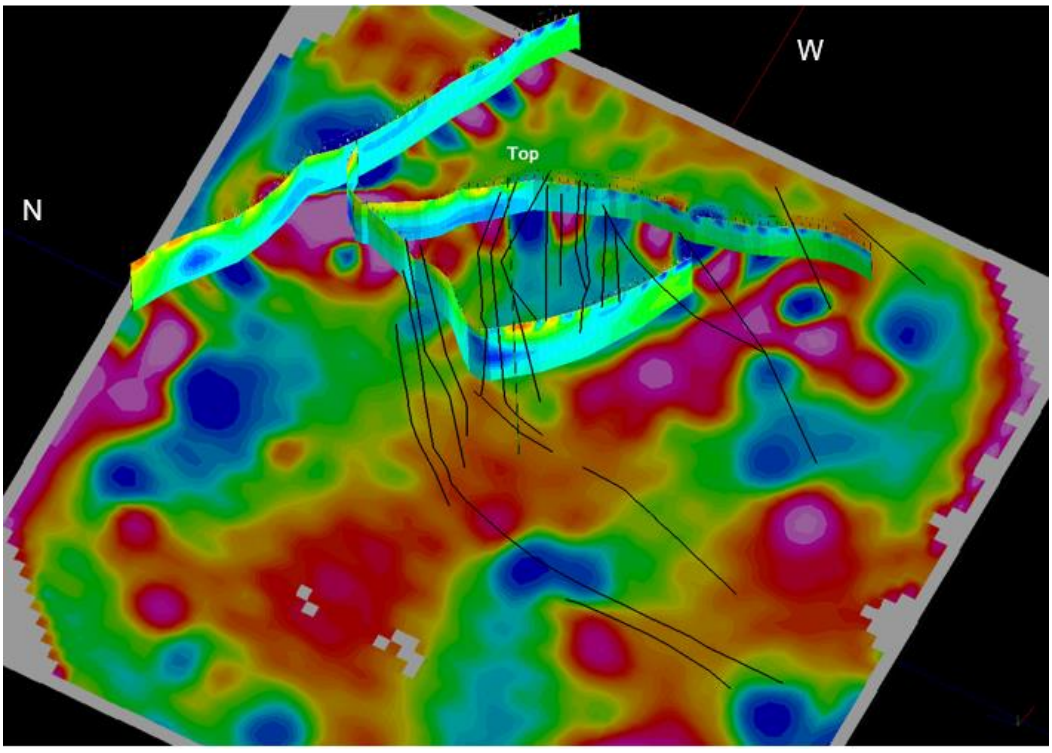

Figure 80 - VLF sections of profiles 2, 3 and 4 projected in 3D on top of the magnetic residual anomaly map, with the location of the mineralized veins (image obtained with Rockworks).

Here it is possible to see that the low resistivity areas in profiles 2 and 3, that were previously said to have an alignment (Figure 55), also appear to have magnetic anomalies associated.

In the northern side of profile 2 occurs an area of lower resistivity, that, as mentioned, could correspond to a mineralized or a dolerite vein that has not been mapped out yet. The magnetic anomalies present there also seem to agree with this hypothesis.

10. Conclusions

The spatial analysis method allowed the identification of areas with higher concentrations of elements, such as Sb, Au, As, Ag, Pb, Zn, W and Sn. The areas with higher concentrations of antimony are Ribeiro da Igreja, Abelheira, Ribeiro da Serra, and Alto do Sobrido. For gold concentrations, the higher values can be found in Ribeiro da Igreja, Ribeiro da Serra, Alto do Sobrido, Banjas, Coiro de Boi and Montalto. Silver, lead, and zinc's highest concentrations can be observed in Terramonte. In Alvarenga and Covas do Rio are the highest concentrations of tungsten and tin, which are areas near granitic sources.

All the geophysical methods used in this work evaluate very different properties. The gravimetric method contributes towards showing differences in densities between lithologies and has a sensitivity towards potentially deeper targets. The electromagnetic VLF method quickly exposes the variations in resistivity of the subsurface, allowing the imaging of structures, weathering zones or mineralizations. The magnetic method shows the sensitivity in the total magnetic field due to the variations in magnetic susceptibility of some of the lithologies surveyed in this area. In this case it grants the ability to find locations with higher concentrations of certain sulphide vein zones, as well as to possibly distinguish the location of previously unmarked veins or structures. The gamma-ray spectrometry method (radiometry) evaluates the concentrations of K, U and Th, which permits the distinction between different lithologies as well as other possible variations within the same lithologies.

The gravity method showed a residual anomaly with areas of lower values (negative anomalies), near the centre of the study area, that possibly occur due to the presence of a non-outcropping granitic mass located at depth, that could possibly be the source of the mineralizations and/or the heat engine that promoted hydrothermal fluid circulation. The created 2D modelling and inversion, that places a granite in the location of the negative anomalies under the lithologies mapped there, with a low associated error, allows this hypothesis to have some geophysical support.

Radiometric surveys are, usually, useful to help differentiate different lithologies, which was the case for the quartzites in this work, where the maps of K, U and Total concentrations show lower values for their location. On all four maps it is also possible to observe a difference in the concentrations between the metamorphic CXG and the metamorphic lithologies from the Middle Ordovician to the Carboniferous.

To try and find a connection between the gravimetric and radiometric method, correlation maps were created. In these maps it is possible to observe two areas of higher correlation values. One of these areas corresponds to the location of the negative

anomalies, where the non-outcropping granite would be located, and to the location of low concentration values of the three isotopes. On the other hand, the second area corresponds to the location of the positive anomalies, where the lithologies from CXG to Carboniferous occur, which are the embedding rocks for the granite, and the location of the higher concentration values.

With the VLF electromagnetic method it was possible to observe several areas of lower resistivity, and consequently higher conductivity, which in some cases corresponds to the locations of the mineralized veins, in other cases corresponds to the location of the DBSZ and surrounding lithologies, which are likely more weathered than the rest and which could contain weathered sulphides.

The magnetic method showed several small anomalies in the location of the old mining works of Alto do Sobrido. These anomalies could occur due to the presence of mineralized veins, diabase/dolerite veins, or due to the presence of faults and fractures associated with the DBSZ.

Comparing the two methods, performed at a smaller scale (magnetic and VLF) in the Alto do Sobrido old mining works, it is possible to observe some correlations between the two, at some locations, while at others the correlation is not observed. There is one clear magnetic anomaly in profile 3, that corresponds to an area of lower resistivity on the VLF sections. This area of lower resistivity also occurs on profile 2, in its northern side, which is where it intersects profile 3. This area occurs within the lithologies of the Carboniferous, and there are no mapped mineralized veins in the area, which could mean that this is an area of higher concentration of weathered sulphides.

10.1 Final Considerations

All the methods could benefit from having a higher spatial sampling density and more widespread measurements, which were not possible in the time that was available for this thesis, due to the pandemic occurring at the moment. Even with all the setbacks, the methods were able to provide some knowledge about the Sb mineralizations, whether it was by, providing geophysical support with gravimetric anomalies to an existing hypothesis, that a non-outcropping granitic rock exists at depth and could be the source for the mineralizations present in the study area, or by being able to locate the mineralizations and structures associated with them, with electromagnetic and magnetic anomalies, or even by distinguishing the area's lithologies, with radiometric anomalies.

Every method has its uses. The gravimetric method is useful in defining lithologies at depth, that are non-outcropping. The radiometric method is a fast execution technique,

that helps with the confirmation of the lithologies present in the area, as well as in distinguishing differences within those same lithologies. The VLF method provides a means of obtaining resistivity information with a quicker and easier acquisition, which allowed the confirmation of the mapped mineralized veins, although in some zones it is prone to interferences from electrical lines. Like the VLF method, the magnetic method also allows the cartography of mineralized veins, as well as structures, but will too be exposed to interferences from electrical lines and metallic structures in the area.

Although there is already a lot of knowledge about the study area, this work was able to provide new geophysical data, with several different methods, that we did not have before. At the same time, we were able to see which methods are of simpler use, such as the magnetic, electromagnetic and radiometry methods, and which require a bit more work to be able to obtain good results, such as the gravity method.

In future it would be of great benefit to the understanding of Sb-Au mineralizations to augment these surveys to larger areas and even to do surveys with other methods, to be able to find a better relation between different techniques that would facilitate the discovery and positioning of these mineralizations. In essence this study contributes towards assessing the applicability of this set of techniques in the specific geographical, geological and topographic context of Northern Portugal and may allow them to be used as a template in other areas of interest.

Bibliographic References

Ajiboye, O. H., 2019. Application of very low frequency (VLF) electromagnetic method to mineral exploration (Mining Geophysics) with case study. University of Ilorin, Department of Applied Geophysics, 34 pp.

Blengini, G. A., Mathieux, F., Nuss, P., 2017. Current circular use of critical raw materials in the EU. In Mathieux, F. (Ed) Critical raw materials and the circular economy, 100 pp. Joint Research Centre (JRC) Science-for-policy report, Publications Office of the European Union, Luxembourg. ISBN 978-92-79-74282-8 ISSN 1831-9424 doi:10.2760/378123.

Costa, J. C., 1950. Notícia sobre uma carta geológica do Buçaco, de Nery Delgado. Comunicação dos Serviços Geológicos de Portugal, 27 pp.

Costa, J. C., Teixeira, C., 1957. Carta Geológica de Portugal na escala 1/50000. Notícia Explicativa da Folha 9-C Porto. Serviços Geológicos de Portugal, Lisbon. 38 pp.

Couto, H., 1993. As Mineralizações de Sb-Au da Região Dúrico-Beirã, 463 pp, University of Porto, Faculty of Science. (PhD Thesis).

Couto, H., 1995. As Mineralizações de Sb-Au da Região Dúrico-Beirã: Controlos das Mineralizações, Hipóteses Genéticas e Relação com Mineralizações de Pb-Zn (Ag) e Sn-W. Museu e Laboratório Mineralógico e Geológico, Memória nº4, pp 541-546. ISSN 0871-1607.

Couto, H., 2013. The Ordovician of Valongo Anticline (Northern Portugal): State of Art. International Multidisciplinary Scientific Geoconference Surveying Geology and Mining Ecology Management, 1, pp 203-208.

Couto, H., 2014. Ouro explorado pelos Romanos em Valongo: controlos das mineralizações auríferas. 1º Congresso Mineração Romana em Valongo. Alto Relevo – Clube de Montanhismo, Câmara Municipal de Valongo. pp 48-57.

Couto, H., Borges, F. S., Roger, G., 2007. Late Palaeozoic orogenic gold-antimony deposits from the Dúrico-Beirã area (North Portugal) and their relation with hidden granitic apexes. Proceedings of the Ninth Biennial SGA Meeting, Dublin. pp 609-612.

Couto, H., Knight, J., Lourenço, A., 2013. Late Ordovician ice-marginal processes and sea-level change from the north Gondwana platform: Evidence from the Valongo Anticline (northern Portugal). Palaeogeography, Palaeoclimatology, Palaeoecology, 375, pp 1-15.

Couto, H., Piçarra, J. M., Gutiérrez-Marco, J. C., 1997. El Paleozoico del Anticlinal de Valongo (Portugal). XIII Jornadas de Paleontología, Reunión Annual de la Sociedad Española de Paleontología. pp 270-290.

Couto, H., Roger, G., Fonteilles, M., 1999. Présence de sills de roches ignées acides dans la mine Sb-Au de Ribeiro da Serra, district Dúrico-Beirão, Nord Portugal. Implications métallogéniques. Comptes Rendus de l'Académie des Sciences - Series IIA - Earth and Planetary Science, Vol 329, Issue 10, pp 713-719. DOI 10.1016/S1251-8050(00)88490-6

Couto, H., Roger, G., Moëlo, Y., Bril, H., 1990. Le district à antimoine-or Dúrico-Beirão (Portugal): évolution paragénétique et géochimique; implications métallogéniques. Mineralium Deposita, Berlin, 25, Suppl: 69-81.

Cruz, C., 2020. Post-tectonic Variscan magmatism from northwest Iberia. Implications for W-Mo metallogeny. Case study of Lamas de Olo Pluton. Departamento de Geociências, Ambiente e Ordenamento do Território, Universidade do Porto. 327pp.

Defense Mapping Agency, 1987. Supplement to Department of Defense World Geodetic System 1984 Technical Report: Part I - Methods, Techniques, and Data Used in WGS 84 Development. 410 pp. United States Naval Observatory, Washington, DC.

Dentith, M., Mudge, S., 2014. Geophysics for the Mineral Exploration Geoscientist. 438 pp. Cambridge University Press, United Kingdom.

European Commission, 2014. Report on Critical Raw Materials for the EU: Critical Raw Materials Profiles. 202 pp.

European Commission, 2017. Communication from the Commission to the European Parliament, the Council, The European Economic and Social Committee and the Committee of the Regions on the 2017 list of Critical Raw Materials for the EU, 8pp. Brussels.

Grund, S. C., Hanusch, K., Breunig, H. J., Wolf, H. U., 2006. Ullmann's Encyclopedia of Industrial Chemistry: Antimony and Antimony Compounds. Volume 4, pp 12-42. Wiley-VCH Verlag GmbH & Co. KGaA, Weinheim, Germany.

Gumiel, P., 1983. Metalogenia de los yacimientos de antimonio de la Peninsula Iberica. Revistaa Española de Geología e Minería, Vol. 54, pp 6-120.

Gumiel, P., Arribas, A., 1987. Antimony Deposits in the Iberian Peninsula. Economic Geology, Volume 82, pp 1453-1463.

Jesus, A. P., 2003. Evolução sedimentar e tectónica da Bacia Carbonífera do Douro (Estefaniano C inferior, NW de Portugal). Cadernos Lab. Xeolóxico de Laxe, Vol. 28, 107-125 pp. ISSN: 0213- 4497.

Julivert, M., Fontboté, J. M., Ribeiro, A., Conde, L., 1974. Memória Explicativa del Mapa Tectónico de la Península Ibérica y Baleares. Intituto Geologico y Minero de España, Madrid, 113pp.

Kearey, P., Brooks, M., Hill, I., 2002. An Introduction to Geophysical Exploration. 3rd Ed., 262 pp. Blackwell Science Ltd., Oxford.

Kernow Mining Portugal, 2009. Contracto de Prospecção e Pesquisa de Antimónio, Ouro, Prata, Cobre, Chumbo, Zinco e Pirites, Sobrido, 5º Relatório de Actividades. Kernow Mining Portugal, Soc. Unip. Lda, 40 pp.

Kernow Mining Portugal, 2010. Contracto de Prospecção e Pesquisa de Antimónio, Ouro, Prata, Cobre, Chumbo, Zinco e Pirites, Sobrido, Relatório Final. Kernow Mining Portugal, Soc. Unip. Lda, 27 pp.

Klochko, K., 2019. Antimony *in* Mineral Commodity Summaries. United States Geological Survey. pp 22-23.

Llewellyn, T. O., 1992. Antimony *in* Minerals Yearbook, Volume 1: Metals and Minerals. United States Department of the Interior, Bureau of Mines, pp 223-234.

Machadinho, A., 2014. Modelação da geometria de rochas granitóides recorrendo a métodos geofísicos gravimétricos e magnéticos: uma contribuição para a avaliação do potencial geotérmico na região centro de Portugal. Departamento de Ciências da Terra da Faculdade de Ciências e Tecnologia, Universidade de Coimbra. 312 pp.

Medeiros, A. C., 1964. Carta Geológica de Portugal na escala 1/50000. Notícia Explicativa da Folha 13-B Castelo de Paiva. Serviços Geológicos de Portugal, Lisbon. 61 pp.

Medeiros, A. C., Pereira, E., Moreira, A., 1980. Carta Geológica de Portugal na escala 1/50000. Notícia Explicativa da Folha 9-D Penafiel. Serviços Geológicos de Portugal, Lisbon. 46 pp.

Medina, J., 1996. Contribuição para o conhecimento da geologia do Grupo das Beiras (CXG) na região do Caramulo-Buçaco (Portugal Central). Aveiro University, 202 pp. (PhD Thesis).

Milsom, J., 2003. Field Geophysics. 3rd Ed., 232 pp. John Wiley & Sons Ltd., West Sussex.

Milsom, J., Eriksen, A., 2011. Field Geophysics. 4th Ed., 287 pp. John Wiley & Sons Ltd., West Sussex.

Moreira, J.R.S., 2001. O trabalho de campo em Geologia com alunos do 11º ano - uma proposta inovadora de construção de materiais à aprendizagem dos alunos (Um estudo na área de Valongo): Dissertação para obtenção do grau de mestre em Geologia para o ensino. Vol.1. University of Porto, Faculty of Sciences, Geology Department, 211 pp. (Master's Thesis).

Moskowitz, B. M., Jackson, M., Chandler, V., 2015. Geophysical Properties of the Near-Surface Earth: Magnetic Properties. Treatise on Geophysics, Second Edition. Vol. 11, pp 139-174.

Moura, A. & Velho, J. L., 2012. Recursos Geológicos de Portugal. Volume 57, 1ªEd, pp 17-24. Palimage, Coimbra, Portugal.

Neiva, A., András, P., Ramos, J., 2008. Antimony quartz and antimony-gold veins from northern Portugal. Ore Geology Reviews, 34, pp 533-546.

Parra, A., Filipe, A., 1997. Ocorrências Auro-Antimoníferas do Alto do Sobrido. Instituto Geológico e Mineiro, Lisboa, 68 pp.

Ramos, J. M. F., 1997. Mineralizações Auro-Antimoníferas em Quartzitos Brechificados e Brechas Quartzo-ferruginosas da Área de Alto do Sobrido (Primeiros Resultados). Instituto Geológico e Mineiro, Lisboa, 48 pp.

Ribeiro, A., Pereira, E., 1992. Tectónica *in* Pereira, E. (coordinator), Carta Geológica de Portugal na escala 1/200 000 – Notícia Explicativa da Folha 1. Serviços Geológicos de Portugal, Lisbon. pp 51-56.

Ribeiro, R., 2017. Gravimetric Modelling and Geological Interpretation of Argemela-Panasqueira Area. Departamento de Geociências, Ambiente e Ordenamento do Território, Universidade do Porto. 81pp.

Sousa, M. B., Sequeira, A. J. D., 1989. Carta Geológica de Portugal à escala 1/50 000 – Notícia Explicativa da folha 10-D Alijó. Serviços Geológicos de Portugal, Lisbon, 59 pp.

Teixeira, C., 1955. Notas sobre a Geologia de Portugal: o Complexo Xisto-Grauváquico ante-Ordoviciano. Empresa Literária Fluminense, Lisbon, 50 pp.

Teixeira, C., Medeiros, A. C., 1965. Carta Geológica de Portugal na escala 1/50000. Notícia Explicativa da Folha 9-A Póvoa de Varzim. Serviços Geológicos de Portugal, Lisbon. 50 pp.

Thébault, E., Finlay, C. C., Beggan, C. D., Alken, P., Aubert, J., Barrois, O., Bertrand, F., Bondar, T., Boness, A., Brocco, L., Canet, E., Chambodut, A., Chulliat, A., Coïsson, P., Civet, F., Du, A., Fournier, A., Fratter, I., Gillet, N., Hamilton, B., Hamoudi, M., Hulot, G., Jager, T., Korte, M., Kuang, W., Lalanne, X., Langlais, B., Léger, J., Lesur, V., Lowes, F. J., Macmillan, S., Mandea, M., Manoj, C., Maus, S., Olsen, N., Petrov, V., Ridley, V., Rother, M., Sabaka, T. J., Saturnino, D., Schachtschneider, R., Sirol, O., Tangborn, A., Thomson, A., Tøffner-Clausen, L., Vigneron, P., Wardinski, I., Zvereva, T., 2015. International Geomagnetic Reference Field: the 12th generation. Earth, Planets and Space, 67:79, 19 pp. DOI 10.1186/s40623-015-0228-9

Vallance, J., Cathelineau, M., Boiron, M. C., Fourcade, S., Shepherd, T. J., Naden, J., 2003. Fluid-rock interactions and the role of late Hercynian aplite intrusion in the genesis of the Castromil gold deposit, northern Portugal. Chemical Geology, 194: 201-224.

Zhang, Z., 2015. The Geophysical Very Low Frequency Electromagnetic (VLF-EM) Method: Effects of Topography and Surface Water Investigated with Simulations and Field Measurements. University of Saskatchewan, Department of Geological Sciences, 128 pp. (Master's Thesis).

Appendix

Appendix 1 – Gravity Values

Table A – Complete Bouguer Anomaly values of every station from the gravity survey, and their coordinates and elevation (Datum: ETRS89 Portugal TM06; EPSG:3763).

Station	Height	Longitude	Latitude	Bouguer Anomaly (mGal)
1	139,52	-24098,36	156999,00	13,8268
2	140,86	-23962,95	157760,95	14,4358
3	158,23	-23613,82	157644,34	13,9220
4	149,15	-23441,72	156969,92	13,6109
5	126,84	-24204,12	156055,14	13,4605
6	178,57	-25186,93	157834,70	15,4033
7	74,83	-27202,93	155970,23	16,0063
8	95,50	-26487,38	155969,44	15,8573
9	32,73	-23197,08	156167,49	12,7109
10	24,34	-22310,50	154060,72	11,0843
11	23,23	-26479,99	154803,57	15,3074
12	73,18	-26870,67	155050,13	15,4435
13	98,65	-24412,33	154312,24	13,0468
14	156,43	-24546,29	154974,78	12,8876
15	96,97	-25473,59	154558,61	14,7272
16	131,76	-25201,57	155842,96	14,5792
17	132,92	-24855,40	156087,13	13,8703
18	168,62	-25593,29	156709,23	15,2682
19	191,04	-25793,30	156969,94	15,3644
20	121,62	-26054,34	156767,73	15,9151
21	85,48	-26987,82	157038,32	16,5351
22	130,06	-27157,54	157820,00	17,3583
23	132,43	-24599,90	155588,54	13,6808
24	127,77	-24820,31	155852,44	13,8094
25	128,26	-24994,18	155801,70	14,0860
26	121,53	-25278,46	155744,83	14,3947
27	111,79	-25383,84	155609,57	14,4692
28	99,44	-25436,39	155761,01	14,7725
29	103,69	-25368,21	155881,16	14,7817
30	114,97	-25379,29	156075,62	14,8768
31	141,24	-25241,81	156013,41	14,5634
32	154,32	-25167,93	156175,49	14,4959
33	164,07	-25029,35	156252,56	14,5360
34	146,01	-24878,87	156183,56	13,9938
35	137,18	-24727,83	156063,61	13,6625
36	164,83	-24939,27	156029,22	13,9202
37	197,49	-25066,29	156122,22	14,2049
38	186,85	-24903,38	156383,19	14,4994
39	208,29	-24588,40	156268,02	13,7710
40	237,58	-24757,52	156458,78	13,6122
41	252,35	-24911,61	156697,67	14,0645
42	89,04	-25113,79	155424,52	14,5250
43	65,22	-25544,17	155582,87	15,1101
44	116,93	-25735,49	155701,04	14,5655
45	133,20	-25790,40	155964,54	14,6970
46	147,10	-25829,97	156303,30	15,0648
47	148,06	-25286,96	156492,63	14,8741
48	125,67	-25563,48	156479,82	15,1513
49	98,11	-25579,38	156159,90	15,5010
50	79,35	-25618,90	155759,51	14,6884

Appendix 2 – Electromagnetic Values

Table B – Values obtained from the electromagnetic survey of in-phase and quadrature for every frequency (19,2 kHz, 22,1 kHz, and 23,4 kHz) and the coordinates of all stations (Datum: ETRS89 Portugal TM06 EPSG:3763).

Profile nº	Longitude	Latitude	In-phase 19,2	Quad 19,2	In-phase 22,1	Quad 22,1	In-phase 23,4	Quad 23,4
1	-24823,97	155900,26	-15,5	-3,3	-18,8	-8,1	-9,6	-4,5
1	-24820,90	155904,20	-9,6	-3,3	-14,2	-8,2	-9,3	-5,1
1	-24819,91	155908,79	-6	-2,4	-9,6	-8,1	-4,9	-5,1
1	-24820,27	155913,77	-1,7	-2,8	-4,9	-8,5	-1	-5,5
1	-24821,37	155918,63	-1,6	-2,9	-4,7	-8,6	-1	-5,3
1	-24822,80	155923,42	-3,4	-2,3	-5,9	-8,6	-2,6	-4,7
1	-24824,23	155928,21	-3,6	-2,4	-6	-8,4	-1,5	-5
1	-24825,92	155932,92	-1,6	-2,1	-2,9	-8,4	-0,2	-4,9
1	-24827,74	155937,57	-1	-2,7	-1,7	-8,8	0,2	-5,1
1	-24829,58	155942,23	-0,4	-2,5	-0,6	-8,8	0,9	-5,6
1	-24831,40	155946,88	-3,2	-2,3	-3,8	-8,3	-1,3	-4,9
1	-24833,24	155951,54	-3,8	-2,1	-3,7	-8,3	-2,6	-4,9
1	-24834,54	155956,36	-4,9	-2,6	-3,6	-8,4	-3	-5,2
1	-24835,74	155961,22	-8,1	-1,9	-5,7	-8,2	-5,2	-4,9
1	-24836,94	155966,07	-6	-2	-4	-8,2	-3,8	-4,7
1	-24837,74	155971,00	-5	-2,3	-2,3	-8	-2,8	-4,5
1	-24838,33	155975,97	-6,2	-2,1	-3,1	-8	-4	-4,4
1	-24838,92	155980,94	-3,9	-2	0,8	-7,6	-0,6	-4,7
1	-24839,69	155985,88	-5,7	-1,9	-0,6	-7,4	-2,8	-4
1	-24840,51	155990,81	-6,4	-1,7	-0,2	-7	-3,1	-3,8
1	-24841,32	155995,75	-7,4	-2	-0,3	-6,6	-3,7	-3,8
1	-24842,53	156000,59	-3,1	-2,5	5,8	-7,4	1,3	-4,4
1	-24843,90	156005,41	-2,1	-2,7	6,5	-7,4	1,3	-4,4
1	-24845,76	156010,01	-2,3	-2,8	7,7	-7,3	1,5	-4,4
1	-24848,18	156014,38	-3,7	-2,5	7,9	-6,7	1,4	-3,9
1	-24848,99	156019,17	-7,6	-1,5	2,5	-5,2	-3,2	-3
1	-24848,94	156024,17	-8,2	-1,6	3,1	-5,4	-4,1	-3,1
1	-24848,28	156029,08	-11,3	-2,8	1,3	-5	-6,7	-2,7
1	-24846,80	156033,86	-11,7	-3,1	1,1	-5,6	-7,1	-3,3
1	-24844,62	156038,00	-22,1	-2,6	-5	-5,9	-16,1	-2,7
1	-24839,98	156039,87	-25,8	-1,7	-6,9	-7,2	-19,5	-2,1
1	-24836,06	156041,46	-25,4	-1,2	-7,2	-7,9	-19,5	-2,5
2	-24798,48	155879,71	-7,1	-4,5	-13,4	-8,8	-6,6	-6,1
2	-24797,77	155884,67	-5,9	-4,1	-12,2	-9,1	-5,9	-5,8
2	-24797,06	155889,61	-6,1	-3,8	-11,4	-9,2	-6	-5,5
2	-24797,13	155894,61	-4,7	-3,1	-8,2	-9,3	-3,6	-5,8
2	-24797,21	155899,62	-3,4	-3,2	-6,9	-9,3	-2,6	-5,7
2	-24797,59	155904,58	-1,9	-3,2	-3,6	-9,1	-0,6	-5,3
2	-24798,56	155909,50	-2,2	-2,7	-3,1	-8,5	-0,3	-5,2
2	-24799,78	155914,33	-2,2	-2,8	-2,6	-8,8	-0,3	-5,2
2	-24801,42	155919,06	0,7	-2,6	0,9	-8,2	2,1	-4,9
2	-24803,05	155923,79	1,3	-2,4	1,9	-8,5	3,1	-5
2	-24804,96	155928,40	1	-2,1	1,9	-8	3,1	-4,6
2	-24807,18	155932,88	0,3	-1,9	1,4	-8	1,9	-4,4
2	-24809,41	155937,35	0	-2,2	2,3	-8,3	2,6	-4,7
2	-24811,63	155941,84	0,6	-2	2,6	-7,9	2,4	-4,7
2	-24813,48	155946,48	-0,6	-2,3	1,9	-7,6	1,4	-4,9
2	-24815,12	155951,20	-1,3	-2,4	2	-7,6	1,1	-4,8
2	-24816,77	155955,93	-1,5	-2,2	2,3	-7,7	0,9	-4,9
2	-24817,99	155960,77	-2,5	-1,8	2,3	-7,1	0,3	-4,3
2	-24819,17	155965,63	-1,9	-2	3,5	-7,1	1	-4,2
2	-24820,36	155970,49	-2,4	-2	3,6	-6,8	0,3	-4,2

Table B – Values obtained from the electromagnetic survey of in-phase and quadrature for every frequency (19,2 kHz, 22,1 kHz, and 23,4 kHz) and the coordinates of all stations (Datum: ETRS89 Portugal TM06 EPSG:3763) (Continuation).

Profile nº	Longitude	Latitude	In-phase 19,2	Quad 19,2	In-phase 22,1	Quad 22,1	In-phase 23,4	Quad 23,4
2	-24821,59	155975,34	-2,7	-2	4,1	-7	0,8	-4
2	-24823,00	155980,14	-2,2	-2,2	5	-7,1	0,9	-4,3
2	-24824,41	155984,93	-3,5	-2	4,8	-6,9	0,7	-4,2
2	-24824,84	155989,87	-6	-1,6	3,8	-6,7	-0,9	-3,8
2	-24824,79	155994,87	-5,6	-1,6	4,4	-6,2	-1,4	-3,5
2	-24824,74	155999,87	-6,8	-1,6	4,7	-5,9	-2,3	-3,5
2	-24824,69	156004,88	-7,2	-2	5,1	-6	-2,3	-3,6
2	-24825,70	156009,89	-8,3	-2	5,2	-6,1	-2,1	-3,9
2	-24825,65	156014,89	-6,9	-2,8	6,7	-6,5	-1,6	-4,4
2	-24826,53	156019,77	-4,7	-3	8,3	-7,5	0,1	-5,1
2	-24827,90	156024,58	-3,6	-2,7	9,3	-8,1	0,9	-5
2	-24829,26	156029,39	-3,4	-2,3	9,5	-8,6	1,9	-4,7
2	-24831,08	156034,04	-3,3	-1,8	8,2	-9	0,7	-4,6
2	-24832,09	156038,57	-4,6	-2	7,2	-9,7	0	-4,9
2	-24834,18	156043,13	-4,8	-2	5,7	-10,2	-0,6	-5
2	-24836,24	156047,68	-4,8	-2,2	5,5	-11,1	-0,9	-5,7
2	-24838,06	156052,34	-5,9	-2,2	3,2	-11,1	-2,3	-5,4
2	-24839,86	156057,01	-5,9	-2,5	3,2	-12	-2,5	-5,8
2	-24841,68	156061,67	-6,3	-2,7	3,3	-12,3	-2,7	-6,4
2	-24843,48	156066,33	-6,3	-2,8	2,8	-12,6	-3,1	-6,5
2	-24845,33	156070,98	-4	-2,3	3,2	-12,1	-1,7	-5,9
2	-24847,30	156075,58	-3	-2	5,9	-11,9	-0,2	-5,5
2	-24849,28	156080,17	-2,8	-1,3	5,7	-11,5	0,4	-5,2
2	-24852,33	156084,06	-1,5	-2,1	7,1	-11,7	1,4	-5,6
2	-24855,72	156087,74	-1,4	-2,1	7,2	-11,7	2	-5,8
2	-24859,12	156091,41	0	-2,3	7,6	-12,3	2,2	-6,1
2	-24862,51	156095,09	-0,9	2,7	7,5	-12,6	3,1	-6,3
2	-24865,90	156098,78	-0,5	-3	6,5	-13	2,5	-6,9
2	-24868,98	156102,71	-0,1	-3,6	6,7	-12,8	2,1	-7,4
2	-24872,07	156106,64	-0,2	4	7	-13,1	2,5	-7,4
2	-24875,15	156110,58	0	3,6	7,1	-12,7	2,5	-7,1
2	-24878,50	156114,23	-0,9	3	9,2	-12	4	-6,6
2	-24882,76	156116,86	-2	2,5	11	-11,6	-5,7	6,1
2	-24887,01	156119,48	-2,7	2,5	11,6	-11,9	-6,3	5,9
2	-24890,94	156122,48	-1,3	2,3	9,6	-12,2	4,5	-5,8
2	-24894,08	156126,38	-0,2	-2	6,4	-11,8	3,1	-6
2	-24897,22	156130,28	-1,6	-2,6	2,8	-12,2	0,5	-5,9
2	-24899,88	156134,51	-1,6	-2,9	2,3	-11,9	-0,7	-6,1
2	-24902,49	156138,78	0	-2,8	4,3	-12,2	1,3	-6,4
2	-24905,10	156143,04	-0,4	-2,9	4,3	-12	1,2	-6,1
2	-24907,85	156147,21	0	-3	5,6	-12	1,7	-6,5
2	-24910,65	156151,36	-0,5	-3,3	4,8	-11,3	1,4	-6,5
2	-24913,27	156155,61	-0,5	-3,6	5,1	-11,7	1,1	-6,6
2	-24915,68	156160,00	-0,6	-3,8	6	-11,4	1,8	-6,9
2	-24916,21	156165,18	-7,6	-3,3	-3,4	-9,7	-6,5	-5,2
3	-24853,51	155971,11	-0,9	2,6	4	-9,2	-3,3	5,7
3	-24858,03	155973,23	-2,1	2,5	4,6	-9,5	-3,5	5,6
3	-24862,56	155975,36	-1,6	2,7	3,3	-9,3	-2,3	5,6
3	-24867,09	155977,49	-0,1	2,1	0,8	-8,8	1,2	-5,5
3	-24871,61	155979,60	-0,4	2,3	1,8	-9	-1,5	5,2
3	-24876,15	155981,73	-1,1	2,6	3,2	-9,2	-2,3	5,4
3	-24880,68	155983,85	-0,7	3	2,4	-9	-2,1	5,8
3	-24885,21	155985,98	-0,1	2,9	1,7	-9,3	-1	5,7
3	-24889,73	155988,10	0,5	3,1	0,8	-9,4	-1	5,8

Table B – Values obtained from the electromagnetic survey of in-phase and quadrature for every frequency (19,2 kHz, 22,1 kHz, and 23,4 kHz) and the coordinates of all stations (Datum: ETRS89 Portugal TM06 EPSG:3763) (Continuation).

Profile nº	Longitude	Latitude	In-phase 19,2	Quad 19,2	In-phase 22,1	Quad 22,1	In-phase 23,4	Quad 23,4
3	-24894,01	155990,69	0,2	3	0,6	-9,4	0	6
3	-24898,25	155993,34	0,2	3,1	0,4	-9,1	0	6
3	-24902,49	155996,00	0,4	3	0,2	-9,3	0	5,9
3	-24906,72	155998,66	2	3,4	-0,9	-9,1	0,6	6,2
3	-24910,96	156001,32	0,9	3,4	1,1	-9,2	-0,7	6,2
3	-24915,19	156003,97	0,8	3,3	-0,4	-9,2	0,2	6
3	-24919,44	156006,64	1,4	3,4	-1,1	-9,1	0,5	6,4
3	-24923,33	156009,75	1,2	3,1	-1,4	-9,1	-1	-5,8
3	-24927,05	156013,10	2	3,6	-2,7	-9	-1,8	-5,8
3	-24930,75	156016,44	-3,5	-3	-8	-8	-4,6	-5,4
3	-24934,47	156019,80	-3,5	-3,3	-2,9	-8,4	-2,9	-5,5
3	-24938,18	156023,15	1,9	3,3	-1,1	-7,9	-1,2	-5,8
3	-24941,73	156026,66	-3,9	-3,3	-4,6	-8,1	-3,5	-5,5
3	-24944,85	156030,57	-3,5	-3,2	-3,2	-7,6	-3,6	-5
3	-24947,96	156034,48	2,8	3,4	-1,9	-7,7	-2,3	-5,5
3	-24951,08	156038,40	2,3	3,9	-1,8	-8	-2,3	-5,8
3	-24954,20	156042,31	2,8	4,5	-2	-8,5	-2,8	-6,4
3	-24957,32	156046,22	2,9	4,7	-2	-9	-2,5	-6,8
3	-24960,43	156050,13	-4,6	-4,3	-4,1	-8,6	-5	-6,2
3	-24962,02	156054,62	-8,8	-3,8	-9,5	-8,4	-9,4	-5,5
3	-24962,26	156059,62	-13,5	-4,4	-13,8	-7,3	-13,3	-5,3
3	-24961,22	156064,18	-15,8	-4	-15,9	-7,7	-15,8	-4,8
3	-24958,00	156068,01	-21,7	-3,3	-19,2	-6,8	-20,4	-3,7
3	-24954,78	156071,84	-23,6	-2,9	-20,3	-6,1	-22,2	-2,9
3	-24951,38	156075,49	-21,5	-2,7	-18,1	-5,9	-20,5	-2,6
3	-24947,83	156079,02	-23,2	-2,1	-17,6	-4,8	-21,4	-1,8
3	-24944,28	156082,55	-21,5	-2	-16,8	-4,6	-19,5	-1,9
3	-24940,74	156086,07	-21,9	-1,8	-14,9	-4,4	-19,4	-1,7
3	-24937,71	156089,97	-19,4	-2	-12	-4	-16,8	-1,8
3	-24935,63	156094,52	-15,2	-1,8	-8	-3,7	-12,5	-1,6
3	-24934,04	156099,18	-11,3	-0,1	-1,8	-3,2	-7,5	-0,8
3	-24933,79	156104,18	-6,9	0,7	2,7	-2,3	-3,9	0,2
3	-24933,72	156109,16	-7,4	0,9	4,2	-0,4	-3,4	1,1
3	-24934,45	156114,11	-15,5	0,9	-2,4	0	-11,5	2,1
3	-24932,00	156118,20	-16,6	0,5	-2,4	0	-11,5	1,8
3	-24928,86	156122,09	-15,8	0	-1,6	-1,2	-11,5	0,8
3	-24925,72	156125,98	-16,7	-1	-2,4	-4	-11,9	-1,1
3	-24923,61	156130,46	-15	-2,2	-2,8	-6,9	-11	-3
3	-24921,83	156135,15	-14,3	-2,5	-3,8	-9,4	-13,2	-4
3	-24920,06	156139,82	-11,6	-2,8	-3,9	-10,9	-10,2	-5,3
3	-24918,38	156144,53	-13,5	-2,9	-6	-11,9	-11,1	-5,5
3	-24916,74	156149,25	-12,8	-3	-6,3	-11,8	-10,3	-6
3	-24915,10	156153,98	-12,4	-3,3	-6,6	-11,7	-11,2	-6
3	-24913,46	156158,70	-14,2	-3,2	-8	-11,2	-12,7	-5,7
3	-24911,70	156163,39	-10,3	-3,2	-4,5	-10	-7,5	-5,9
3	-24909,91	156168,06	-10,2	-2,8	-5,8	-9	-8,7	-4,4
3	-24908,12	156172,73	-11,7	-1,5	-10,9	-9	-12,5	-3,8
3	-24904,47	156175,69	-19,2	-0,7	-16,6	-9,1	-19,1	-2,1
3	-24900,00	156177,93	-21,4	-0,6	-17,8	-7	-21,3	-1,2
3	-24895,54	156180,21	-23,7	-0,7	-19,4	-5,5	-22,5	-0,7
3	-24890,74	156181,09	-24,6	-0,5	-18,9	-4	-23,8	-0,1
3	-24885,74	156181,16	-24,6	0,3	-17,9	-3	-23,1	0,9
3	-24880,74	156181,12	-23,6	1	-16,9	-1,6	-22,1	2,1
4	-24741,79	156105,89	-17,4	5	25,9	-3,3	20,6	-5,8

Table B – Values obtained from the electromagnetic survey of in-phase and quadrature for every frequency (19,2 kHz, 22,1 kHz, and 23,4 kHz) and the coordinates of all stations (Datum: ETRS89 Portugal TM06 EPSG:3763) (Continuation).

Profile nº	Longitude	Latitude	In-phase 19,2	Quad 19,2	In-phase 22,1	Quad 22,1	In-phase 23,4	Quad 23,4
4	-24745,32	156109,43	-13,8	6,8	21,7	-5,9	16,5	-7,5
4	-24748,95	156112,86	-12,1	6,3	21,1	-6,4	15,4	-7,2
4	-24752,95	156115,87	-12,6	4,6	21,4	-6,2	15,5	-5,9
4	-24756,95	156118,87	-11,2	4,4	19,9	-7,1	-14,2	6,2
4	-24761,05	156121,73	-11,1	4,4	21,7	-8,2	-15,5	6,8
4	-24765,18	156124,57	-11	4,4	20,8	-7,6	-14,7	6,8
4	-24769,37	156127,28	-11,2	3,3	22,6	-5,7	-15,4	5,3
4	-24773,88	156129,34	-11,1	1,9	22,6	-3,5	-16	3,7
4	-24778,68	156130,72	-11,3	0,6	22,9	-1,5	-15,8	2,1
4	-24783,49	156132,10	-10	0,2	23	-0,3	-14,6	0,8
4	-24788,04	156134,15	-7,7	0,8	20,5	-0,6	-12,6	1,1
4	-24792,51	156136,39	-5,5	1,5	18,1	-1,7	-10,2	2,4
4	-24796,92	156138,75	-3,5	2	15,3	-2,2	-8,3	2,9
4	-24801,34	156141,10	-2,6	1,9	13,1	-1,9	-6	2,6
4	-24805,60	156143,72	-2,4	1,1	12,5	-1,2	-6,3	1,8
4	-24809,82	156146,39	-2,8	0,5	12,6	-1,2	-6,9	0,9
4	-24814,06	156149,06	-2,8	0,3	13,4	-1,1	-7,1	0,9
4	-24818,40	156151,52	-2,1	0,3	12,8	-0,6	-5,9	0,8
4	-24822,91	156153,66	-1	0,7	12,4	-0,8	-4,8	1,1
4	-24827,44	156155,81	0,2	1,3	10,7	-1,2	-3,1	1,3
4	-24831,96	156157,95	1,1	1,6	9,6	-1,1	-2,3	1,6
4	-24836,48	156160,10	1,2	1,3	8,5	-1,9	-2,1	1,3
4	-24841,00	156162,25	0,1	0,7	9,1	-1,3	-3,7	1,2
4	-24845,51	156164,39	-0,8	1	9,6	-2	-4,1	1,4
4	-24850,03	156166,54	-1,4	0,9	9,5	-2,3	-4,5	1,7
4	-24854,45	156168,88	-2,4	0,7	9,3	-2,2	-4,9	1,4
4	-24858,78	156171,36	-3	0,9	9,8	-2,5	-5,4	1,8
4	-24863,13	156173,83	-3,8	1,2	9,2	-2,6	-5,9	1,7
4	-24867,48	156176,31	-3,9	1,4	8,3	-2,7	-5,6	2,6
4	-24871,77	156178,88	-4,6	1	7	-2,7	-6,2	2,2
4	-24875,97	156181,59	-5,5	0,1	5,1	-1,9	-5,9	1,4
4	-24880,17	156184,30	-6,4	-0,3	5,3	-1,8	-7,1	1
4	-24884,38	156187,02	-7,8	-0,7	5,2	-2,5	-8,4	1
4	-24888,57	156189,73	-8	-0,6	4,5	-1,7	-7,4	1,2
4	-24892,21	156193,15	-6,4	0,3	2,1	-2,8	-5,5	1,9
4	-24895,75	156196,68	-4,3	1,6	0,6	-2,6	3,3	-2,7
4	-24899,28	156200,22	-3,4	2,4	0	-3,4	-2	4,1
4	-24903,01	156203,42	-2	3,7	-0,7	-4,6	-0,9	5,4
4	-24907,85	156204,72	-2,1	3,9	0,3	-6	-1,3	5,2
4	-24912,74	156205,71	-2	1,8	-2,5	7,1	-2,7	5,1
4	-24917,70	156206,34	-2,7	1,5	-4,1	7	-3,2	5
4	-24922,67	156206,96	-1,5	1,7	-3,1	7,5	-2,5	5,4
4	-24927,53	156208,08	-1,1	5,3	2,9	-8	-1,4	6,7
4	-24932,34	156209,44	0,4	6,7	2	-8,8	0,1	7,6
4	-24937,16	156210,80	0,2	6,9	-0,4	-9,3	1,1	8
4	-24941,95	156212,19	0,8	7,2	-2,2	-9,7	1,8	8,4
4	-24946,59	156214,08	0,5	7,5	-6	-10,9	3,8	9,4
4	-24951,23	156215,95	2,1	9	-9,2	-12,7	5,9	10,6
4	-24955,86	156217,84	2,5	9,9	-11,1	-14,1	6,9	12,3
4	-24960,49	156219,74	1	10	-10,2	-14,8	-5,5	-12,8
4	-24964,41	156222,85	-2,8	8,5	-6,7	-13,4	-2	-11,7
4	-24968,33	156225,95	-5,5	7,5	-3,8	-12,6	1,4	-10,9
4	-24972,25	156229,06	7	-8,2	-1,9	-13,5	2,9	-11,5
4	-24976,17	156232,16	-10,7	7,4	3,2	-12,8	7	-11,2

Table B – Values obtained from the electromagnetic survey of in-phase and quadrature for every frequency (19,2 kHz, 22,1 kHz, and 23,4 kHz) and the coordinates of all stations (Datum: ETRS89 Portugal TM06 EPSG:3763) (Continuation).

Profile nº	Longitude	Latitude	In-phase 19,2	Quad 19,2	In-phase 22,1	Quad 22,1	In-phase 23,4	Quad 23,4
4	-24980,10	156235,25	-12,9	7,3	5,4	-13,3	10,6	-11,3
4	-24984,03	156238,35	-16,6	6,1	9,2	-12,6	14,3	-10
4	-24987,96	156241,44	-20,3	4,2	12,9	-11,3	17,4	-8,5
4	-24991,89	156244,54	-22,2	4,2	18,1	-10,9	-20,4	8,4
4	-24996,03	156247,31	-23,5	5	22,1	-10,8	-23,5	9,3
4	-25000,42	156249,71	-25,4	3,5	26,4	-9,8	-26,2	7,9
4	-25004,81	156252,10	-28,7	1	31,8	-6,8	-31	5,1
4	-25009,20	156254,50	-30,5	-0,4	34,9	-5,8	-33,8	3,3
4	-25013,59	156256,89	-31,6	-1	37,2	-4,8	-34,7	2,7
4	-25019,00	156260,46	-31,5	-0,7	-40,9	5,6	-36	3,4
5	-24919,01	156156,80			-16,6	13,1	0,7	6,8
5	-24920,40	156151,65			-14,7	13,7	1,6	7
5	-24921,77	156146,51			-12,8	14	4,7	6,9
5	-24923,14	156141,37			-11,9	14,2	6,1	6,3
5	-24924,52	156136,23			-12,5	13,7	6,8	5,6
5	-24925,89	156131,10			-15	12,7	5	5,7
5	-24928,16	156126,58			-16,5	10,7	3	4,7
5	-24930,62	156122,20			-19,3	8,2	0,8	4,1
5	-24933,08	156117,82			-21,6	5	-1,1	1,7
5	-24935,54	156113,44			-22,1	2,1	-1,6	0,5
5	-24937,60	156108,93			-20,2	1,2	-0,2	-0,2
5	-24936,98	156103,54			-10,5	0,6	8,6	-1,9
5	-24936,36	156098,16			-7,3	0,9	13	-2,4
5	-24936,84	156092,87			-8,3	2,9	8,7	0
5	-24939,00	156088,49			-10,1	4,3	5,9	2
5	-24942,12	156084,92			-11,5	5,7	4,9	3
5	-24945,25	156081,35			-9,9	6,3	3,4	4
5	-24948,36	156077,78			-8,7	6,4	5,3	3,6
5	-24951,48	156074,20			-7,6	7	4,2	3,9
5	-24954,61	156070,62			-7,1	7,2	4,4	4,3
5	-24957,72	156067,05			-7,2	8,5	3	5,2
5	-24960,12	156062,71			-5,6	8,7	4,4	5,2
5	-24961,08	156057,63			-4	8,8	8,3	6,1
5	-24959,88	156052,71			3,9	8,8	13,3	5,8
5	-24957,13	156048,66			8,1	8	17,9	4,3
5	-24954,07	156045,03			9,3	8	20,6	4,2
5	-24950,91	156041,54			16,6	7,5	25,7	3,9
5	-24947,76	156038,03			15,3	7,5	25	3,9
5	-24944,82	156034,22			15,1	7,2	25,5	3,5
5	-24942,06	156030,19			13,4	6,4	23,8	3,4
5	-24939,23	156026,23			12,9	6,5	22,9	2,6
5	-24936,12	156022,65			12	6,5	21,9	2,8
5	-24932,82	156019,44			14,1	6,8	23,8	2,9
5	-24929,37	156016,44			14,3	6,7	23,4	3
5	-24925,94	156013,44			15,2	7	24,1	2,5
5	-24922,50	156010,43			14,9	7,5	24,4	3,2
5	-24919,07	156007,42			16,4	7,1	24,4	2,3
5	-24915,63	156004,43			17,2	7,2	24,9	2,9
5	-24912,09	156001,66			16,9	7,5	25,1	3
5	-24908,40	155999,24			17	7,1	-26,1	-3
5	-24904,71	155996,83			17,5	6,8	-25,7	-2,6
5	-24901,01	155994,41			16,6	7,6	-25,3	-2,5
5	-24897,32	155991,99			16,7	7,2	-25,2	-2,6
5	-24893,64	155989,57			17,7	6,7	-25,8	-2,6

Table B – Values obtained from the electromagnetic survey of in-phase and quadrature for every frequency (19,2 kHz, 22,1 kHz, and 23,4 kHz) and the coordinates of all stations (Datum: ETRS89 Portugal TM06 EPSG:3763) (Continuation).

Profile nº	Longitude	Latitude	In-phase 19,2	Quad 19,2	In-phase 22,1	Quad 22,1	In-phase 23,4	Quad 23,4
5	-24889,87	155987,36			16	7	24,9	2,8
5	-24886,10	155985,16			16,9	7,4	-25,6	-2,7
5	-24882,33	155982,97			16,4	7	-25,4	-2,3
5	-24878,56	155980,78			14,6	6,6	-25,6	-2,4
5	-24874,78	155978,59			18,1	6,6	-24,7	-2,4
5	-24871,10	155976,17			15	6,7	-23,1	-1,9
5	-24867,72	155973,07			16	7,5	-24,9	-1,7
5	-24864,37	155969,90			15,2	6,9	-23,8	-2,6
5	-24860,66	155969,19			18,3	7	-25,6	-2,2
5	-24856,70	155970,65			-21	-7	-26,6	-1,1
5	-24852,90	155972,80			-20,4	-7,1	-23,5	-1,9
5	-24849,11	155974,96			-19,9	-6,5	-23,5	-1,8
5	-24845,33	155977,11			-18,9	-6,6	-22,6	-1,4
5	-24841,54	155979,26			-17	-6,8	-21,1	-1,4
5	-24839,58	155980,36			-16,5	-6,5	-23,5	-1

Appendix 3 – Magnetic Values

Table C – Values of the magnetic field obtained through the magnetic surveys, with the stations' numbers and coordinates (Datum: ETRS89 Portugal TM06; EPSG: 3763).

Station	Longitude	Latitude	Field (nT)	Station	Longitude	Latitude	Field (nT)
1	-24821,01	155848,45	45029,0500	**54**	-24889,94	156180,42	44980,8888
2	-24814,24	155948,83	45005,8836	**55**	-24883,70	156180,74	44981,7821
3	-24813,23	155942,61	45008,8969	**56**	-24878,42	156180,60	44970,4754
4	-24815,65	155954,72	45011,3635	**57**	-24873,38	156180,81	44955,0254
5	-24818,15	155959,95	45014,5468	**58**	-24866,75	156176,12	44962,3787
6	-24819,39	155966,84	45013,3302	**59**	-24861,30	156173,43	44962,6087
7	-24821,97	155974,18	45004,4335	**60**	-24855,94	156171,44	44970,5920
8	-24822,71	155979,73	44996,2768	**61**	-24850,68	156169,63	44977,6419
9	-24823,28	155985,40	44995,6501	**62**	-24845,88	156167,95	44955,4852
10	-24824,35	155991,51	45001,3434	**63**	-24841,04	156165,51	44972,1152
11	-24826,19	155995,85	45003,9667	**64**	-24836,80	156162,80	44993,1152
12	-24826,08	156000,62	45009,2500	**65**	-24831,43	156159,78	44966,9352
13	-24826,58	156005,03	45013,1433	**66**	-24825,30	156157,21	44981,0952
14	-24827,48	156009,76	45012,9466	**67**	-24819,94	156155,19	44978,2285
15	-24828,08	156014,71	45011,7299	**68**	-24813,98	156151,73	44986,3518
16	-24829,43	156019,06	45008,1532	**69**	-24809,28	156147,71	44980,4051
17	-24831,01	156024,24	45003,4965	**70**	-24804,50	156145,14	44998,8651
18	-24832,58	156029,04	45002,4799	**71**	-24801,23	156142,69	44989,6250
19	-24834,01	156034,14	45003,8565	**72**	-24795,19	156139,89	44981,6583
20	-24835,62	156038,52	45006,3698	**73**	-24788,05	156137,87	44980,3483
21	-24837,45	156044,86	45004,3997	**74**	-24783,63	156135,69	44983,5783
22	-24838,60	156051,53	45005,2331	**75**	-24778,45	156134,34	44991,6416
23	-24841,19	156056,53	45006,2064	**76**	-24773,28	156131,03	45001,3416
24	-24843,84	156061,90	45011,5764	**77**	-24769,30	156128,71	44998,5216
25	-24846,16	156068,50	45010,6830	**78**	-24764,42	156126,08	44995,6882
26	-24849,16	156073,08	45000,5096	**79**	-24880,08	156186,05	44951,5707
27	-24852,09	156078,25	44990,6129	**80**	-24885,20	156189,51	44957,1207
28	-24854,34	156082,60	44998,2662	**81**	-24889,98	156191,97	44981,9740
29	-24856,30	156087,02	44999,5295	**82**	-24893,30	156196,04	44979,8673
30	-24859,22	156092,02	45000,9529	**83**	-24897,69	156199,55	44975,0206
31	-24862,52	156095,47	45004,2562	**84**	-24902,72	156201,45	44974,2306
32	-24866,31	156098,59	45005,1495	**85**	-24907,51	156203,13	44976,0639
33	-24869,80	156102,07	45005,8128	**86**	-24912,50	156205,05	45009,0139
34	-24872,71	156105,95	45003,0661	**87**	-24918,21	156206,10	44988,4738
35	-24876,14	156108,63	45007,2294	**88**	-24924,22	156206,74	44988,3371
36	-24879,24	156112,86	45001,9727	**89**	-24930,06	156208,50	44990,1105
37	-24881,41	156116,97	44998,2060	**90**	-24935,81	156209,56	44994,1604
38	-24886,53	156120,32	45002,4893	**91**	-24940,51	156210,24	44993,1438
39	-24890,47	156123,45	45005,8293	**92**	-24946,14	156211,15	44992,8737
40	-24891,80	156126,34	45005,6526	**93**	-24949,83	156213,05	44993,7470
41	-24896,24	156131,35	45006,5659	**94**	-24954,28	156214,51	44991,3870
42	-24897,57	156134,58	45003,2425	**95**	-24958,56	156215,63	44985,4803
43	-24900,75	156138,36	45004,6891	**96**	-24963,59	156218,43	44984,3803
44	-24904,85	156144,04	45012,0991	**97**	-24968,71	156221,67	44990,4636
45	-24908,70	156148,29	45011,6357	**98**	-24970,88	156226,34	44988,3369
46	-24911,40	156152,19	45014,9524	**99**	-24975,99	156230,80	44991,2202
47	-24913,46	156157,62	45008,1757	**100**	-24980,25	156233,03	44993,6035
48	-24916,56	156160,74	44993,6489	**101**	-24984,90	156236,63	44995,9169
49	-24916,54	156167,18	44991,2289	**102**	-24990,23	156239,03	44993,1402
50	-24913,16	156172,50	45017,7722	**103**	-24995,33	156241,51	44996,5501
51	-24909,53	156176,93	45005,5622	**104**	-25000,36	156244,13	44998,2101
52	-24902,71	156179,46	45006,7822	**105**	-25006,36	156247,44	45002,0901
53	-24895,65	156180,33	44993,5155	**106**	-25012,96	156250,14	45003,2901

Table C – Values of the magnetic field obtained through the magnetic surveys, with the stations' numbers and coordinates (Datum: ETRS89 Portugal TM06; EPSG: 3763) (Continuation).

Station	Longitude	Latitude	Field (nT)	Station	Longitude	Latitude	Field (nT)
107	-25019,27	156254,19	44999,6227	**163**	-24835,53	155967,67	45017,9448
108	-24919,13	156156,09	45007,9227	**164**	-24834,20	155961,89	45017,9981
109	-24920,63	156149,98	45010,1727	**165**	-24833,12	155957,78	45017,7614
110	-24921,75	156142,77	45008,0427	**166**	-24832,75	155953,26	45016,4581
111	-24922,27	156136,44	45007,6727	**167**	-24832,14	155949,44	45016,8014
112	-24923,55	156132,89	45008,8527	**168**	-24829,28	155944,71	45016,6447
113	-24924,99	156128,78	45009,5626	**169**	-24827,03	155940,66	45018,3746
114	-24926,86	156122,90	45007,0159	**170**	-24824,87	155936,98	45019,1879
115	-24930,99	156117,48	45011,1259	**171**	-24821,70	155930,09	45023,7746
116	-24933,86	156113,82	45007,9192	**172**	-24819,53	155924,75	45021,1779
117	-24937,71	156110,29	45006,5192	**173**	-24833,78	155911,55	45021,8179
118	-24935,49	156104,72	45009,0392	**174**	-24818,63	155917,53	45022,7812
119	-24933,91	156099,38	45011,4392	**175**	-24817,37	155911,77	45024,9411
120	-24934,86	156093,39	45012,0391	**176**	-24817,30	155906,90	45025,8711
121	-24937,23	156088,18	45012,6524	**177**	-24818,20	155901,57	45024,7211
122	-24940,35	156085,30	45013,2824	**178**	-24817,75	155897,37	45022,1944
123	-24943,98	156079,54	45017,3657	**179**	-24813,62	155894,97	45028,9242
124	-24948,22	156075,93	45019,2190	**180**	-25124,55	155766,00	45011,7300
125	-24951,90	156072,90	45016,7323	**181**	-25158,81	155792,86	45052,6500
126	-24954,35	156070,02	45017,0857	**182**	-25193,84	155808,90	45057,5700
127	-24957,67	156066,77	45019,3856	**183**	-25190,24	155864,22	45072,4900
128	-24958,83	156062,82	45018,5789	**184**	-25190,70	155899,17	45074,4300
129	-24960,36	156058,05	45018,0289	**185**	-25205,52	155933,47	45063,3800
130	-24959,32	156054,10	45023,2422	**186**	-25230,61	155976,59	45066,2700
131	-24955,42	156050,19	45020,1522	**187**	-25241,12	156015,61	45056,2400
132	-24951,37	156045,69	45019,0422	**188**	-25224,44	156054,99	45041,1900
133	-24946,57	156040,22	45020,9221	**189**	-25217,22	156104,17	45049,1400
134	-24942,52	156036,09	45020,3621	**190**	-25204,41	156125,21	45048,0800
135	-24940,04	156032,11	45020,7221	**191**	-25184,68	156153,91	45057,0600
136	-24936,29	156027,39	45022,9521	**192**	-25143,91	156192,76	45046,9800
137	-24933,74	156024,08	45019,9921	**193**	-25117,12	156215,24	45024,9200
138	-24929,90	156019,63	45022,6821	**194**	-25069,04	156227,73	45022,8200
139	-24926,23	156016,88	45019,4520	**195**	-25031,66	156249,33	45003,7600
140	-24922,78	156014,18	45020,8120	**196**	-25029,84	156236,19	45017,5500
141	-24919,33	156011,63	45019,7953	**197**	-25041,87	156204,60	45004,4900
142	-24915,88	156008,63	45022,2853	**198**	-25053,40	156186,42	45007,4400
143	-24910,63	156005,18	45020,4553	**199**	-25059,41	156135,10	45023,3900
144	-24906,58	156002,18	45020,3453	**200**	-25066,52	156116,43	45024,3300
145	-24902,98	155999,93	45018,1052	**201**	-25047,06	156069,65	45026,2500
146	-24898,93	155997,53	45019,3785	**202**	-25048,75	156032,71	45034,1700
147	-24895,17	155994,37	45018,4385	**203**	-25044,23	155998,99	45042,1200
148	-24890,07	155991,52	45019,2285	**204**	-25058,94	155973,69	45039,0100
149	-24886,02	155988,67	45018,9285	**205**	-25068,17	155946,24	45052,9000
150	-24882,42	155985,52	45017,3385	**206**	-25084,19	155916,24	45064,8000
151	-24877,92	155983,27	45018,4085	**207**	-25098,40	155898,94	45064,6600
152	-24874,17	155981,47	45017,1118	**208**	-25120,51	155882,98	45063,5800
153	-24870,12	155978,92	45017,2284	**209**	-25155,35	155864,49	45077,5300
154	-24865,91	155975,92	45015,8117	**210**	-25186,42	155842,98	45076,4200
155	-24861,26	155973,52	45015,5850	**211**	-24852,88	155849,07	45047,8800
156	-24856,76	155973,82	45014,2783	**212**	-24897,50	155851,02	45045,7088
157	-24852,56	155975,62	45014,8216	**213**	-24931,91	155876,18	45042,4548
158	-24846,86	155976,97	45013,8216	**214**	-24955,36	155841,90	45059,2007
159	-24843,86	155979,37	45012,9016	**215**	-25079,94	155799,54	45013,7773
160	-24839,51	155982,22	45009,0616	**216**	-25052,96	155942,95	45045,7612
161	-24836,80	155976,52	45015,8915	**217**	-25020,88	155962,26	45044,6765
162	-24835,68	155972,22	45014,1315	**218**	-24993,09	155980,92	45038,5072

Table C – Values of the magnetic field obtained through the magnetic surveys, with the stations' numbers and coordinates (Datum: ETRS89 Portugal TM06; EPSG: 3763) (Continuation).

Station	Longitude	Latitude	Field (nT)
219	-24990,13	156023,24	45030,0838
220	-24965,83	156009,91	45028,9144
221	-24939,84	155995,67	45031,7451
222	-24910,18	155969,30	45036,5757
223	-24876,70	155947,56	45033,4064
224	-24851,04	155921,90	45035,2370
225	-24845,74	155891,83	45042,8983
226	-24877,32	155907,12	45033,7289
227	-24917,13	155926,78	45041,4749
228	-24936,14	155935,09	45039,2209

Appendix 4 – Radiometric Values

Table D – Values of K, U and Th in % and ppm and counts for every station, with its coordinates (Datum: ETRS89 Portugal TM06; EPSG:3763).

Station	Longitude	Latitude	ToT (C)	K (C)	U (C)	Th (C)	ToT (ppm)	K (%)	U (ppm)	Th (ppm)
1	-25201,6	155843,0	2059,5	453,5	137,5	78,5	16,7	1,6	3,6	9,3
2	-24855,4	156087,1	2943,5	698,5	159,0	102,0	23,9	2,7	4,1	12,2
3	-25593,3	156709,2	2500,0	629,0	123,0	91,0	20,3	2,4	3,3	10,9
4	-25793,3	156969,9	2480,0	613,5	121,0	78,5	20,1	2,3	3,2	9,3
5	-26054,3	156767,7	2015,0	448,0	116,0	80,0	16,3	1,6	3,1	9,5
6	-25029,3	156252,6	3952,0	885,0	242,0	165,0	32,2	3,5	6,1	19,8
7	-24878,9	156183,6	2669,5	616,0	148,0	132,0	21,7	2,3	3,9	15,8
8	-24727,8	156063,6	3846,5	970,0	222,0	120,5	31,3	3,8	5,7	14,4
9	-24939,3	156029,2	2716,0	698,0	123,5	90,0	22,1	2,7	3,3	10,7
10	-25066,3	156122,2	2403,0	621,0	112,0	81,0	19,5	2,4	3,0	9,6
11	-24903,4	156383,2	3639,5	856,5	176,0	175,5	29,6	3,3	4,5	21,1
12	-24588,4	156268,0	4163,0	968,5	227,0	208,5	33,9	3,8	5,8	25,1
13	-24757,5	156458,8	3452,0	710,0	227,5	169,0	28,1	2,7	5,8	20,3
14	-24911,6	156697,7	3253,0	739,5	182,5	145,0	26,5	2,8	4,7	17,4
15	-25113,8	155424,5	2533,5	590,0	146,0	98,5	20,6	2,2	3,8	11,8
16	-25544,2	155582,9	2835,5	721,0	135,5	108,0	23,0	2,8	3,6	12,9
17	-25735,5	155701,0	2690,0	693,0	128,7	93,0	21,9	2,7	3,4	11,1
18	-25790,4	155964,5	1523,0	341,3	83,3	57,7	12,3	1,2	2,3	6,8
19	-25830,0	156303,3	1576,0	347,5	83,5	70,5	12,7	1,2	2,3	8,4
20	-25287,0	156492,6	3156,0	682,0	193,5	142,5	25,7	2,6	5,0	17,1
21	-25563,5	156479,8	3495,5	926,5	155,0	113,0	28,5	3,6	4,0	13,5
22	-25579,4	156159,9	2356,5	531,5	111,0	83,0	19,1	2,0	3,0	9,9
23	-25618,9	155759,5	2966,5	769,5	130,0	94,0	24,1	3,0	3,4	11,2
24	-24820,3	155852,4	1846,5	434,5	110,0	72,5	14,9	1,6	2,9	8,6
25	-24994,2	155801,7	1678,0	352,0	108,5	61,5	13,6	1,2	2,9	7,3
26	-25278,5	155744,8	2568,5	654,0	118,5	91,5	20,9	2,5	3,1	10,9
27	-25383,8	155609,6	1350,5	233,0	83,0	68,0	10,9	0,7	2,3	8,1
28	-25436,4	155761,0	2782,5	704,5	131,5	97,5	22,6	2,7	3,5	11,6
29	-25368,2	155881,2	2240,5	545,0	125,5	86,0	18,2	2,0	3,3	10,2
30	-25379,3	156075,6	2077,0	483,0	114,0	89,5	16,8	1,8	3,0	10,7
31	-25241,8	156013,4	2648,5	660,0	135,0	93,0	21,5	2,5	3,5	11,1
32	-25167,9	156175,5	2533,5	605,5	131,0	104,5	20,6	2,3	3,5	12,5
33	-25196,7	156845,0	3841,0	824,0	215,5	217,5	31,3	3,2	5,5	26,1
34	-25117,2	156873,5	2586,0	523,0	157,0	134,5	21,0	1,9	4,1	16,1
35	-25063,0	156920,0	926,5	158,5	62,5	48,5	7,4	0,4	1,8	5,7
36	-24997,9	156991,6	3100,5	755,5	158,0	136,0	25,2	2,9	4,1	16,3
37	-24890,7	156671,5	1167,5	182,5	82,0	67,5	9,4	0,5	2,3	8,0
38	-24642,9	156368,9	1559,5	266,0	105,0	95,5	12,6	0,9	2,8	11,4
39	-24775,4	156656,8	3231,5	763,5	181,0	146,5	26,3	2,9	4,7	17,6
40	-24498,3	156451,1	2268,3	468,0	145,0	113,0	18,4	1,7	3,8	13,5
41	-24541,0	155549,3	3531,5	861,5	182,0	137,0	28,8	3,4	4,7	16,4
42	-24893,5	154788,8	2618,5	631,5	147,0	93,5	21,3	2,4	3,8	11,2
43	-25693,9	154913,7	1924,0	411,0	132,5	80,0	15,6	1,5	3,5	9,5